

**INVESTIGATION OF AQUEOUS DROPLET-BASED ELECTROSTATIC
TRANSDUCTION**

by

Graham Allegretto

B.Eng., University of Victoria, 2014

A THESIS SUBMITTED IN PARTIAL FULFILLMENT OF
THE REQUIREMENTS FOR THE DEGREE OF

MASTER OF APPLIED SCIENCES

in

THE FACULTY OF GRADUATE AND POSTDOCTORAL STUDIES

(Electrical Engineering)

THE UNIVERSITY OF BRITISH COLUMBIA

(Vancouver)

August 2017

© Graham Allegretto, 2017

Abstract

With the effects of climate change being felt more and more each day, any form of alternative energy production, no matter how small, must be investigated. Each new transduction mechanism discovered opens up new possibilities of harnessing energy that was previously untapped or underutilized, possibly shifting some of the burden on carbon-based power plants to non-emitting sources. Even if the mechanism is inefficient or unsuitable for energy conversion, the technology may still be useful as a sensor. This thesis examines a recently discovered mechanical-to-electrical transduction mechanism that can be as simple as a water droplet sandwiched between vibrating electrodes.

The mechanism in question is analogous to electrostatic transduction where motion is converted to electricity by pulling apart the two plates of a charged capacitor. Conventional technology, however, has plateaued as their performance is limited by the breakdown potential of air. One drawback of using this transduction mechanism is the necessity of having a biasing source, a requirement not shared by electromagnetic and piezoelectric transducers. By utilizing an electrical double layer capacitor's (EDLC) high capacitance per area and inherent self-biasing, performance can be improved and one disadvantage can be avoided.

In this work, we demonstrate such a device using a droplet of water between two Indium Tin Oxide (ITO) electrodes with one electrode being coated with poly[4,5-difluoro-2,2-bis(trifluoromethyl)-1,3-dioxole-co-tetrafluoroethylene] (PTFE-AF). We investigate its frequency response, an important parameter for sensing and generation applications, and show an improved frequency response of up to 100 Hz, surpassing literature's best, with a maximum

peak-to-peak voltage of 892 mV. We present a linear approximation model that can be used for further optimization of such a system and correctly predicts the point of maximum power transfer. We also investigate how and why the technology self-biases, proposing an alternative theory to those posed in literature. We finally evaluate the system as both a sensor and generator in its current state and ideas that could make this technology competitive.

Lay Summary

Converting vibrational energy into electricity could potentially extend battery life of handheld devices or replace batteries altogether. This thesis investigates a new way of doing so by using a method that can be as simple as a droplet of water sandwiched between two electrodes. The main goal of this thesis is to understand what is possible with this technology and whether or not it should be studied further. A mathematical model is presented that shows how to improve the amount of power it can harness and identifies the two most critical aspects that govern performance. This work also proposes an alternative theory compared to what has been given in literature as to why electricity is generated in the first place. An assessment and potential applications of the technology are then presented.

Preface

All aspects of the material appearing in this thesis have been originally written by the author unless otherwise stated.

Previous work that led to the discovery of this effect was performed collaboratively with fellow Master's student Yuta Dobashi.

Dr. John Madden supervised and helped me develop the linear model presented in Chapter 3. He also thoroughly reviewed the thesis prior to defense and submission.

Table of Contents

Abstract.....	ii
Lay Summary	iv
Preface.....	v
Table of Contents	vi
List of Figures.....	ix
List of Abbreviations	xi
Acknowledgements	xii
Chapter 1: Introduction	1
1.1 Electrostatic Transduction	1
1.2 Electrical Double Layer	5
1.3 An EDL-Based Transducer.....	8
1.4 Literature Review.....	13
1.5 Thesis Outline	17
Chapter 2: Experimental Setup.....	18
2.1 Device Preparation.....	18
2.2 Vibration Source	20
2.3 Bose Interface and Experimentation Arduino-Shield Printed Circuit Board (PCB)	22
2.3.1 Arduino Compatibility	23
2.3.2 Buffer Amplifier	24
2.3.3 Frequency Response	24
2.3.4 Point of Maximum Power Transfer	25

2.3.5	Bias Potential Investigation	25
2.4	Capacitance and Surface Area Measurements	26
2.5	Data Analysis	27
2.6	A Note on Repeatability.....	30
Chapter 3: Frequency Response and Linear Model.....		31
3.1	Experiment.....	31
3.2	Results.....	31
3.3	Increase in Bandwidth.....	35
3.4	Linear Model Derivation.....	38
3.5	Discussion.....	41
3.5.1	Point of Maximum Power Transfer Prediction	44
3.6	Conclusion	47
Chapter 4: Origin of V_{bias}.....		49
4.1	Self-Biasing Theories.....	49
4.1.1	Determining Charging	52
4.1.2	Measuring V _{bias}	55
4.2	Experiments	58
4.2.1	Varying Surface Area	58
4.2.2	Varying CEDL	60
4.2.3	Varying pH.....	62
4.2.4	Step Response	64
4.3	Discussion.....	68
4.3.1	Hydroxide Adsorption Induced Charging.....	69

4.4	Summary	70
Chapter 5: Conclusion and Future Work.....		72
5.1	Research Conducted.....	72
5.2	Further Work.....	74
5.3	Outlook and Applications	75
5.3.1	Sensing.....	75
5.3.2	Generation.....	77
5.4	Concluding Remarks.....	81
Bibliography		82
Appendices.....		86
Appendix A Bose Interface Experimentation Arduino-Shield Printed Circuit Board.....		86
A.1	Schematics	87
A.2	Layout	89
Appendix B Arduino Code		90
B.1	Digital Potentiometer Library	97
Appendix C MATLAB Code.....		100
C.1	EDL Simulation Code.....	100
C.2	Phase Measurement Code.....	103

List of Figures

Figure 1-1 – Demonstration of Electrostatic Transduction.....	3
Figure 1-2 – The Electrical Double Layer	5
Figure 1-3 – Smoluchowski Smearing at Conductor Interface.....	7
Figure 1-4 – Potential Profile across Two Identical Electrodes in Solution at Steady State.....	8
Figure 1-5 – Equivalent Electrical Circuit.	10
Figure 1-6 – EDL Transduction Cycle.....	13
Figure 1-7 – Parallel Electrode EDL-Based Transducer	14
Figure 1-8 – Top Electrode Capacitance.	16
Figure 2-1 – Experimental Setup.	18
Figure 2-2 – Electrode Configuration	19
Figure 2-3 – Bose ElectroForce 3100 Tensiometer.	21
Figure 2-4 – 3D Printed Electrode Holders	22
Figure 2-5 –Bose Interface and Experimentation Arduino-Shield PCB.....	23
Figure 2-6 – Droplet Profile Views.	27
Figure 2-7 - Surface Area Measurement.....	28
Figure 2-8 – Transforming Mover Throw to Surface Area	29
Figure 3-1 – Standard Device Bode Plot	32
Figure 3-2 – Low Frequency Perturbation.....	34
Figure 3-3 – Perturbations of Top vs. Bottom Electrode Gain Phase Log-Log Plots	36
Figure 3-4 – Varying Electrode Separation Offset Distance Bode Plot	37
Figure 3-5 – Linear Approximation Model Equivalent Electrical Circuits	41

Figure 3-6 – Time Domain Comparison of Models for Varying Relative Changes in Capacitance	43
Figure 3-7 – Frequency Domain Signal Amplitude Comparison of Models.....	44
Figure 3-8 – Moon Device Power Curves	45
Figure 3-9 – Point of Maximum Power Transfer Prediction	47
Figure 4-1 – EDL Charging Theory.....	50
Figure 4-2 - Hydroxide Ion Physical Adsorption	51
Figure 4-3 – Voltage Source Approximation.....	54
Figure 4-4 – V_{bias} Test Circuit.....	55
Figure 4-5 – Bias Electronics Validation Log-Log Plots.....	56
Figure 4-6 – Bias Variation.....	57
Figure 4-7 - Plate Separation Distance Notation	59
Figure 4-8 – Varying Electrode Separation Distance	60
Figure 4-9 - Varying Electrode and Solution Composition V_{bias} Measurements	62
Figure 4-10 - V_{bias} Dependence on pH – V_{bias} measurements for varying pH solutions.	63
Figure 4-11 - Step Response: Standard Configuration	65
Figure 4-12 - Step Response: Reverse Electrode Setup.....	66
Figure 4-13 - Step Response Standard Setup after Reversing Electrode.....	67
Figure 4-14 – PTFE-Water Interface	69
Figure 5-1 - Artificial Fingerprint Embodiment.	76
Figure 5-2 – “Super” Transducer.....	80

List of Abbreviations

BSN	Body Sensor Network
EDL	Electric Double Layer
EDLC	Electric Double Layer Capacitor
EIS	Electrochemical Impedance Spectroscopy
GCS	Gouy-Chapman-Stern
IC	Integrated Circuit
ITO	Indium Tin Oxide
OHP	Outer Helmholtz Plane
PTFE	Polytetrafluoroethylene
SSR	Solid State Relay
WSN	Wireless Sensor Network

Acknowledgements

I'd like to thank the supervising committee for taking the time to read and review my Thesis. I would also like to thank NSERC for providing funding in the form of the Alexander Graham Bell CGS M scholarship and the CREATE NanoMat stipend.

I'd like to express my gratitude to my lab mates Mirza Saquib us Sarwar, Ali Mahmoudzadeh, Saeedeh Ebrahimi, Ali Rafiee, Matt Dawson, Justin Wyss, and Katelyn Dixon for all the help and making my experience with the lab a great one. I would like to extend a special thanks to Yuta Dobashi, fellow Master's student and lab mate, who was always available to help and kept me company throughout my degree. His work ethic is something to aspire to and I do not think I could have finished my thesis in timely manner without him.

Finally, I would like to thank my supervisor, Dr. John Madden. His breadth of knowledge is astonishing, covering everything from electrochemistry to condensed matter. The only thing that is more remarkable than his understanding of the physical world is his kindness. He was always available to talk no matter how busy he was and always greeted me with a smile. Working with him was truly a joy and I would not have been able to finish it without him.

Special thanks are owed to my parents, who have supported me throughout my years of education and have always been there for me. Thanks to my brother, Evan, for letting me keep my summer tires at his house.

Chapter 1: Introduction

Harnessing vibration energy could potentially extend battery life for handhelds and wearables [1], [2] and provide a minimally obtrusive power source for implantable medical devices [3]–[5]. Cellphone and tablet wall charging-adapters could become obsolete, and vibration-powered Wireless Sensor Networks (WSN) could drastically cut maintenance and installation costs for industrial applications [6], [7]. In this thesis, we investigate a new transduction mechanism that converts mechanical motion into electrical energy for harvesting and sensing applications. This section is dedicated to explaining background concepts essential to understand the thesis beginning with a discussion of a similar transduction mechanism and its theory of operation. The Electrical Double Layer (EDL), a concept that is central in understanding how the new transducer works, is also introduced. We finally review what has already been done in literature and provide a brief outline of what the thesis covers and how it is organized.

1.1 Electrostatic Transduction

Electrostatic transduction, the conversion of mechanical energy into electricity can be as simple as a variable-capacitor connected to a voltage source through a switch [3]. Figure 1-1 demonstrates the operation of a so-called voltage-constrained electrostatic energy harvester with a battery acting as a biasing source.

The battery initially charges the capacitor at its point of maximum capacitance—when the plates are the closest together (Figure 1-1a). As the plates are separated (Figure 1-1b), induced by a vibration, the capacitance decreases in accordance to the parallel-plate capacitance equation,

$$C = \frac{\epsilon A}{d}, \quad (1.1)$$

where C is capacitance, ϵ is the permittivity of the dielectric, A is the overlapping area of the two plates, and d is the distance between the two plates. Since capacitance is the measure of the amount of charge that can be stored for an applied voltage,

$$C = \frac{Q}{V}, \quad (1.2)$$

as capacitance decreases and the stored charge is not allowed to move, or is impeded to do so, the voltage across it will increase. Charge leaves the capacitor, acting to charge the battery, until the potential across the capacitor is equal to the voltage of the battery (Figure 1-1c). As a vibration forces the plates together, a switch can open to stop the current or can be recovered. Finally, when the plates reach their point of closest proximity, the battery then charges the capacitor where the cycle can be repeated [8].

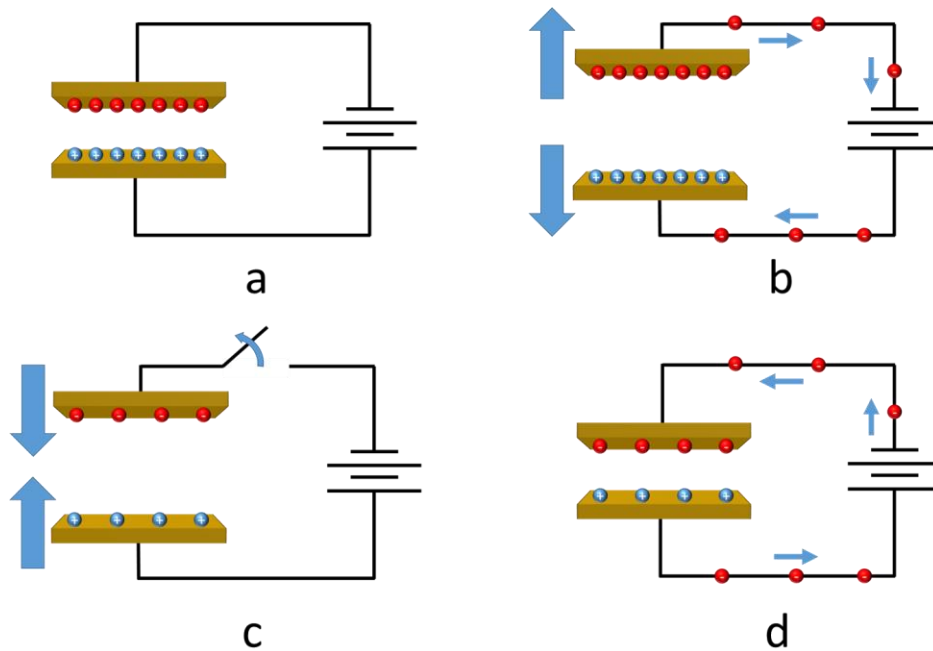


Figure 1-1 – Demonstration of Electrostatic Transduction – (a) Initially, the voltage source charges the capacitor plates. As the plates separate (b), current flows into the battery acting to charge it until the plates reach their widest separation. At this point, the switch opens to ensure that no charge flows into the capacitor as the plates come together (c). Once the plates are as close together as possible, the switch opens, allowing the battery to recharge the capacitor for the cycle to repeat itself.

At first glance, the above process seems counter-productive from a generation standpoint; the net amount of charge that enters the battery is equal to how much leaves, then how does it charge the battery? To begin with, following [8] and [9], the amount of energy required to precharge the capacitor, $E_{precharge}$, can be calculated by the amount of energy that the capacitor can store,

$$E_{precharge} = \frac{1}{2} C_{max} V_{bias}^2 ,$$

where C_{max} is the capacitance when the plates are the closest together and V_{bias} is the voltage of the battery. As the plates are separated (Figure 1-1b), and assuming that the voltage across the battery remains constant, the current that leaves the capacitor is equal to

$$i_{bat}(t) = \frac{dq_C}{dt} = \frac{d(CV_{bias})}{dt} = V_{bias} \frac{dC(t)}{dt}.$$

The energy harvested during this half cycle can be calculated,

$$E_{Harv} = \int V_{bias} i_{bat}(t) dt = V_{bias}^2 (C_{max} - C_{min}).$$

A switch is then opened as the plates moves together (Figure 1-1c), or, the energy remaining in the capacitor,

$$E_{Recov} = \frac{1}{2} C_{min} V_{bias}^2 ,$$

is recovered. Once the electrodes hit their point of maximum capacitance, the switch closes and the battery charges the capacitor for the cycle to start over again. Therefore, the amount of energy harvested over an entire cycle of a vibration can be calculated by

$$E_{net} = E_{Harv} + E_{Recov} - E_{Precharge} ,$$

which yields

$$E = \frac{1}{2} V_{bias}^2 (C_{max} - C_{min}). \quad (1.3)$$

For an optimized parallel-plate voltage-constrained electrostatic harvester, the amount of energy able to be harnessed will depend on the breakdown voltage of the dielectric material between the plates. To maximize these devices' efficiency, voltages are applied as high as possible without causing breakdown. In practical devices, however, high voltages are to be avoided. To reduce this potential, the plates are brought as close together to maximize C_{max} . Even if the plates are to come within 100 μm , a potential of 300 V would need to be applied to reach this threshold, assuming an air gap and a breakdown potential of 3 MV m^{-1} of air [10]. These voltages would extremely limit its potential applications. The fact that this transduction mechanism even requires a biasing source is one of the most commonly cited criticisms of the technology [7],

[11]–[13]. Other transduction methods, such as piezoelectric and electromagnetic methods, do not. The family of devices studied in this thesis does not require a biasing source to generate power and can possibly significantly increase the amount of power extracted. The initial theory is that the formation of an Electrical Double Layer (EDL), which is discussed in the following section, can act as both a biasing source and a variable capacitor. The origin of the potential generated is the topic of Chapter 4.

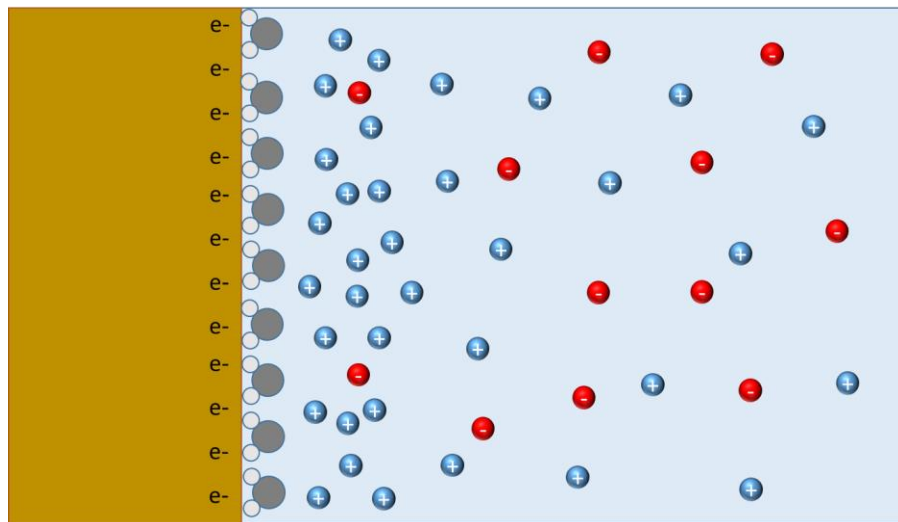


Figure 1-2 – The Electrical Double Layer – In this figure, the surface of the electrode initially contains a negative charge causing the buildup of positive ions immediately outside of the electrode. Water molecules are oriented with the hydrogens nearest to the electrode due to the high electric field.

1.2 Electrical Double Layer

Ions in solution are free to move. On average, the net charge per volume of solution is normally zero [14]. This equilibrium, however, can be disrupted. By submerging an electrode and applying a bias to it, oppositely-charged ions can accumulate at the interface between the electrode and solution, screening the applied electric field. An excess of one type of ion, and a

deficiency of its counter, will develop in the solution where the electric field strength is strongest. The net charge of the electrolyte just outside the electrode will no longer be zero but will rather equal the charge directly on the surface of the metal. Coined the diffuse layer, it extends from as close as a counter-ion can come to the surface, also known as the Outer Helmholtz Plane (OHP), up until the solution's net charge is again zero, ranging from tens of angstroms (10^{-10} m) for saturated solutions to microns for deionized water. The electric field near the interface can be as high as 10^9 V/m, causing water molecules to strongly orient themselves in respect to the electric field, and if the applied voltage is too high, electrolysis can occur. This arrangement of charges and dipoles is known as the Electrical Double Layer (EDL) and is frequently cited in electrochemistry [15]. In many ways it resembles a parallel-plate capacitor with plate separation distances in the order of nanometers or Angstroms (10^{-10} m), explaining the EDL's large capacitance. Its capacitance can be estimated by using a modified Equation 1.1,

$$C = \frac{\epsilon A}{\kappa}, \quad (1.4)$$

that considers the EDL's Debye length, κ (m), the distance in which the ions in solution screen the applied electric field [16]. It should be noted that the dielectric constant in the above equation will not be that of the bulk solution. The electric fields are so strong in an EDL that the alignment it imparts on the molecules affects its permittivity.

Alluded to earlier, even without applying an external biasing source an EDL can form. The abrupt junction of the metal into vacuum, or in this case electrolyte, can be enough to cause this redistribution of ions and a substantial voltage across the interface to be generated.

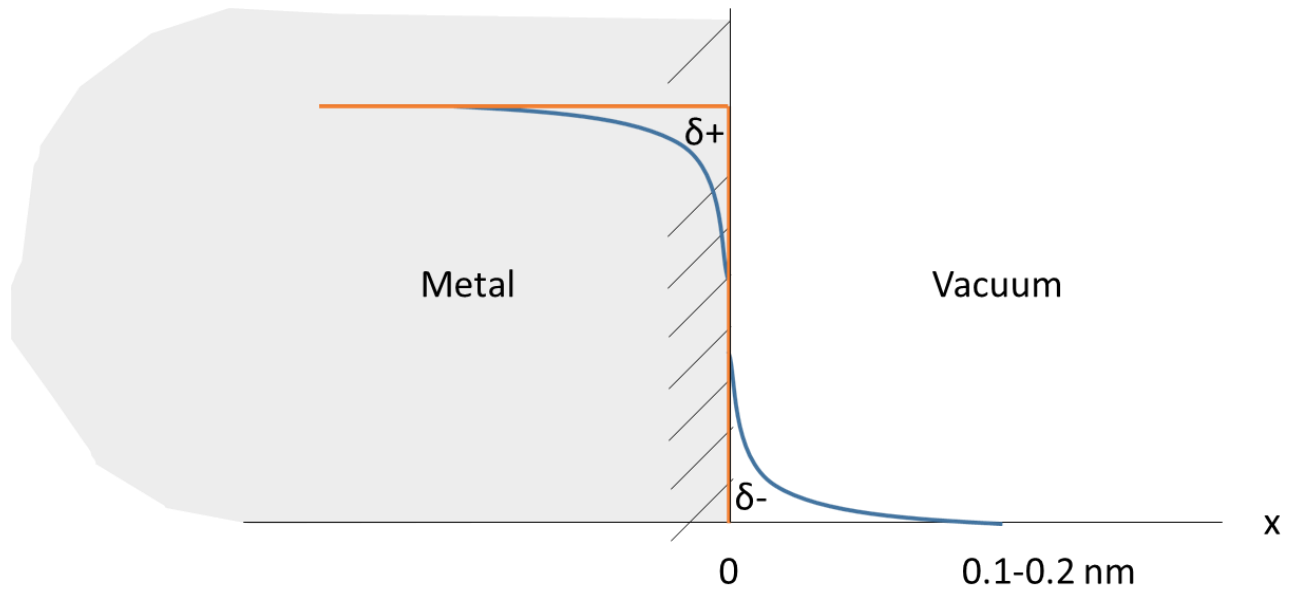


Figure 1-3 – Smoluchowski Smearing at Conductor Interface - Orange line indicates the background positive charge of the metal according to the Jellium model. The blue line represents the charge from the electron cloud that spills into vacuum. This results in a surface dipole. This image is adapted from [17, pp. 890–893].

To understand what happens at the interface between a metal and vacuum, the *jellium model* comes in handy. It approximates metal’s stationary positive nuclei as a constant positive background charge. The electrons are free to move and are modeled as an electron cloud. At the edge of the metal, the positive jellium ends abruptly but the electron cloud does not. The density function predicts the probability of an electron outside of the metal. This causes a dipole at the surface of the metal, with a partial positive charge inside the metal and a partial negative charge extending 0.1 to 0.2 nm outside of the metal. This dipole can attract cations in solution aiding in the formation of an EDL. A potential across the metal-electrolyte interface can be generated without external intervention [17, pp. 890–893]. Thus, by simply dipping a metal into and out of an electrolyte a rudimentary electrostatic transducer can be made, having both a variable

capacitor and an inherent biasing source owing to the EDL. Whether this phenomenon is what charges the device in question is the topic of Chapter 4.

1.3 An EDL-Based Transducer

With a single electrode-electrolyte interface, there is a potential source and a means to vary the capacitance, but the only way to drive a current or measure in reference to something is to have a second electrode. A second electrode-electrolyte interface introduces another source of capacitance and potential. If the electrodes are identical in composition, surface area, and are stationary, the biases will completely cancel each other out. Figure 1-4 illustrates the potential profile across solution including the surface dipole at the edge of the electrode and the EDL.

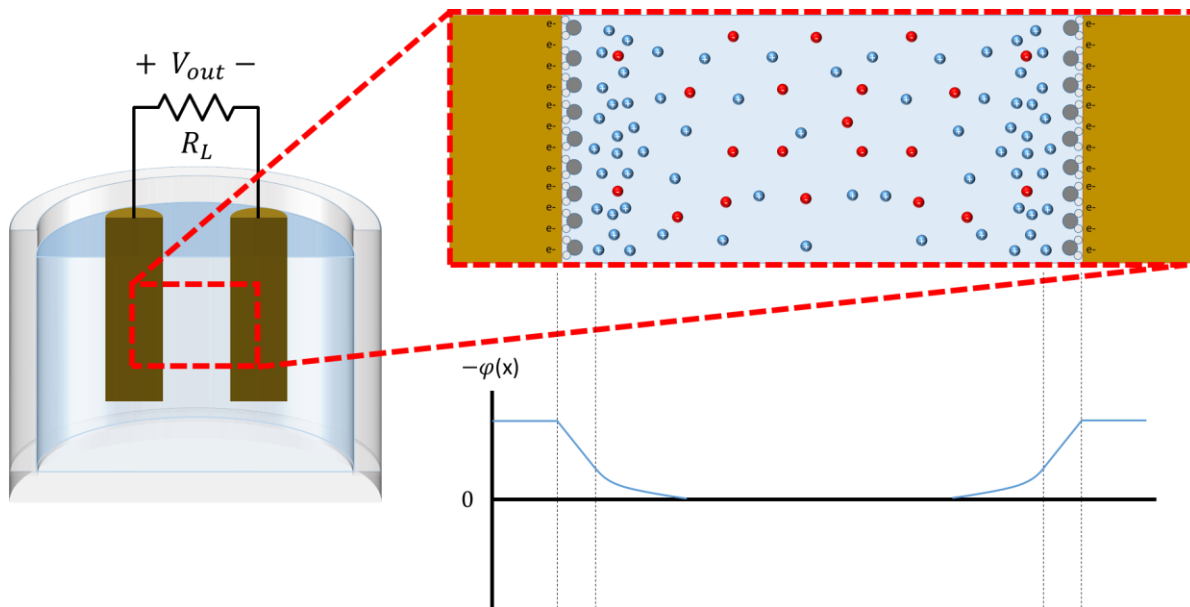


Figure 1-4 – Potential Profile across Two Identical Electrodes in Solution at Steady State - Assuming infinite conductivity, the potential within the electrodes will be constant. Immediately outside the electrode, the potential decreases linearly until the OHP. Past this point, the decay is more gradual and can be modeled by a hyperbolic sine function [15].

If the two electrodes are connected via an external circuit, as above, no current will flow as the EDL potentials will be equal. The charge on each electrode will then follow the equation,

$$V_{EDL} = V_L = V_R = \frac{Q_R}{C_R} = \frac{Q_L}{C_L},$$

where V_{EDL} is the potential generated across the electrode into solution via the EDL and V_L and V_R are the voltages across the left and right EDL capacitors. The amount of charge stored in the right electrode's EDL, Q_R , divided by its capacitance, C_R , will equal the charge stored in the left electrode's EDL, Q_L , divided by its capacitance, C_L . This is true for any two connected electrodes in electrolytes at equilibrium, regardless of the amount of surface area each has in contact with solution. Figure 1-5 shows the equivalent circuit model of two electrodes submerged in an electrolyte that is connected through an external load resistor, R_L . R_L is the ionic resistance of the electrolyte and is dependent on concentration and the distance the two electrodes are separated. We assume that the electrodes are perfect cylinders and each one is initially submerged to an equal depth to simplify subsequent calculations.

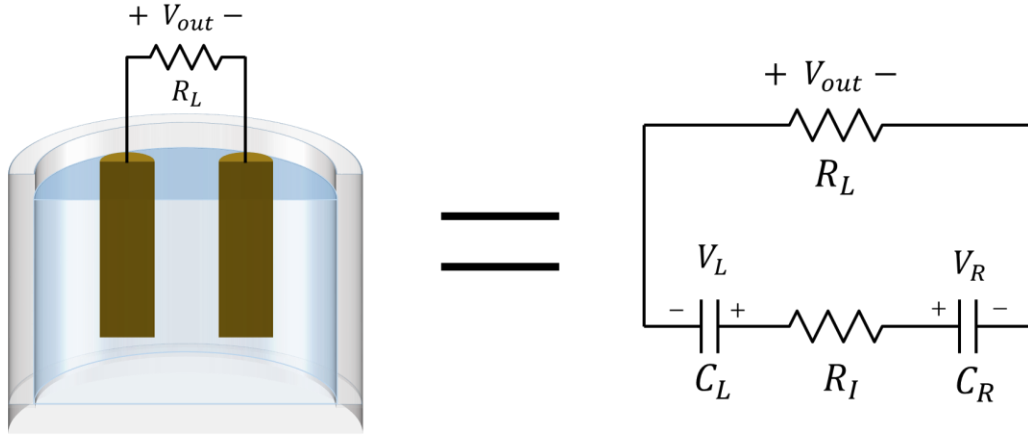


Figure 1-5 – Equivalent Electrical Circuit – Capacitors in the right figure symbolize the EDL capacitance at the surface of the electrodes. The ionic resistance of the solution, R_I , separates the two capacitors as well as an external load resistor, R_L . The sign convention of the output potential, V_{out} , is also shown in this image.

The capacitance of the cylindrical electrodes can then be estimated by substituting the surface area of a cylinder and its one end into Equation 1.4,

$$C(h) = \frac{\varepsilon A(h)}{\kappa} = \frac{\varepsilon(2\pi r h + \pi r^2)}{\kappa},$$

where h is the height of electrode in solution and r is the radius of the cylinder. As an electrode is submerged, its capacitance should increase, yielding

$$C(h_0 + \Delta h) = \frac{\varepsilon A(h_0 + \Delta h)}{\kappa} = \frac{\varepsilon(2\pi r(h_0 + \Delta h) + \pi r^2)}{\kappa},$$

which can be redefined as a static component and a varying component,

$$C(h_0 + \Delta h) = C^0 + \frac{\varepsilon 2\pi r \Delta h}{\kappa},$$

where h_0 is defined as the initial depth each electrode is submerged to, Δh is any deviation from this depth, and C^0 is the capacitance of an electrode at a depth of h_0 . As one electrode is submerged while the other left stationary, the open circuit voltage can be estimated by

$$V_{out} = V_R - V_L$$

and

$$V_{out}(C_R) = \frac{Q_R}{C_R} - \frac{Q_L}{C_L}.$$

Defining an electrode's capacitance as the combination of a static (C_R^0) and varying component (ΔC_R),

$$C_R \equiv C_R^0 + \Delta C_R,$$

the output will be

$$V_{out}(C_R^0 + \Delta C_R) = \frac{Q_R}{C_R^0 + \Delta C_R} - \frac{Q_L}{C_L} = \frac{Q_R}{C_R^0 \left(1 + \frac{\Delta C_R}{C_R^0}\right)} - \frac{Q_L}{C_L}.$$

Assuming ΔC_R is much smaller than C_R^0 , the output potential can be estimated as

$$V_{out}(h_0 + \Delta h) \approx \frac{Q_R}{C_R^0} - \frac{Q_L}{C_L} - \left(\frac{Q_R}{C_R^0}\right) \left(\frac{\Delta C_R}{C_R^0}\right)$$

yielding

$$V_{out} = V_{EDL} \left(\frac{\Delta C_R}{C_R^0}\right) \quad (1.5)$$

Equation 1.5 applies primarily to sensing as no current is drawn. If we allow R_L to become a finite value, a current will be able to flow when the output potential is not at unity. Using loop analysis on Figure 1-5,

$$i(t)R_L - \frac{Q_R(t)}{C_R(t)} + i(t)R_I + \frac{Q_L(t)}{C_L(t)} = 0$$

where

$$i(t) = \frac{dq(t)}{dt}$$

then

$$\frac{dq(t)}{dt} (R_L + R_I) = \frac{Q_R(t)}{C_R(t)} - \frac{Q_L(t)}{C_L(t)}.$$

Since we allow current to flow between the two EDL's, and if we assume no extra charge enters the system, thus,

$$Q_R(t) \equiv Q_R^0 - q(t) \text{ and } Q_L(t) \equiv Q_L^0 + q(t)$$

then

$$\frac{dq(t)}{dt} (R_L + R_I) = \frac{Q_R^0 - q(t)}{C_R(t)} - \frac{Q_L^0 + q(t)}{C_L(t)} \quad (1.6)$$

with boundary condition

$$q(t = 0) = 0.$$

Using Equation 1.6, the voltage across the load resistor can be predicted and is demonstrated in following chapters of this thesis. It should be noted that the above model has been adapted from Moon *et al.*, the first group to demonstrate such a device [18]. How they got there, and what has been done since by other groups is the topic of the next section.

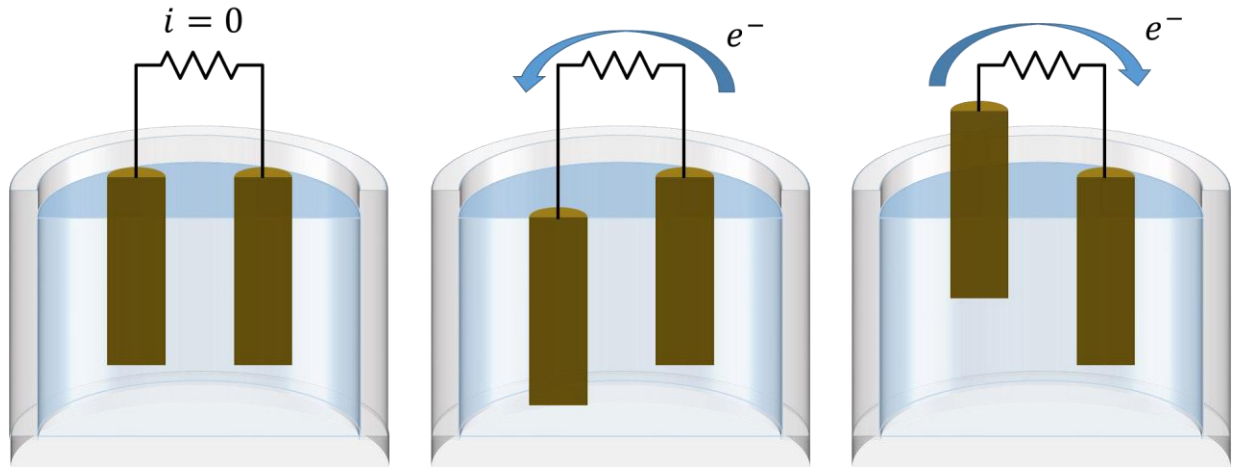


Figure 1-6 – EDL Transduction Cycle – Initially, the electrodes are at rest (left) and the potential across both EDL's is the same. As an electrode is dipped into solution (center), its EDL capacitance increases causing electrons to flow in the submerged electrode. When it is removed, the opposite happens as the EDL capacitance decreases with less surface area.

1.4 Literature Review

In 2011, the first electrostatic energy harvester using a solid-liquid interface as the variable-capacitor was demonstrated. Krupenkin and Taylor [19] used a droplet of mercury between two plates with one electrode treated by a coating of a high voltage breakdown dielectric followed by a thin coating of a hydrophobic material. An external bias of 80 V was applied and one electrode was vibrated in relation to the other. Although they did not utilize an EDL, this was more of a conventional parallel-plate capacitor with an electric field across a dielectric, it was the first example of using a liquid and varying the capacitance via surface area. They claimed power densities as high as 10^3 W m^{-2} , however, mercury being a poisonous heavy metal, limits its potential applications. It also still requires an external biasing source to generate power. A subsequent paper published a few years later addressed both of these problems.

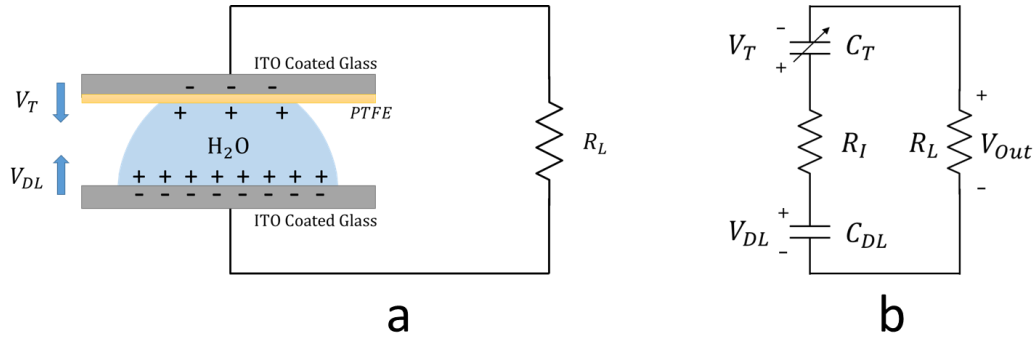


Figure 1-7 – Parallel Electrode EDL-Based Transducer – (a) The physical depiction of the device and its equivalent electrical circuit (b). (adapted from [18])

In 2013, Moon *et al.* demonstrated the first electrostatic energy harvester utilizing the EDL as the source of capacitance [18]. The setup is similar to Krupenkin’s, one electrode is held stationary and the other vibrated. The mechanism of transduction, however, is more akin to Section 1.3.

Figure 1-7 is a depiction of their setup. Equation 1.7 has been adapted below to accommodate the sign convention and variable names. Here, Q_{EDL}^0 and Q_T^0 are the initial charges on the bottom and top electrodes respectively and C_{EDL} and $C_T(t)$ are each interface’s capacitance; all the rest of the variables remain the same. It should be noted that in the case above, C_{EDL} is a constant and $C_T(t)$ is time varying. This sign convention and naming scheme applies to the remainder of the thesis.

$$\frac{dq(t)}{dt}(R_L + R_I) = \frac{Q_{EDL} - q(t)}{C_{EDL}} - \frac{Q_T^0 + q(t)}{C_T(t)} \quad (1.7)$$

In Moon’s setup, the top electrode, which is also coated with a thin layer of Teflon® AF, is held stationary while the bottom is vibrated. The purpose of the Teflon is to ensure that the electrodes wet differently; the top electrode will be hydrophobic and the bottom hydrophilic. As the

electrodes squeeze together, the interfacial surface area between the water droplet and the top electrode will get larger while the bottom interfacial surface area remains relatively constant. This is analogous to Section 1.3 where one electrode's surface area is changed in relation to another.

In addition to changing the wettability of the top electrode, the Teflon layer affects the interfacial capacitance at the top electrode. Immediately at the surface of the PTFE, an EDL can form [20, p. 211] with capacitance that can be estimated via Equation 1.4. The PTFE acts like a second capacitor in series that can be calculated using Equation 1.1 with d being the thickness of the layer. The net capacitance is the series combination of the PTFE capacitor, C_{PTFE} , and C_{EDL} , which can be found using

$$C_T = \left(\frac{1}{C_{EDL}} + \frac{1}{C_{PTFE}} \right)^{-1},$$

and since $C_{PTFE} \ll C_{EDL}$,

$$C_T \approx C_{PTFE}.$$

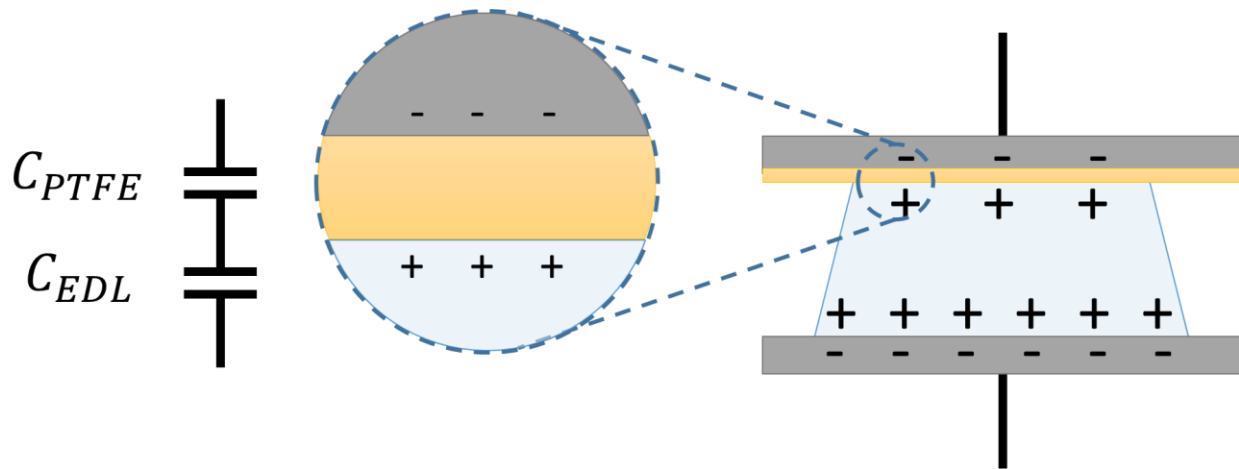


Figure 1-8 – Top Electrode Capacitance: Consists of two capacitors in series: a capacitor that forms across the PTFE-AF and one from the EDL that forms at the PTFE-AF’s surface (adapted from [18]).

Moon *et al.* demonstrated voltages of up to 8 V_{pp} using multiple droplets and even lit up LED’s using the transduction mechanism. One issue they identified was the limited frequency of the device. They claimed that at 30 Hz, splashing of the water droplet causes the voltage to drop off. To harvest energy from vibrations at higher frequencies, or to be used as a sensor past 30 Hz, this would have to be extended. To do this and to reduce the rate of evaporation, Wu *et al.* replaced the water droplet with hydrogel [21], [22]. They showed an increase in bandwidth, up to 80 Hz, and a reduction in evaporation rate. Another group used an ionic liquid as the electrolyte to address the evaporation issue and limited temperature range but also to see how it would affect power generation [23]. They observed a reduction in output power, attributing it to the ionic liquid’s viscosity. Others have used a similar transduction mechanism for converting raindrops to electricity [24]. As for assessing the usefulness of the mechanism for sensing, limited work has been done; one group has used it coupled with a thermogalvanic process, an electrochemical reaction that is dependent on temperature, to measure both temperature and pressure [25] and

another for underwater SONAR [26]. All of these works have been completed in the last three years, and because of this, there remains many unanswered questions that this thesis poses to answer.

1.5 Thesis Outline

This thesis is organized into five separate chapters. The following chapter, Chapter 2, is devoted entirely to explaining the experimental setup and techniques used. Chapter 3 investigates how vibrations applied to the top electrode affects bandwidth and presents a linearized approximation model that correctly predicts the point of maximum power transfer. Chapter 4 probes the origin of the biasing potential, V_{bias} , using a method also presented in this chapter. Finally, Chapter 5 concludes by reiterating the claims made and the work done. It also discusses future prospects and what needs to be accomplished for this technology to be a viable alternative for generation and sensing applications.

Chapter 2: Experimental Setup

This chapter describes the experimental setup used throughout this thesis. The chapter is split into six sections, with each section describing a piece of the experimental setup or method. These include device preparation, vibration source, data acquisition and interfacing electronics, surface area measurements and electrochemical techniques, data processing, and ends with a note on the repeatability of the measurements. All relevant code and schematics are included in the appendices.

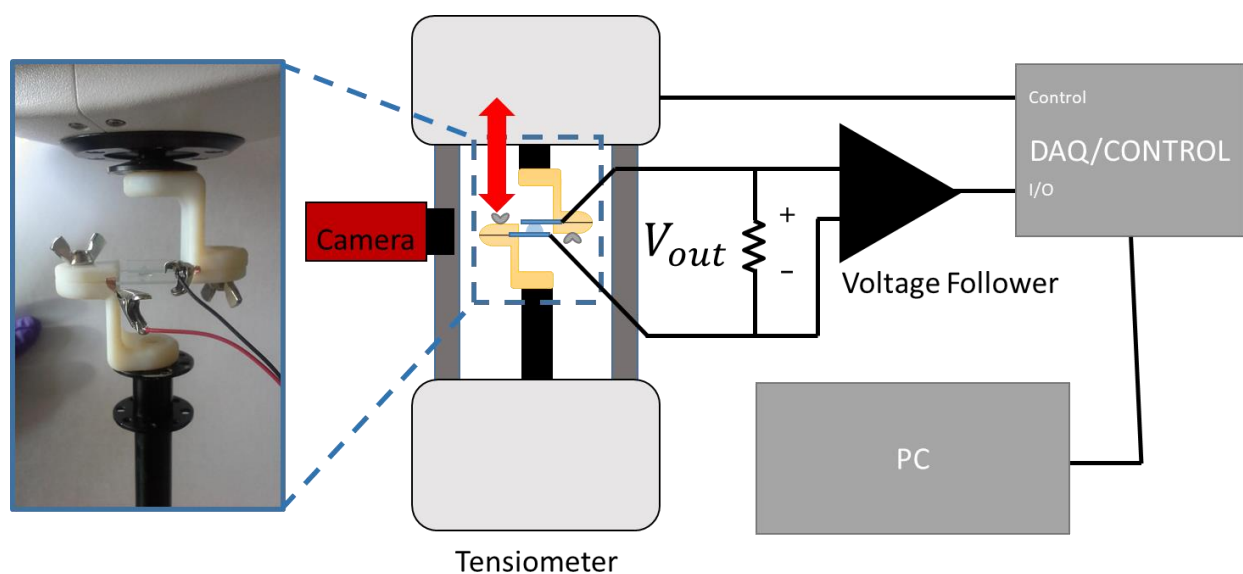


Figure 2-1 – Experimental Setup: Electrodes are prepared and placed in custom 3D-printed jigs that attach to the Bose ElectroForce 3100 tensiometer. A voltage follower buffers the signal where it is recorded at the DAQ system. A side-profile camera is used estimate the interfacial surface areas.

2.1 Device Preparation

In all experiments, the electrodes used are indium tin oxide (ITO) coated 25x25x1.1 mm glass slides purchased from Sigma-Aldrich (product number: 703176). ITO is used as it is completely

transparent and the interfacial surface area can be measured optically through the electrodes. Prior to use, the electrodes were first rinsed using ethanol and deionized water. The top electrode is then coated by 40 nm of the amorphous fluoroplastic, Poly[4,5-difluoro-2,2-bis(trifluoromethyl)-1,3-dioxole-co-tetrafluoroethylene], also known as PTFE-AF (Sigma-Aldrich, part number 469610-1G). PTFE-AF is ideal for this application as it is very hydrophobic and able to form extremely thin coatings.

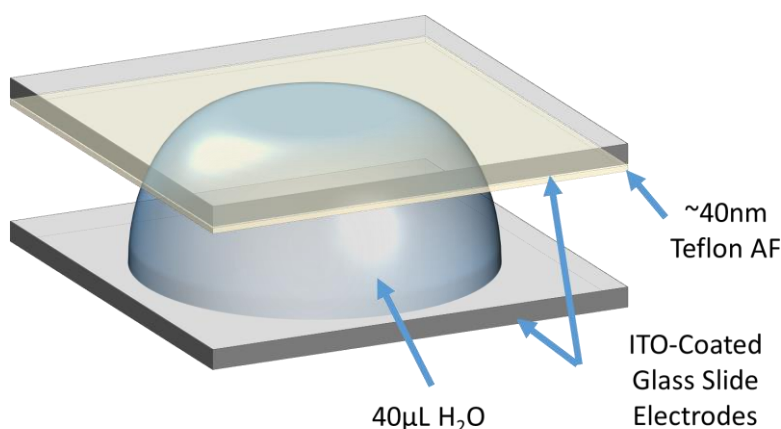


Figure 2-2 – Electrode Configuration – Each electrode is an ITO-coated glass slide with an approximately 40 nm PTFE-AF coating on the top electrode. 40 μL of ultrapure water is placed between the two electrodes.

The PTFE-AF films are prepared by first dissolving solid PTFE-AF in Fluorinert® FC-40 (Sigma-Aldrich, part number F9755-100ML), at 1 wt%. The solution is sonicated for four hours and filtered afterwards using a 0.45 μm PVDF syringe filter. 100 μL of the solution is pipetted onto an ITO glass slide spinning at 500 rpm, which is ramped to 2000 rpm for 45 seconds. The electrode is then left to air-dry for 15 minutes. Following the air-dry, the sample is placed on a hot plate and baked at 165°C for 10 minutes to remove the majority of the solvent. Baking the

sample at 330°C for an additional 10 minutes ensures an even coating and fills pin-holes. The baking is in accordance to DuPont's Teflon™ AF Adhesion Guide. Approximately a 5 mm strip of the PTFE-AF is removed using a razor blade to ensure proper electrical contact for the DAQ and for thickness measurements. A Dektak XT Profilometer is used to measure the thickness of the film and is found to be approximately 40 nm. These results are confirmed by electrochemical impedance spectroscopy (EIS) and simulations performed in following chapters. 40 µL of Milli-Q ultrapure water is used to maximize surface area change and minimize the rate of evaporation; any larger volume of water results in the droplet resembling more of a pancake shape. The droplets were pipetted using Gilson® Pipetman® Diamond D200 polypropylene tips. It should be noted that for each set of experiments new electrodes were prepared following the steps described above.

2.2 Vibration Source

The Bose ElectroForce 3100 is a tensiometer primarily used for material tests. It is able to apply perturbations of up to 5 mm spanning from very low frequencies up to 100 Hz. It is also supplied with a data acquisition (DAQ) system that precisely measures the mover's displacement in conjunction to input voltage signals.

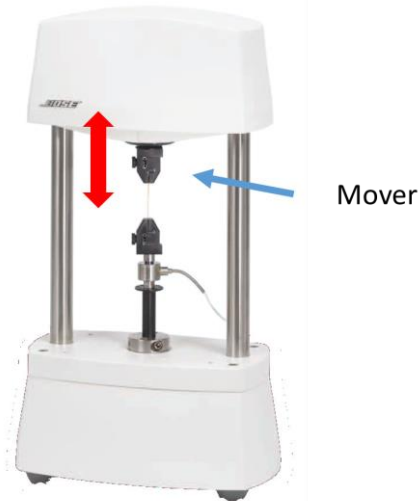


Figure 2-3 – Bose ElectroForce 3100 Tensiometer – Test equipment commonly used for mechanical characterization. In this case, however, it is used as a vibration source.

Electrodes are attached to the tensiometer via custom made 3D printed fixtures. Figure 2-4 shows the fixtures and electrodes without the hardware included. In all experiments, the applied oscillations are 0.25 mm in amplitude and the electrode-separation-offset is 1.25 mm, thus, the electrodes vary from 1.0 mm in separation to 1.5 mm. Any amplitude larger than 0.25 mm causes displacement clipping at higher frequencies. The offset of 1.25 mm is chosen because it is as close together as possible to maximize the change in the top electrode interfacial surface area without inducing one on the bottom. Copper tape is applied to the fixtures as contacts to the electrodes.



Figure 2-4 – 3D Printed Electrode Holders – 3D CAD drawings of holders designed using SolidWorks. Omitted from these drawings include hardware, specifically wingnuts and bolts for clamping the electrodes and connecting to the tensiometer.

2.3 Bose Interface and Experimentation Arduino-Shield Printed Circuit Board (PCB)

The electronics designed for this thesis's experiments are relatively demanding. The output impedance of the prepared devices is extremely high making it impossible to measure using the relatively low input impedance Bose DAQ. There are also three different experiments, each with their own requirements that need to be designed for. This section discusses why certain integrated circuits (IC's) were chosen and the design of a custom printed circuit board (PCB), dubbed the Bose Interface and Experimentation Arduino-Shield PCB. The PCB schematics and layout can be found in Appendix A

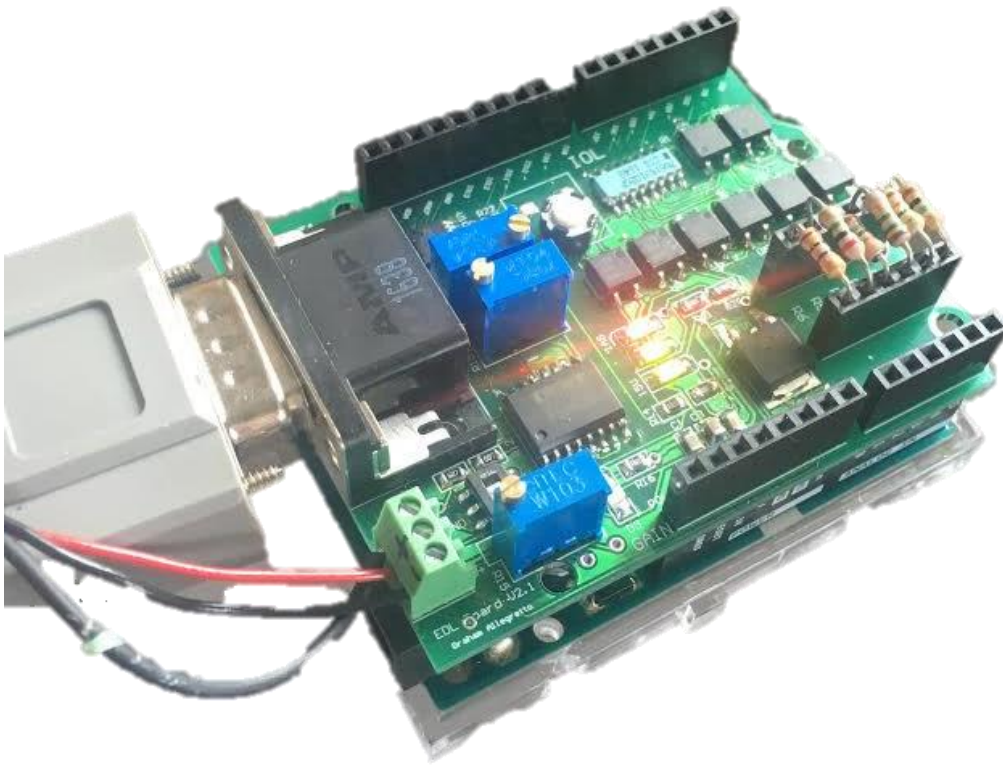


Figure 2-5 –Bose Interface and Experimentation Arduino-Shield PCB – This PCB performs various functions including signal buffering, load switching, and the application of a bias potential and gain.

2.3.1 Arduino Compatibility

The Arduino® electronics platform is an easy to use programmable prototyping device that is able to read and write digital and analog signals and can communicate with I²C devices. By designing a PCB that has the ability to be programmed, or can be interfaced to a programmable device, it becomes much more powerful and robust. Multistep procedures can be implemented without manual intervention and can be reprogrammed easily without requiring any changes in hardware. The PCB is therefore designed as an Arduino-Shield, able to mount directly onto an Arduino. Arduino source code, including a custom library for an I²C digital potentiometer, is included in Appendix B

2.3.2 Buffer Amplifier

Due to the high output resistance of the device, and the low input impedance of the Bose DAQ, a high impedance buffer amplifier is necessary to measure the generated potential without attenuating it. In addition, the load resistances can be upwards of $10\text{ M}\Omega$, thus, an input bias current as low as 10 nA can impart an error as high as 100 mV . This 100 mV would propagate through to the input causing a 100 mV bias applied across the device which could significantly affect the results. To address these issues, a Texas Instruments INA116 Ultra Low Input Bias Current instrumental amplifier was chosen as a buffer amplifier. This IC has a 3 fA input bias current and can be ran directly off the Bose DAQ that supplies $\pm 15\text{ V}$. This is important for convenience as well as being able to take advantage of the DAQ's entire input range of -10V to $+10\text{V}$. Gain can be enabled via a switch and a potentiometer. This amplifier is common for each of the three main experiments, however, each experiment has its own requirements and supporting circuitry.

2.3.3 Frequency Response

To measure the frequency response, the load resistance is held constant, usually at $10\text{ M}\Omega$, unless stated otherwise, while vibrations of 36 different frequency are applied, ranging from 0.1 Hz up to 100 Hz . This is the least demanding of tests for electronics and only requires the ability to enable a load resistor which is performed using a solid state relay (SSR). The Vishay VO1400AEFCT SSR was chosen because of its low on resistance and its ability to pass through a bipolar signal.

2.3.4 Point of Maximum Power Transfer

Measuring the point of maximum power transfer involves holding the frequency of oscillations constant while varying the load. The voltage across the load is measured which can yield the power the load dissipated. Five of the same SSRs specified in the previous section are used for turning on and off load resistors, providing 32 different possible resistor combinations. Resistors are chosen with the aid of a MATLAB script written to optimize the resistor choices for maximum resolution near the point of maximum power transfer. The script outputs a sequence of resistor combinations varying from high to low that can be copy-and-pasted directly into the Arduino code. The Arduino code enables the resistor combination for a predetermined amount of time before moving on to the next combination. This all occurs while vibrations are applied. Headers are used to make inserting and removing through-hole resistors easier as the point of maximum power transfer may be device dependent.

2.3.5 Bias Potential Investigation

For investigating the bias potential, V_{bias} , a known voltage is applied across the device during fixed-frequency vibrations to see how it affects the signal amplitude. A more detailed explanation of the circuitry can be found in Chapter 4. Two of the same SSR's identified earlier are used to connect a voltage divider consisting of the Microchip MCP45HV51 Digital Potentiometer to the device. The MCP45HV51 can be powered by ± 15 V, providing the same benefits identified in Section 2.3.2. It has 256 possible different resistance values, and being digital, can be operated by the Arduino. This allows for repeatable offset potential changes without having to manually set a potentiometer.

2.4 Capacitance and Surface Area Measurements

Prior to applying vibrations, the interfacial surface area of the top and bottom electrodes is estimated at maximum and minimum separation. These surface areas are used to assess the agreement between the model and empirical results and will be discussed further in Chapter 3. A short video of the profile of the device is captured using a camera recording at 60 fps and 640x480 resolution as the top electrode oscillates. Using a millimeter grid placed above the device, the surface area can be estimated by measuring the diameter of droplet and assuming a perfectly circular interface. The bottom two images show the droplets from a different perspective, supporting the perfect circle assumption.

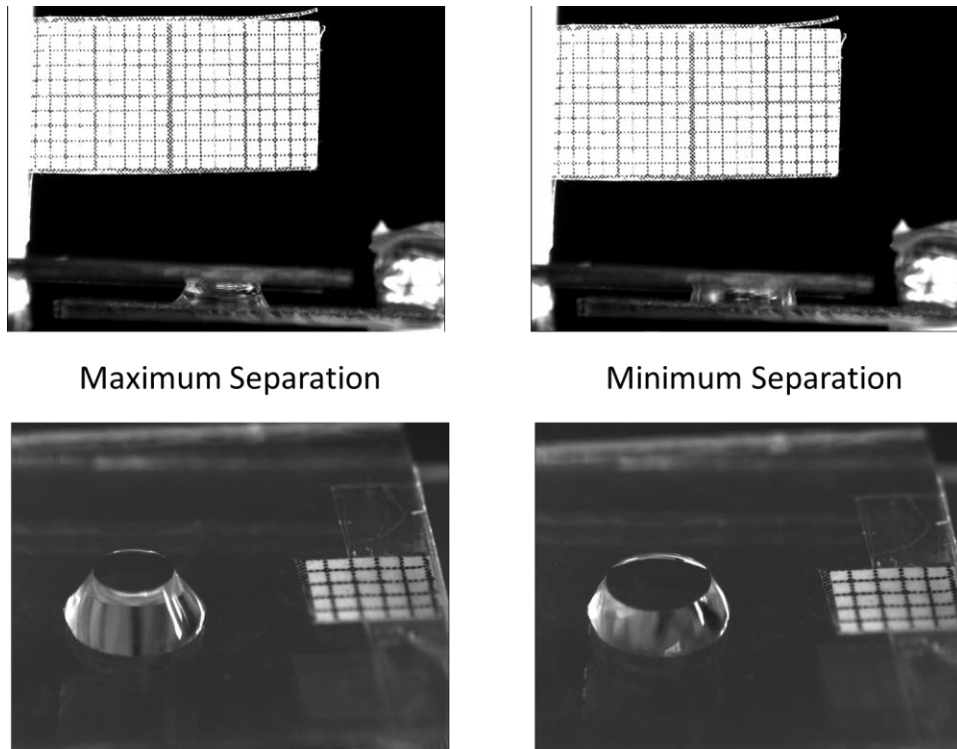


Figure 2-6 – Droplet Profile Views - Images on the left were taken when the plates are at their point of maximum separation while images on the right are when they are closest together. The diameter is taken using the top images to estimate surface area assuming the interfaces are perfectly circular. The bottom images were taken at approximately a 30° angle and prove the circular interface assumption for both extremes.

EIS measurements are taken via a Solartron SI 1287 potentiostat to confirm resistance and capacitance values used in the simulation. Custom 3D printed jigs at a separation of 1.0 mm and 1.5 mm were made for this purpose.

2.5 Data Analysis

Data captured by the Bose DAQ contains a time stamp, output potential, and the location of the tensiometer’s mover, also known as the mover’s *throw*. Although valuable for this device, the comparison of how much the top electrode moves to the voltage signal does not apply to

different configurations. To provide more universal results, the throw is converted to a surface area signal, allowing it to be used as an input for a simulation as well. Figure 2-7 shows how the top interfacial surface area, as calculated by the method described previously, varies as a 0.25 mm amplitude vibration is applied to the top electrode.

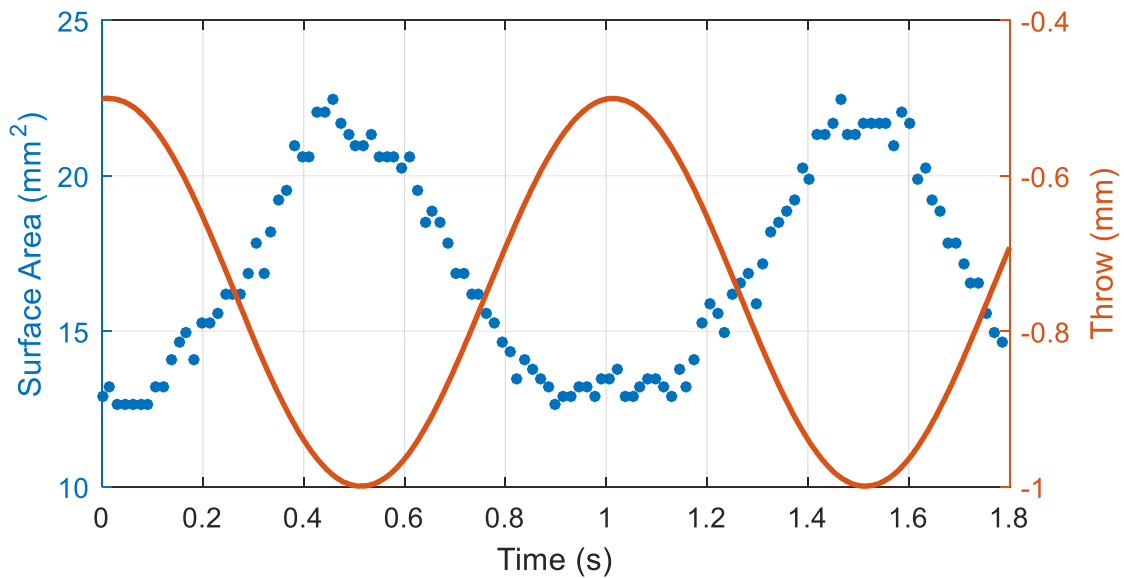


Figure 2-7 - Surface Area Measurement – This plot shows the change in interfacial surface area between the droplet and top electrode as a 0.25mm sinusoidal vibration is applied to the top electrode. Although the surface area response is not perfectly sinusoidal, it is assumed for subsequent calculations that surface area and electrode displacement is linearly related.

As the throw becomes more negative, the top plate moves farther down and the separation of the electrodes decreases. Thus, at the throw's minima the surface area will be a maximum, and vice versa. A surface area signal, shown in Figure 2-8 (bottom), is estimated by multiplying the throw signal by negative one and ensuring that it varies between the maximum and minimum surface area values measured earlier.

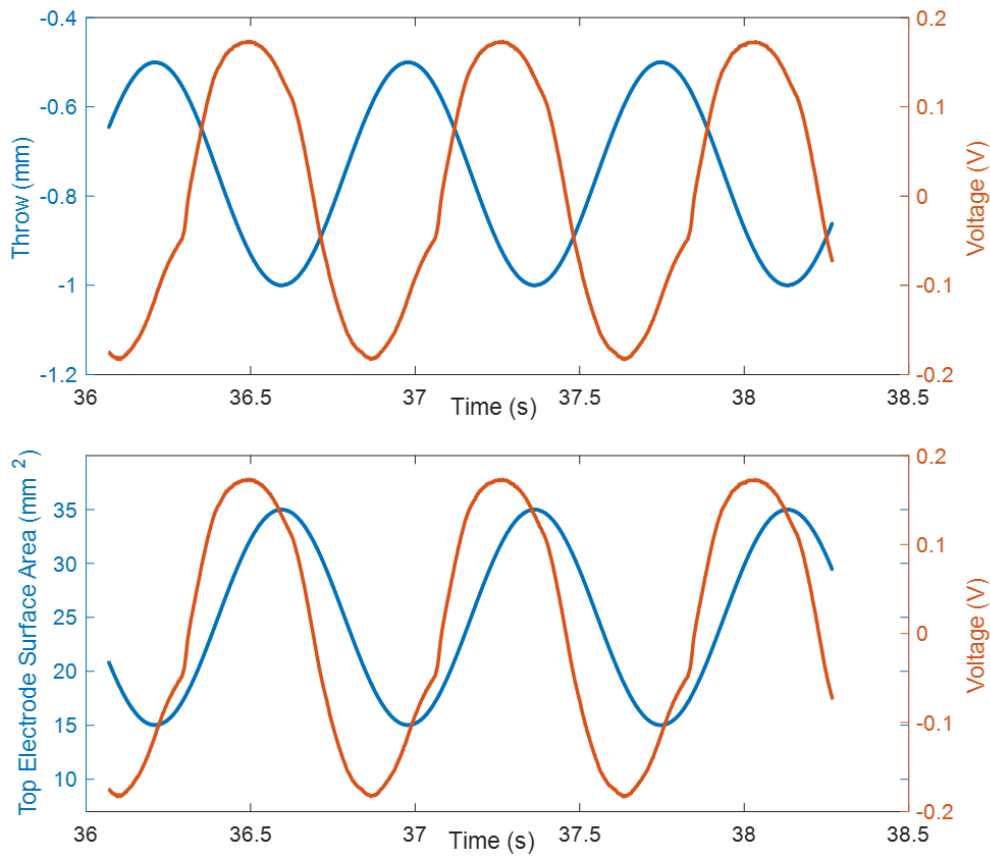


Figure 2-8 – Transforming Mover Throw to Surface Area – Assuming surface area is directly related to throw, a surface area signal is estimated using droplet surface area measurements using the camera and the process explained above.

Once the previous transformation is performed, the signal can be further processed and analyzed. All data processing is handled by MATLAB including the procedure above. Transfer function measurements are performed by curve fitting a sinusoid to the data by least squares sense. Peak-to-peak amplitude based response matches the sinusoidal fitting up to approximately 80 Hz, beyond this, there is some deviation between amplitude measured by peak-to-peak measurements

and that of curve fitting. This possibly indicates inertial effects. The fitting MATLAB code is included Appendix C .

2.6 A Note on Repeatability

All experiments performed are easily repeated, however, there are some procedures that require extra care to ensure consistent results. First of all, for an experiment to yield similar results as a previous experiment, droplets had to be placed at the exact same location on the same sample. This indicates that the PTFE layer may not be completely uniform due to inconsistent spin coating. Specifically for Chapter 4, it was important to use only freshly baked PTFE electrodes as V_{bias} measurements tended to increase over time. This will be further discussed in Chapter 4.

The experimental setup and techniques discussed in this chapter are used in the remainder of this thesis unless stated otherwise. In the following chapter, the Bose Interface and Experimentation Arduino-Shield PCB is used to measure the frequency response and point of maximum power transfer. In Chapter 4, more frequency response measurements are performed and the motivation behind the biasing circuit introduced in Section 2.3.5 is discussed. The technique is then applied to understand the origin of the device's self-biasing properties.

Chapter 3: Frequency Response and Linear Model

In this chapter, we investigate different perturbation methods including applying vibrations to the top electrode. Data is presented as a conventional Bode plot, making this thesis the first instance in literature to do so. This chapter also presents a linearized approximation model that clearly shows the relationship between various device parameters. Using this model, we present a method of calculating the point of maximum power and demonstrate its accuracy by comparing the predicted value to empirical results.

3.1 Experiment

The frequency response is calculated by applying 36 different frequencies, spanning from 0.1 Hz to 100 Hz at equal logarithmic spacing. At low frequencies, a minimum of 10 cycles are performed per frequency ranging up to 100 cycles closer to 100 Hz. All other experimental parameters follow those described in Chapter 2 unless stated otherwise. Included in Appendix C is the finite-element source code used to simulate Equation 1.7.

3.2 Results

The Bode plot is shown in Figure 3-1. Experimental results (x) are in good agreement with simulated values, depicted as a blue line. The inset shows a comparison between a measured and simulated signal using surface area estimations and capacitance measurements taken by the methods discussed in Section 2.4. The most significant result of the Bode Plot is the lack of signal degradation at higher frequencies. At up to 100 Hz, the signal remains more or less constant. Another surprising result is the first-order, high-pass response of the system.

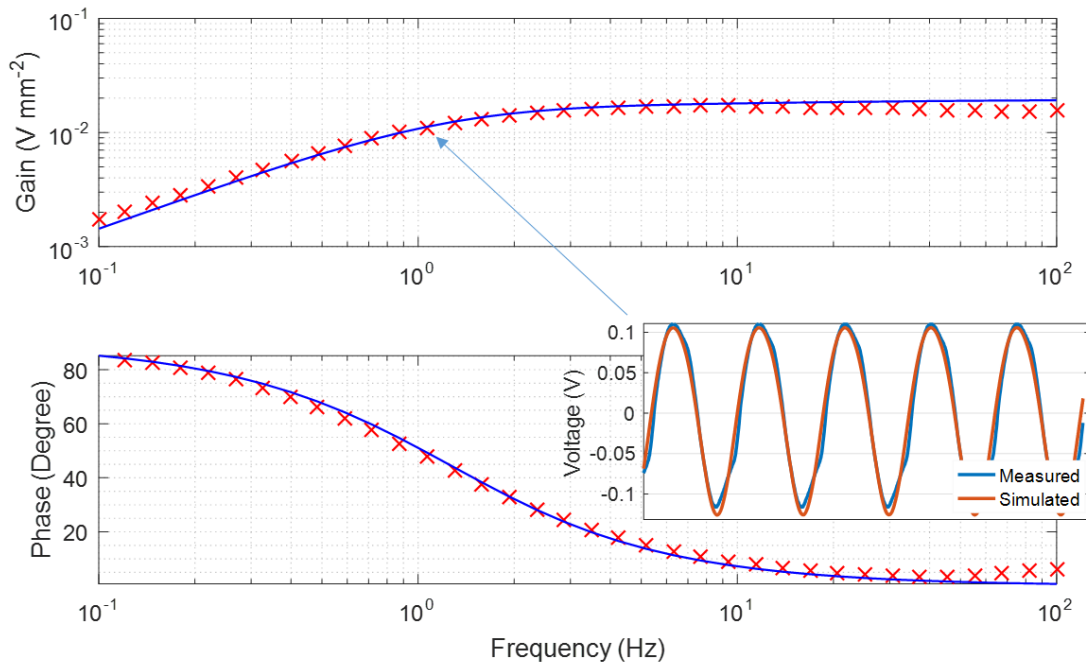


Figure 3-1 – Standard Device Bode Plot: The inset shows a comparison of the measured response to simulated at approximately 1 Hz. At each frequency point, a signal is simulated and compared to measured response. In the above plot, the maximum peak-to-peak voltage was measured to be 555 mV_{pp},

Although relatively hidden by Equation 1.7, upon closer inspection, Figure 3-1 can be justified. At low frequencies, the voltage induced from the change in capacitance of the top electrode discharges at a faster rate than the vibrations are applied. The charge that moves between the electrodes has ample time to equilibrate the changes in voltage, thus, only a small amount of current is driven across the load resistor. The charge transferred per cycle also only depends on the maximum and minimum capacitance values in this regime and is therefore constant. This indicates that current, and voltage across the load resistor, is directly proportional to frequency. This is the source of the slope of 1 at low frequencies of the magnitude response which is conducive to a first-order high phase response.

The 90° phase lead can be explained by examining the sign convention and considering what happens to the charge at the top capacitor. As the plates are separated, the top interfacial surface area decreases causing charge to concentrate at the top interface. In this frequency regime however, the resistance is small compared to the rate of change in capacitance and the connection between the two capacitors can be considered as a short. Charge is simply forced out of the top capacitor; the charge per area, and therefore voltage, stays relatively constant. Thus, the amount of charge that leaves the top capacitor will depend on the rate of interfacial surface area change. The opposite happens as the plates are brought together: the concentration of charge in the top capacitor decreases allowing charge to flow from the bottom capacitor to equalize the concentrations. Since current is a measure of the amount of charge flowing through a point for a given time, this is equivalent to saying that current is dependent on the rate of change of the capacitance of the top capacitor. Noting that conventional current is opposite to the flow of electrons, and using the sign convention of Figure 3-2a,

$$i(t) = \frac{dC_T(t)}{dt}.$$

If the surface area, and therefore capacitance, is sinusoidal, the phase of the current will lead by 90° . The measured voltage will be in phase with current and lead surface area by 90° as

$$V_{out}(t) = i(t)R_{load} = \frac{dC_T(t)}{dt}R_{load}$$

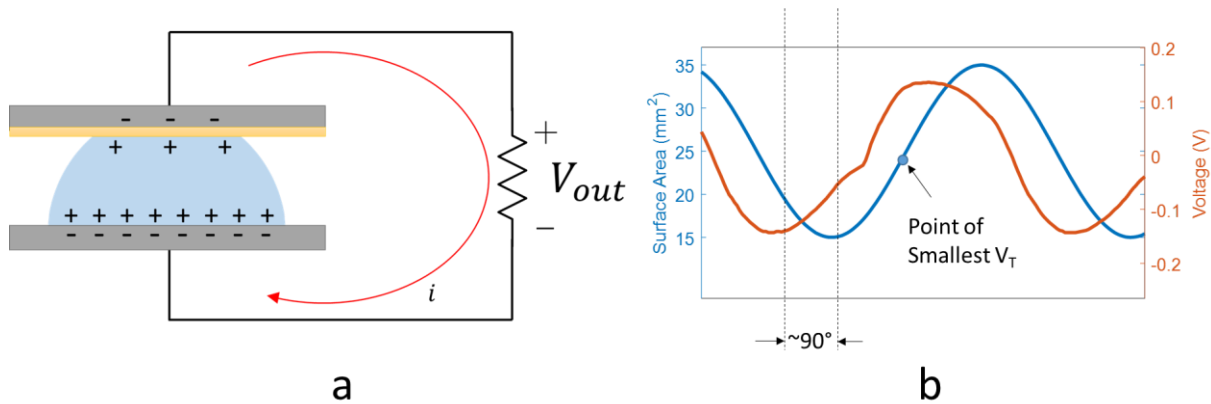


Figure 3-2 – Low Frequency Perturbation – (a) is the sign convention used and (b) shows a typical wave. It should be noted that the point of smallest V_T will yield the largest V_{out} .

Figure 3-2b demonstrates the 90° phase lead of voltage in reference to surface area. The same plot shows non-linearities in the voltage signal that occur at surface area minima. At these points, the rate of surface area change is at a minimum, causing more pronounced contact angle pinning. This can even be seen in Figure 2-7 as an extended minima.

As frequency increases past a certain threshold, the magnitude response flattens out and the phase approaches 0° . The load resistor impedes the charge's ability to move such that it cannot compensate the changes in voltage across the top electrode as the RC time constant is too long. Now, the vibrations are faster than the capacitors can discharge. The system drives little current through the load resistor and the output voltage is due to the changes in capacitance, as in Equation 1.5. After careful consideration of Equation 1.7, it becomes apparent that the frequency response can in fact follow a first order response. This however is not trivial and is addressed in a following section. Arguably, the more significant result revealed by the Bode Plot of Figure 3-1 however is the lack of a decay in signal at higher frequencies.

3.3 Increase in Bandwidth

One possible explanation as to why the bandwidth is so much larger in these results than those reported by Moon *et al.* is that, in this study, vibrations are applied to the top electrode rather than the bottom. In Moon *et al.*'s paper, they claim the mechanism that limits bandwidth is splashing; as soon as splashing occurs, performance suffers [18]. The hypothesis is that vibrations applied to the bottom electrode accelerates the entire droplet. At higher frequencies, the acceleration is so great that the droplet can be thought as being thrown against the top electrode which could very possibly impart splashing. If the top electrode is vibrated, only a portion of the droplet will be accelerated, perhaps causing the frequency the onset of splashing occurs to increase. Another possible cause may be due to the separation distance between the electrodes. In Moon's original experiment this parameter is not specified. To determine which of these two experimental parameters, if any at all, contributed to an increase in bandwidth, two tests were carried out. The first, testing whether vibrations applied to the top electrode improved results, was performed by simply applying vibrations to the bottom electrode and comparing them to the original results. The second set of experiments tested the effects of plate separation distance.

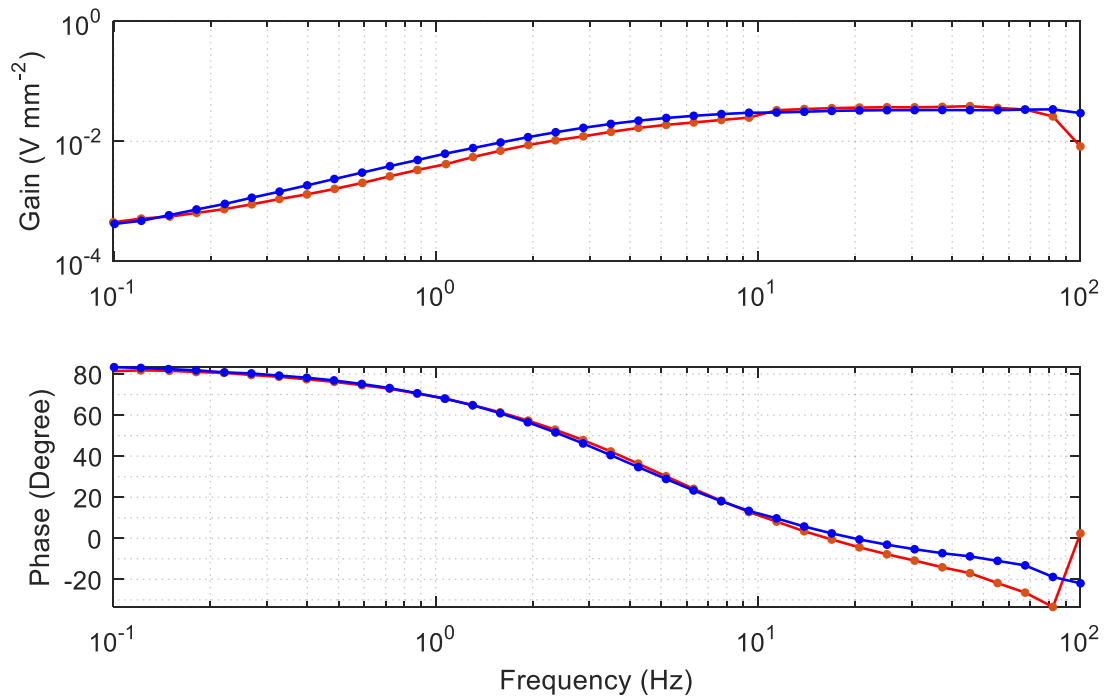


Figure 3-3 – Perturbations of Top vs. Bottom Electrode Gain Phase Log-Log Plots – Plots comparing the frequency response of perturbing the bottom electrode (orange) to the top electrode (blue).

Figure 3-3 shows the results of vibrating the bottom electrode in comparison to the original setup where the top electrode is vibrated. Although not conclusive, these results indicate that electrode configuration does not affect bandwidth. Figure 3-4 on the other hand shows an inverse correlation between plate separation distance and bandwidth. As the electrode offset distance is increased, its higher frequency signal magnitude starts to decay. One possible reason could be that due to the reduced contact between the droplet and the top electrode, the stability of the droplet decreases causing the onset of splashing to occur at a lesser frequency. Although not entirely clear from Figure 3-4, voltage amplitude tends to increase with smaller separation distances. Peak-to-peak potentials as high as 892 mV were measured for separation distances of 0.85 mm. Figure 3-4 also revealed that knee frequency depends on plate separation distance.

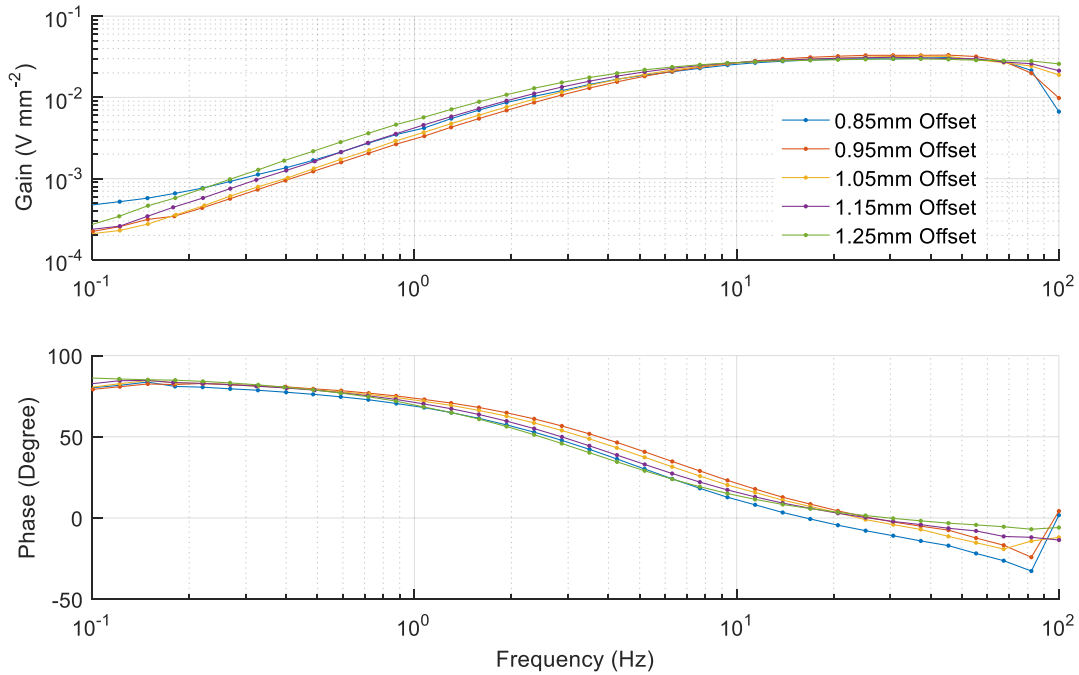


Figure 3-4 – Varying Electrode Separation Offset Distance Bode Plot – Bode Plot comparing different plate separation distances using identical droplet size and vibration amplitude. Peak-to-peak voltages as high as 892 mV were obtained by placing the electrodes at a separation distance of 0.85 mm.

Understanding why potential amplitude and knee frequency depends on electrode separation offset distance is not trivial. As the electrodes come closer together, more of the top electrode is wetted and the average capacitance of its interface increases. The change in capacitance could possibly increase at closer offset distances as well. Knowing this, Equation 1.7 offers little help. Since it is a non-linear differential equation, it makes it very difficult to gain any insight without running numerical simulations. To understand this relationship amongst others, and how to optimize future devices, a linear approximation model was developed.

3.4 Linear Model Derivation

To begin, we start with the original model as depicted in Figure 1-7. Using loop analysis, a modified equation for the output voltage of the circuit is

$$V_{out}(t) = i(t)R_L = \frac{Q_{EDL}(t)}{C_{EDL}} - \frac{Q_T(t)}{C_T(t)} - i(t)R_I, \quad (3.1)$$

where

$$Q_T(t) = Q_T^0 + q(t),$$

$$Q_{EDL}(t) = Q_{EDL}^0 - q(t),$$

$$C_T(t) = C_T^A A_T(t), \quad (3.2)$$

and

$$A_T(t) = A_T^0 + \Delta A \sin(\omega t). \quad (3.3)$$

Q_T^0 is the initial charge on the top electrode, Q_{EDL}^0 is the initial charge on the bottom electrode, C_T^A is the capacitance per area of the top electrode, ω is the angular frequency of the applied vibration, $A_T(t)$ is the interfacial area of the top electrode, A_T^0 is the average of the interfacial area of the top electrode over one cycle and ΔA is the change in area. To create a linear approximation, we assume $\frac{\Delta A}{A_T^0}$ is small.

The voltage across the top interface is

$$V_T(t) = \frac{Q_T(t)}{C_T(t)}. \quad (3.4)$$

Inserting Equations 3.2 and 3.3 into 3.4 yields

$$V_T(t) = \frac{Q_T(t)}{C_T^A (A_T^0 + \Delta A \sin(\omega t))} = \frac{Q_T(t)}{C_T^A A_T^0 (1 + \frac{\Delta A}{A_T^0} \sin(\omega t))}.$$

For small $\frac{\Delta A}{A_T^0}$ and defining $C_T^A A_T^0 \equiv C_T^0$,

$$V_T(t) \cong \frac{Q_T(t)}{C_T^0} \left[1 - \frac{\Delta A}{A_T^0} \sin(\omega t) \right].$$

Then

$$V_{out}(t) = \frac{Q_{EDL}^0 - q(t)}{C_{EDL}} - \frac{Q_T^0 + q(t)}{C_T^0} \left[1 - \frac{\Delta A}{A_T^0} \sin(\omega t) \right] - \frac{dq(t)}{dt} R_I,$$

Assuming that prior to an applied vibration the voltages are equal across each capacitor,

$$V_{EDL} = \frac{Q_T^0}{C_T^0} = \frac{Q_{EDL}^0}{C_{EDL}},$$

then the above equation can be expanded to,

$$V_{out}(t) = \left(V_{EDL} - \frac{q(t)}{C_{EDL}} \right) - \left(V_{EDL} + \frac{q(t)}{C_T^0} \right) + \frac{\Delta A}{A_T^0} \sin(\omega t) \left(V_{EDL} + \frac{q(t)}{C_T^0} \right) - \frac{dq(t)}{dt} R_I,$$

resulting in

$$V_{out}(t) = -\frac{q(t)}{C_{EDL}} - \frac{q(t)}{C_T^0} + \frac{V_{EDL} \Delta A}{A_T^0} \sin(\omega t) + \left(\frac{q(t)}{C_T^0} \right) \left(\frac{\Delta A}{A_T^0} \right) \sin(\omega t) - \frac{dq(t)}{dt} R_I.$$

Also, assume that $C_{EDL} \gg C_T^0$ due to the presence of the PTFE layer at the top electrode. This

allows for the removal of the $\frac{q(t)}{C_{EDL}}$ term. Since we are also assuming a small ΔA , this indicates

that there should be little charge that moves between the two electrodes, or $q(t) \ll Q_T$. Both $\frac{q(t)}{C_T^0}$

and $\frac{\Delta A}{A_T^0}$ will therefore be small, and since they are multiplied, their product will be even smaller.

This allows for the removal of the $\left(\frac{q(t)}{C_T^0} \right) \left(\frac{\Delta A}{A_T^0} \right) \sin(\omega t)$ term, resulting in:

$$V_{out}(t) \cong V_{EDL} \left[\frac{\Delta A}{A_T^0} \sin(\omega t) \right] - \frac{q(t)}{C_T^0} - \frac{dq(t)}{dt} R_I = \frac{dq(t)}{dt} R_L,$$

which can be rearranged to

$$\frac{dq(t)}{dt} (R_I + R_L) = V_{EDL} \left[\frac{\Delta A}{A_T^0} \sin(\omega t) \right] - \frac{q(t)}{C_T^0}. \quad (3.5)$$

If we define,

$$V_{sense}(t) \equiv V_{EDL} \left[\frac{\Delta A}{A_T^0} \sin(\omega t) \right], \quad (3.6)$$

we can combine equations 3.5 and 3.6 results in

$$V_{sense}(t) = \frac{dq(t)}{dt} (R_I + R_L) + \frac{q(t)}{C_T^0}. \quad (3.7)$$

After converting equation 3.6 and 3.7 to the frequency domain,

$$V_{sense}(j\omega) = I(j\omega)(R_I + R_L) + \frac{I(j\omega)}{j\omega C_T^0}.$$

This can be rearranged for $I(j\omega)$:

$$I(j\omega) = \frac{V_{sense}(j\omega)}{R_I + R_L + \frac{1}{j\omega C_T^0}}, \quad (3.8)$$

resulting in the measured output voltage of

$$\frac{V_{out}(j\omega)}{V_{sense}(j\omega)} = \left(\frac{j\omega R_L C_T^0}{j\omega C_T^0 (R_I + R_L) + 1} \right). \quad (3.9)$$

Equation 3.9 provides insight into the relationship between output voltage and various parameters that would not as easily be deduced using Moon's model. It also can be used to predict the frequency response of such a system and could prove to be useful in the design of a

droplet based sensor. Two equivalent electrical circuit representations of the Equation 3.9 are shown in Figure 3-5. They yield identical results

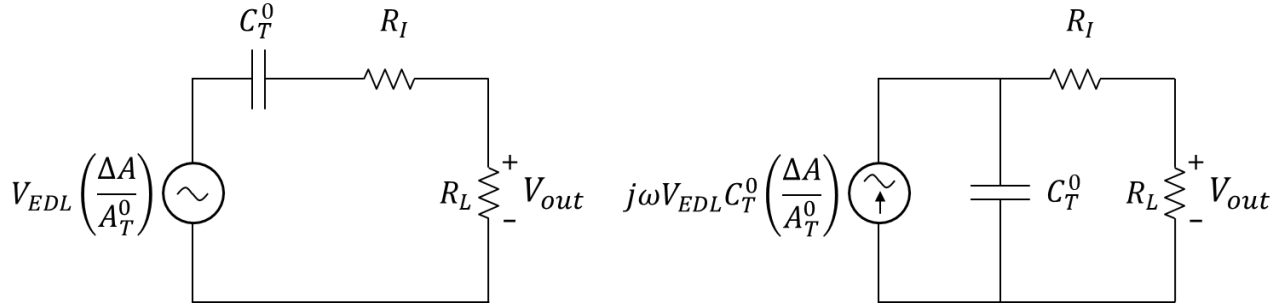


Figure 3-5 – Linear Approximation Model Equivalent Electrical Circuits – Both models represent Equation 3.9 and are equivalent.

Using Equation 3.9, the cut-off frequency can be obtained,

$$f_{knee} = \frac{1}{C_T^0(R_I + R_L)}, \quad (3.10)$$

as well as the phase and magnitude response,

$$\angle V_{out}(j\omega) = \tan^{-1} \frac{1}{\omega C_T^0(R_I + R_L)}, \quad (3.11)$$

and

$$|V_{out}(j\omega)| = \frac{\omega R_L \Delta C_T V_{EDL}}{\sqrt{1 + [\omega(R_I + R_L)C_T^0]^2}}. \quad (3.12)$$

3.5 Discussion

To construct the linear approximation model it was assumed that the change in capacitance (ΔC_T) of the top electrode is small in relation to its rest capacitance (C_T^0). That being said, its

error should increase as a function of the ratio of ΔC_T to C_T^0 . To test the accuracy of the model and its sensitivity to this assumption, $\frac{\Delta C_T}{C_T^0}$ was varied and compared to Moon's model. At small ΔC_T 's, the linear model follows Moon's quite closely. As ΔC_T grows, however, the two models diverge.

Figure 3-6 compares the two models, ranging from a ten percent surface area change up to 80%. At low surface area changes, the models are in good agreement. At approximately 40% surface area change, the models start to diverge. Although the peak-to-peak voltages are close, an offset is imposed on the non-linear model and the phases are not in perfect agreement. The most bottom plot shows an 80% surface area change. Here, the nonlinearity of Moon's model starts to present itself, with a greater than expected voltage drop.

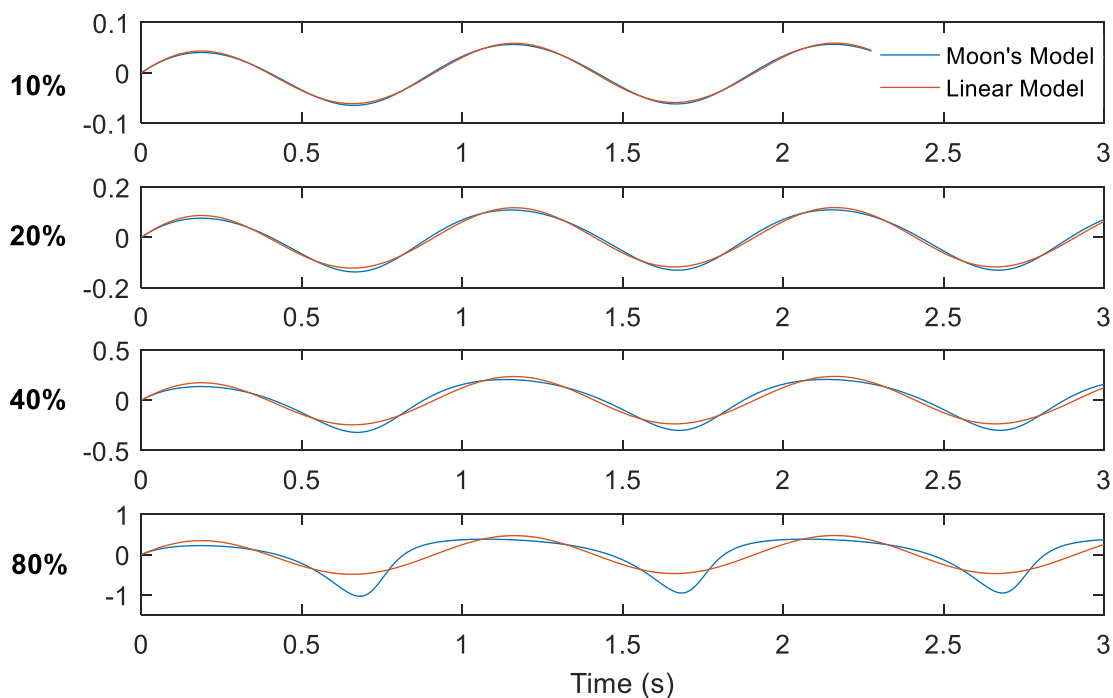


Figure 3-6 – Time Domain Comparison of Models for Varying Relative Changes in Capacitance – Each plot shows the output of the two models for varying relative changes in surface area. At 10% relative change, the models show good agreement. The linear model loses its ability to predict response at higher surface area changes.

In the frequency domain, considering just signal amplitude and phase, the model performance follows a similar trend as demonstrated above. Figure 3-7 shows the magnitude response of Moon's model, dotted lines in the figure, with respect to the linear model which are depicted with solid lines. Amplitude is determined by fitting the simulated voltage response with a sine wave. As can be seen below, for small changes in interfacial surface area the two models are in good agreement. Even for larger changes in amplitude the models relatively agree up until the knee frequency that can be calculated by Equation 3.8. The linear increase in Moon's model at frequencies greater than 10 Hz, and more pronounced at larger changes in surface area, has yet to be observed experimentally. This is left as further work.

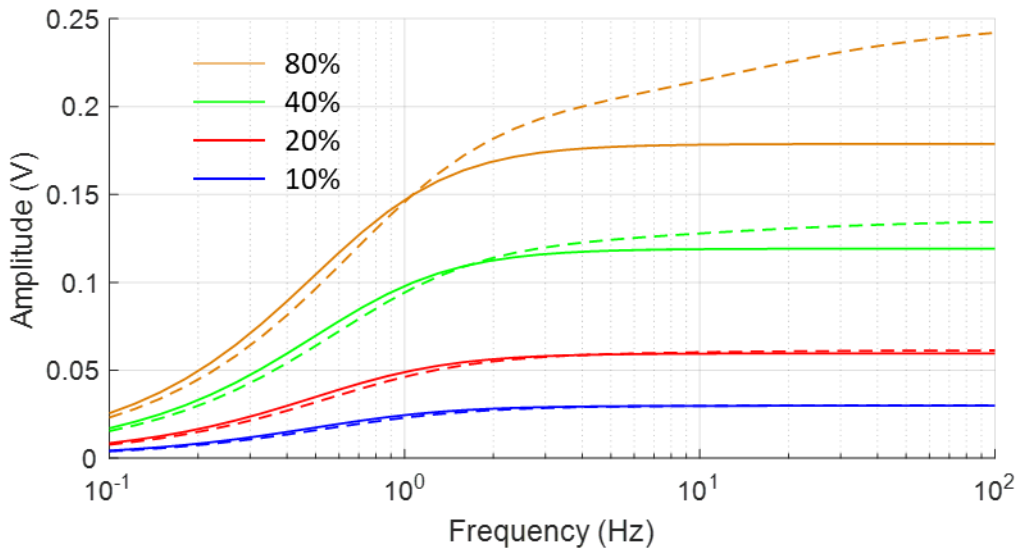


Figure 3-7 – Frequency Domain Signal Amplitude Comparison of Models – Simulation results comparing the two models in the frequency domain.

As long as the frequencies do not get too high, nor the changes in capacitance too large, the linear model predicts the response of the device relatively accurately. One additional benefit that the linear model provides that Moon's cannot easily perform is the analytical prediction of the point of maximum power transfer. A critical calculation if these are ever to be used as actual energy harvesters.

3.5.1 Point of Maximum Power Transfer Prediction

The amount of power dissipated across a purely resistive load is simply current multiplied by the voltage drop, or $P = IV$. Batteries and generators are also governed by this equation; however, the amount of power they can deliver is finite. An infinite current cannot be drawn at a given potential; as more current is drawn, the potential drops. For every power source there is a load impedance that maximizes power delivery such that voltage multiplied by current is a maxima.

Figure 3-8, for example, shows the power curve for different load resistors and frequencies, where the triangles are experimental results and the solid lines are predicted values using the model developed in this chapter. For the 20 Hz and 25 Hz curves, it is apparent there is an obvious point where the average power comes to a peak. The load resistance at this point is called the point of maximum power transfer. To determine this point analytically, a model that includes the internal resistance of a power source is necessary, such as Equation 3.12.

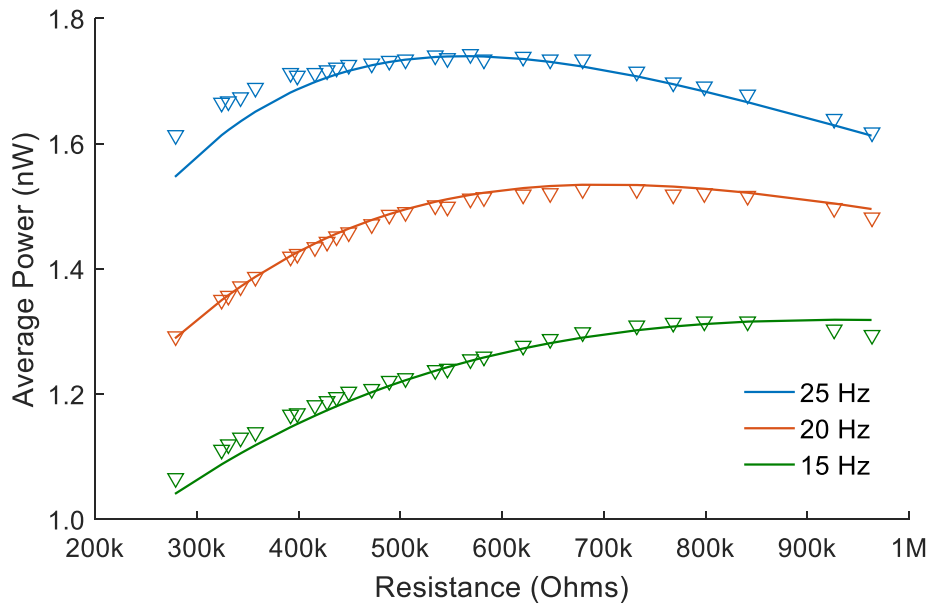


Figure 3-8 – Moon Device Power Curves: Solid lines are simulations using the linear approximation model and triangles are experimental measurements.

The average power a sinusoidal voltage with amplitude V dissipates across a resistor, R , can be determined by the equation

$$P_{avg} = \frac{1}{2} \frac{V^2}{R} \quad (3.13)$$

Substituting Equation 3.12 into 3.13 results in

$$P_{avg}(R_L, \omega) = \frac{1}{2} \frac{|V_{out}(j\omega)|^2}{R_L} = \frac{\omega^2 R_L \Delta C_T^2 V_{EDL}^2}{2(1 + [\omega(R_L + R_I)C_T^0]^2)}. \quad (3.14)$$

Equation 3.14 provides the average power the device will supply for a given load and frequency.

To determine the point of maximum power transfer, the partial derivative of Equation 3.14 is taken with respect to R_L and set to zero. Solving for R_L yields the load resistance that delivers the highest power.

$$\frac{\partial P_{avg}(R_L, \omega)}{\partial R_L} = 0 = \frac{\omega^2 R_L \Delta C_T^2 V_{EDL}^2}{2(1 + [\omega(R_L + R_I)C_T^0]^2)}$$

$$R_{MaxP} = \sqrt{\frac{1}{(\omega C_T^0)^2} + R_I^2} \quad (3.15)$$

Equation 3.15 estimates a device's point of maximum power transfer, R_{MaxP} . This calculation could prove extremely useful for tuning an EDL based energy harvester's load, optimizing the power extracted for a target frequency. It also illustrates how the electrolyte starts affects the generated power at higher frequencies. If a device is designed to harness vibrations of 100's of Hz, the concentration of the solution starts to play a significant roll.

Figure 3-9 shows the predicted points of maximum power transfer, based on Equation 3.15, overlaid on top of experimental results. Although not perfect, Figure 3-9 demonstrates the ability this method has for determining the load resistance to deliver the maximum amount of power for a given frequency. It should be noted that further improvements in power extraction can be made by adding an inductive element.

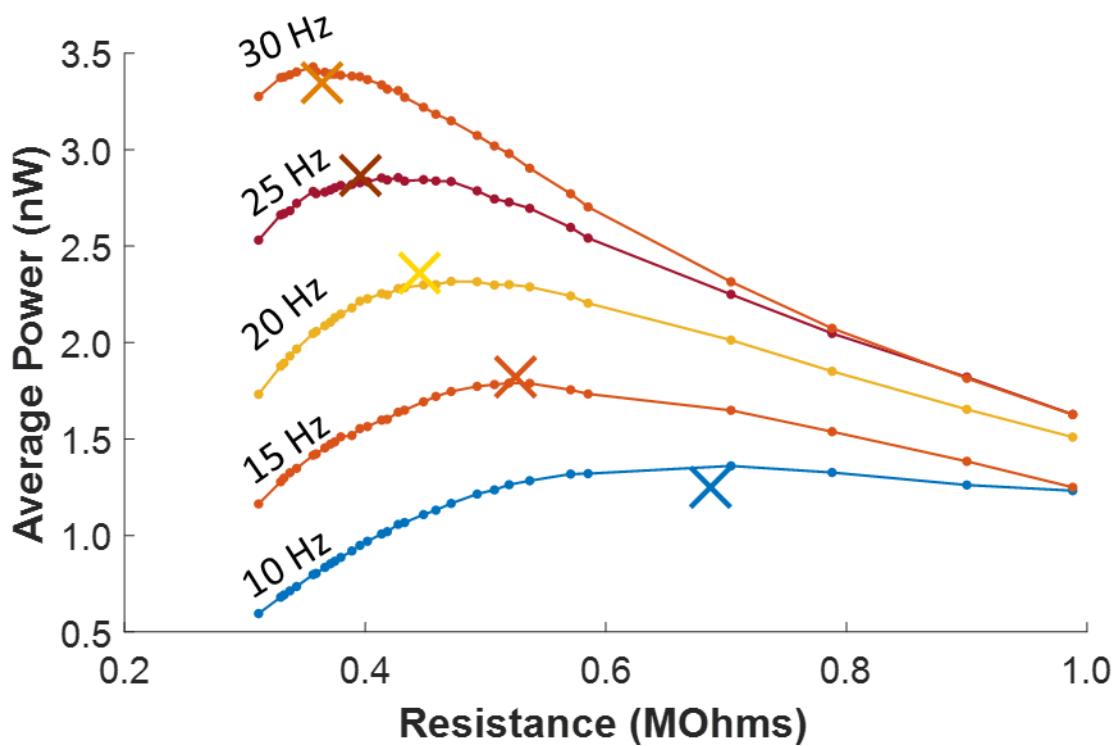


Figure 3-9 – Point of Maximum Power Transfer Prediction

3.6 Conclusion

One of the benefits of the linear model presented in this chapter is that it shows direct relationships. It identifies which parameters would require to be tuned for a given application. If a device were being designed as a high-pass sensor for example, Equation 3.9 would help in picking a resistor value such that low-frequency vibrations would be properly attenuated. It can also be used to determine what load value would deliver the most power for a vibrational-energy harvester. But arguably the most significant contribution of this model to device development is that it clearly shows how to increase output voltage.

The following chapter reassess how the devices self-bias. Until now, the theory was that the EDL drives electrons into the top interfacial capacitor via a biasing potential denoted V_{EDL} . Chapter 4, however, considers effects that may occur at the PTFE-water boundary. Since an alternative mechanism may be the dominant biasing mechanism, for the remainder of the thesis the biasing source V_{EDL} will be replaced with V_{bias} to accommodate the other possible mechanism. It also more closely follows the convention of electrostatic energy harvesters discussed in Chapter 1.

Chapter 4: Origin of V_{bias}

According to the current understanding of the sensor/generator technology, a device's output potential, as described in the preceding chapter, is directly related to two parameters: the rest potential across the PTFE capacitor, V_{bias} , and its net change in capacitance, ΔC_T . Whether a device is a sensor or generator, the output potential is critical in determining its sensitivity or power, yet, there has been very little literature published that investigates how to maximize these two parameters. This chapter further probes the origin of V_{bias} to ultimately assess the technology's potential; how ΔC_T can be increased is left as future work and is discussed in Chapter 5. An alternative theory of how the devices self-bias is tested using a method to measure V_{bias} that was independently developed but closely resembles one presented by Moon [27].

4.1 Self-Biasing Theories

Previous literature, including experimental work documented in Chapter 3, has shown that the variable capacitor model first demonstrated by Moon *et al.* correctly predicts voltage response [18], [21]–[23]. Each interface between the droplet and electrode acts as a charged capacitor with current being driven through an external load resistor. This model, however, has one notable exception: how the capacitors are charged is omitted.

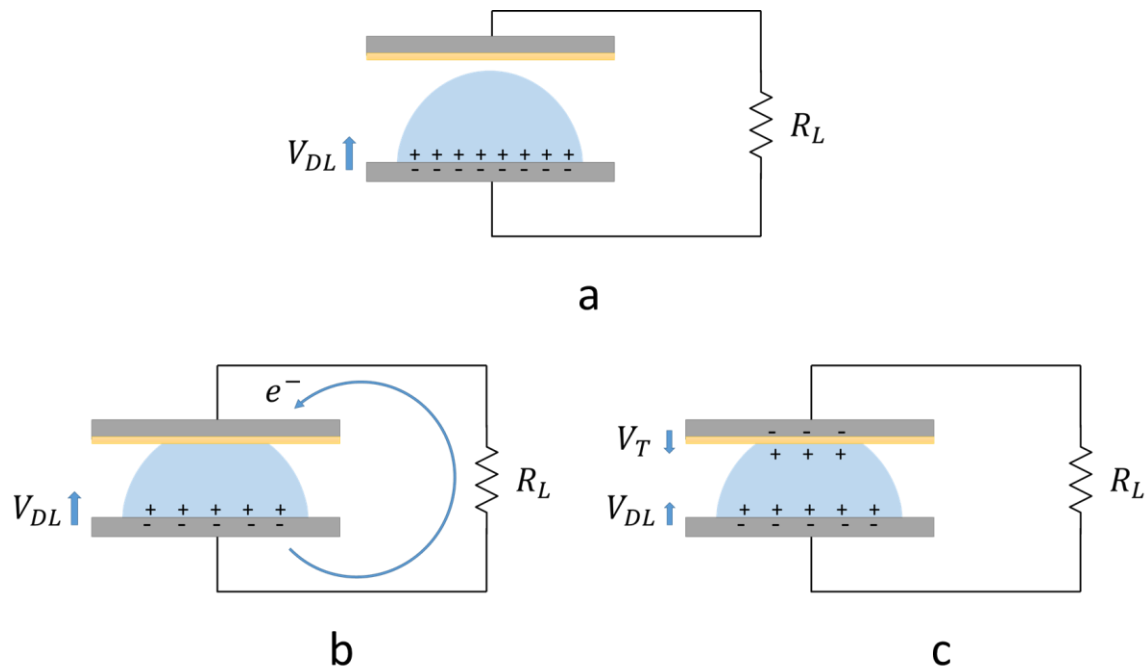


Figure 4-1 – EDL Charging Theory: Initially, when the plates are separated, an EDL forms at that bottom interface as in (a). As the plates are brought together (b), charge moves from the bottom electrode to the top until the potentials across both capacitors are equal and opposite (c).

As discussed in the introduction of this thesis, one theory of how the top interfacial capacitor is charged is via the EDL that is formed at the bottom bare-ITO electrode and the water droplet. If the droplet is only in contact with the bare electrode, an EDL will form at its interface (Figure 4-1a). As the PTFE coated electrode comes into contact with the water, charge will leave the bare-ITO EDL capacitor, C_{EDL} , and charge the capacitor that is formed across the PTFE, C_T , (Figure 4-1b) until the potential across the two are capacitors are equal (Figure 4-1c). This theory has been proposed by Moon and one of its main assumptions, although not explicitly stated, is that the PTFE-AF-water interface does not contribute any charge: it solely acts as a charge sink [27]. This seems to be a completely reasonable assumption as one of PTFE’s properties is that it

is extremely inert. An interesting phenomenon occurs however when PTFE is exposed to aqueous solutions, it tends to acquire a negative charge [28]–[30]. Although the exact mechanism is still a source of controversy [31]–[34], it is believed that hydroxide ions (OH^-) preferentially adsorb onto the surface of the hydrophobic layer [34]–[36], resulting in a surface charge. Recent work has even shown that some of these hydroxide ions remain even when removed from solution [36]. Thus, something that was initially assumed to be completely inert may in fact be the source of the bias.

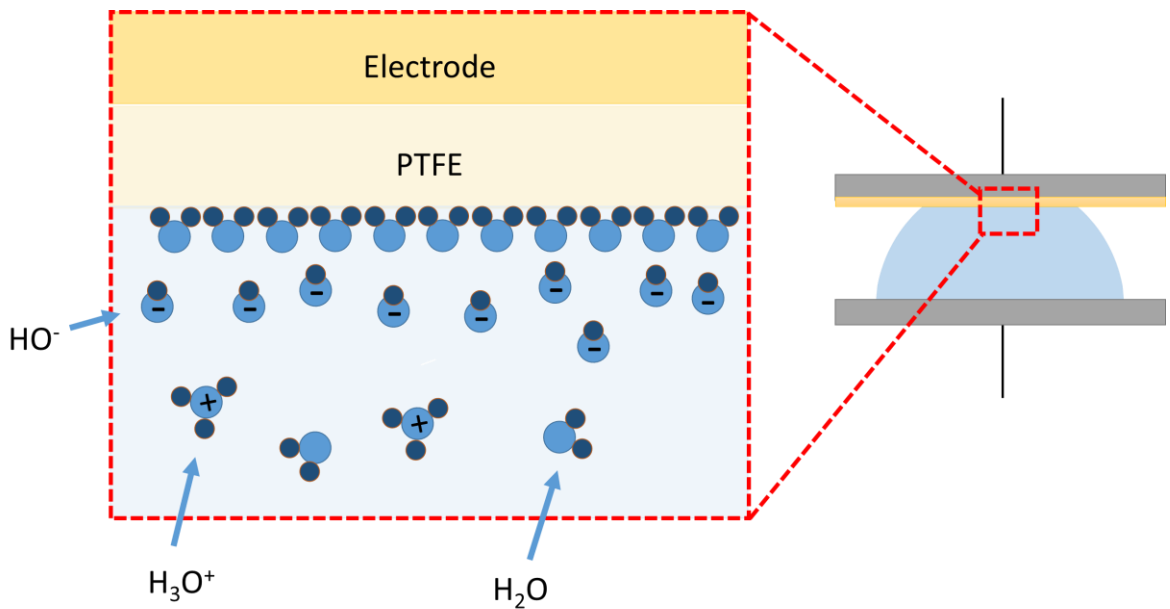


Figure 4-2 - Hydroxide Ion Physical Adsorption – Hydroxide ions are adsorbed on the surface of the Teflon in contact with water, creating a layer of negative charge at the interface.

This Chapter is devoted to determining whether or not hydroxide adsorption plays a role in the devices ability to self-bias.

4.1.1 Determining Charging

There can be a relatively simple way of separating whether charging is from the EDL or if it is a result of hydroxide ions adsorbing to the surface of PTFE; each mechanism should be dependent on the surface areas and capacitances of each respective interface. Specifically, the amount of charge each mechanism contributes will depend on its surface area, and V_{bias} will depend on both C_T and C_{EDL} .

Take the EDL charging mechanism for example. Prior to the top electrode coming into contact with the droplet, as in Figure 4-1a, the amount of charge stored in C_{EDL} should depend mainly on the work function of the electrode and the composition of the electrolyte. If the surface charge density is known, it can be calculated by

$$Q_{EDL} = \sigma_{EDL}A_B, \quad (4.1)$$

where Q_{EDL} is the charge contributed from the EDL, σ_{EDL} is the surface charge density of the interface, and A_B is the amount of area the droplet wets the bottom electrode. As discussed earlier, assuming that the PTFE acts strictly as a charge sink, when the top electrode is brought into contact with the droplet, charge will leave C_{EDL} and enter C_T until the voltages across each capacitor are equal. The voltages across each capacitor will in fact be the biasing potential, V_{bias} .

This will follow

$$\frac{Q_{EDL} - \Delta q}{C_{EDL}} = \frac{\Delta q}{C_T} = V_{bias},$$

where Δq is the charge that moves from C_{EDL} to C_T [27]. V_{bias} can then be calculated by

$$V_{bias} = \frac{Q_{EDL}}{C_T + C_{EDL}}. \quad (4.2)$$

Substituting Equation 4.1 for Q_{EDL} ,

$$V_{bias} = \frac{\sigma_{EDL}A_B}{C_T + C_{EDL}}. \quad (4.3)$$

On the other hand, if charge is supplied by the PTFE-water interface, as

$$\frac{Q_T - \Delta q}{C_T} = \frac{\Delta q}{C_{EDL}} = V_{bias},$$

then

$$V_{bias} = \frac{\sigma_{PTFE}A_T}{C_T + C_{EDL}}, \quad (4.4)$$

where σ_{PTFE} is the surface charge density arising from the PTFE. If C_{EDL} is static and much larger than C_T , which is true for the devices studied in this thesis, vibration induced currents will have a negligible effect on the potential across C_{EDL} , V_{EDL} . As vibrations are applied, V_{EDL} will remain at V_{bias} . This assumption, that $C_{EDL} \gg C_T$, allows for C_{EDL} to be replaced with a DC voltage source with a magnitude of V_{bias} , as shown in Figure 4-3. If the PTFE layer is the source of V_{bias} , it is assumed that charge is not added or removed to the system as A_T is modulated. This will be discussed further in a following section.

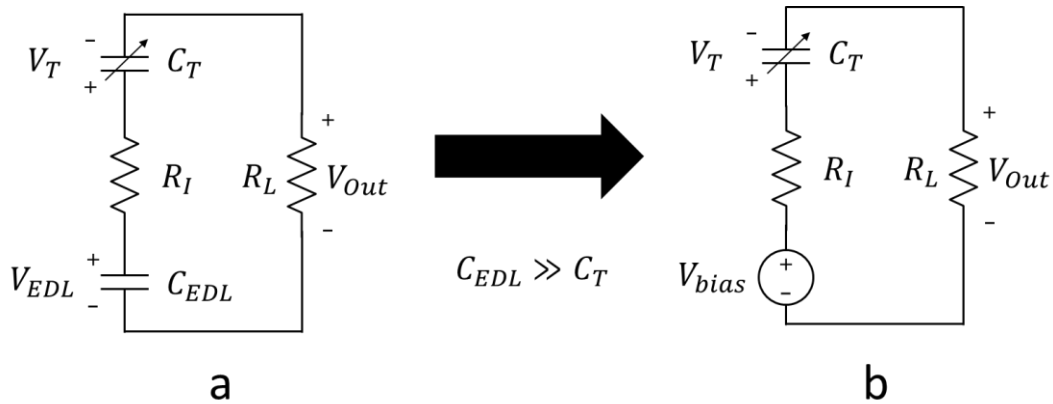


Figure 4-3 – Voltage Source Approximation – Moon’s original model is shown in (a), and assuming that C_{EDL} is much greater than C_T , C_{EDL} can be replaced with a voltage source as the potential across it will stay relatively constant.

Using the transformation of Figure 4-3 the model is simplified such that only the biasing source, the variable capacitor, and the load resistor is considered. If an external voltage source is connected, as in Figure 4-4, when the applied potential, V_{app} , is equal to V_{bias} , V_T will be equal to zero. At this point C_T will not hold any charge and changes in capacitance will not drive any current. Therefore, V_{bias} can be estimated by applying vibrations to one of the electrodes and adjusting V_{app} until there is no AC signal on V_{out} . This method can be used to understand the relationship between V_{bias} and the interfacial surface areas, A_T and A_B . In conjunction with Equations 4.3 and 4.4, the results will ultimately be used to help determine the mechanism that dominates V_{bias} .

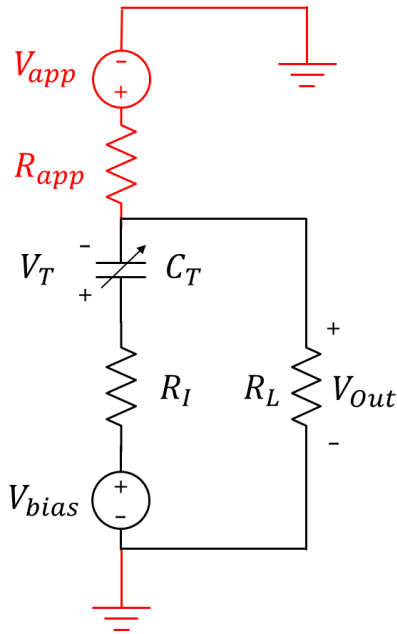


Figure 4-4 – V_{bias} Test Circuit – Applying an external voltage source can oppose the voltage generated by the EDL. At some applied voltage it is assumed that all the charge is driven out of the top capacitor causing vibrations to not elicit any AC response.

4.1.2 Measuring V_{bias}

Figure 4-4 was implemented using a digital potentiometer as discussed in Section 2.3.5. The digital potentiometer created a voltage divider between the Bose DAQ ± 15 V which was applied across the load in series with R_{app} , as shown in Figure 4-4. R_{app} was $10\text{ M}\Omega$, the same resistance as the load resistor, creating another voltage divider that further halved the applied potential. Using Thevenin's theorem, the equivalent resistance of the circuit is $5\text{ M}\Omega$. Due to the presence of the PTFE coating, the capacitance of the top electrode's interface is much smaller than C_{EDL} , therefore, almost the entirety of the potential applied across the load resistor will be dropped across C_T . The purpose of R_{app} is to increase the output impedance of the voltage

source such that the potential isn't clamped at V_{app} . Without this resistor, the measured potential would not deviate from the applied potential.

To ensure that the circuit is not adding any sources of error or artifacts, two frequency responses were taken: one with the biasing circuit enabled but V_{app} set to zero and one with the biasing electronics completely disconnected from the device. The load resistance was set to 5 M Ω for the standard frequency response such that its load resistance was equal to the equivalent resistance of the biasing circuit. Figure 4-5 shows a comparison of the two frequency responses that demonstrates their consistency.

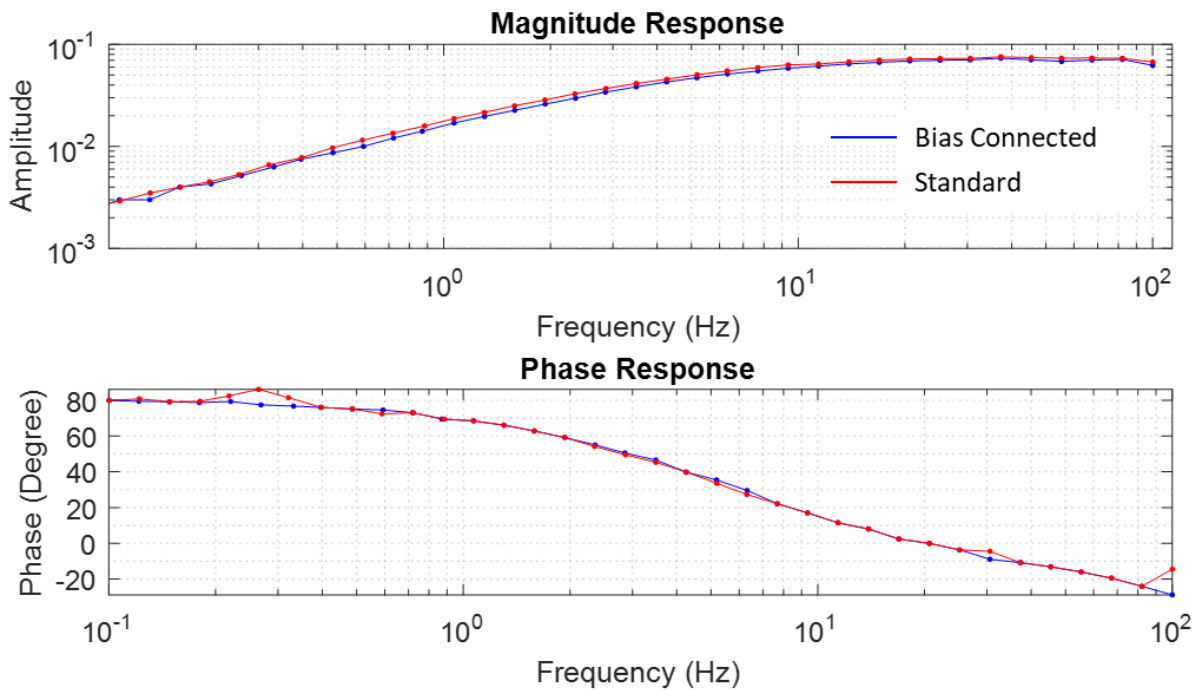


Figure 4-5 – Bias Electronics Validation Log-Log Plots: A comparison of the frequency response between a standard setup to that with the biasing circuit enabled but V_{app} set to zero.

Figure 4-6 shows the results for a standard device as prepared in accordance to Chapter 2 as V_{bias} is swept -1 V to 1.5V. From -1 V to approximately 0.25 V, the peak-to-peak voltage declines linearly with respect to applied potential. At 0.25 V, the signal is completely attenuated. Here, we claim that the top capacitor no longer holds any charge, thus, there is no voltage across the interface and the potential across the load, V_{app} , exactly equals V_{bias} . Changes in capacitance of C_T will not yield a response in voltage. The offset potential at this point can be used as an estimate of V_{bias} . Past 0.25 V, the charge stored by C_T is reversed; there is now a positive charge on the electrode explaining the 180° phase shift. The AC signal magnitude follows a similar trend as before 0.25 V, increasing linearly with applied potential.

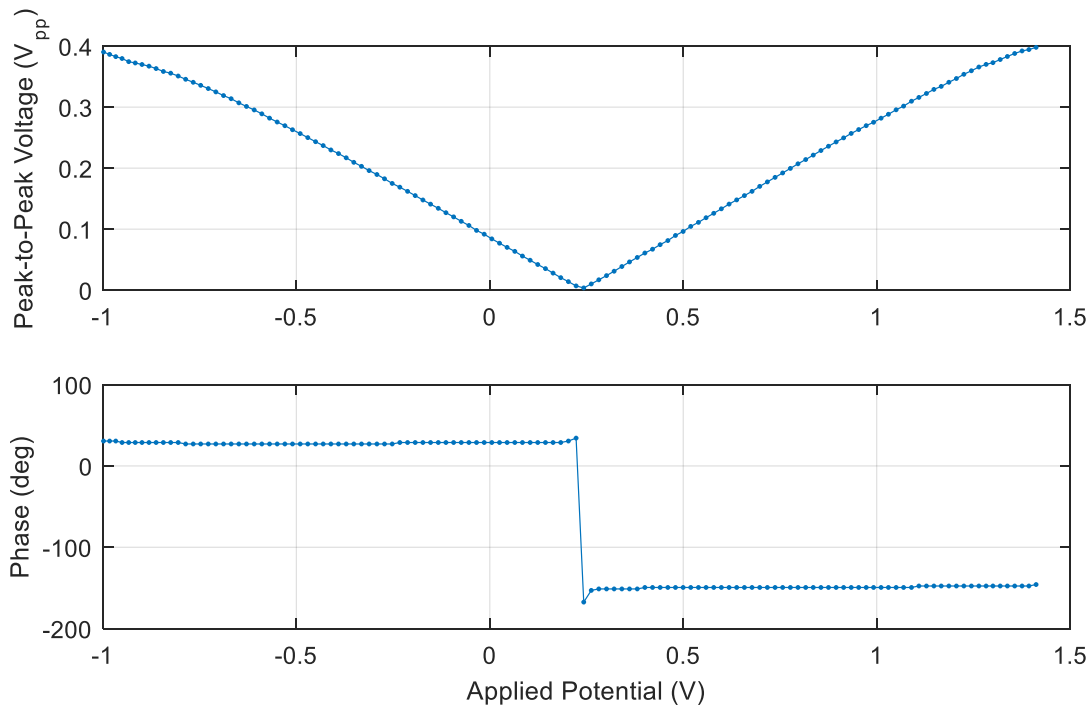


Figure 4-6 – Bias Variation – Applying a single vibration frequency, offset potential is varied from -1 to 1.5V to determine its effect on signal amplitude. At approximately 0.25 V, it is hypothesized that there is no charge in C_T , therefore the AC signal amplitude tends to zero.

Equation 3.12 can be modified to incorporate V_{bias} by replacing V_{EDL} with $(V_{app} - V_{bias})$ to compensate for the applied potential:

$$|V_{out}(j\omega)| = \left| \frac{\omega R_L \Delta C_T (V_{app} - V_{bias})}{\sqrt{1 + [\omega(R_L + R_f)C_T]^2}} \right|. \quad (4.5)$$

Equation 4.5 predicts a linear relationship between signal amplitude and potential applied, agreeing with Figure 4-6. C_T is again assumed to be much smaller than C_{EDL} such that the entire potential drop is across the top electrode's electrolyte-electrode interface.

4.2 Experiments

The main purpose of this chapter is to precisely determine the mechanism behind the device's ability to self-bias. Two different possible charging mechanisms have been discussed; this section presents experiments and their results that may help to separate them.

4.2.1 Varying Surface Area

To determine whether the PTFE charged the interface via a surface charge, vibration frequency and amplitude was kept fixed as offset distance varied. At increased offsets, the average interfacial surface area between the top electrode and droplet will decrease as the bottom interfacial surface area remains constant. If the biasing mechanism is EDL based, it is predicted that changing the offset distance will not strongly affect V_{bias} and will follow a general trend resembling Equation 4.3. The only parameter that will vary will be C_T , and since it is orders of magnitudes smaller than C_{EDL} , it will have a negligible effect. On the other hand, if the biasing

mechanism is due to the PTFE layer, V_{bias} should strongly depend on the top interfacial surface area, a function of plate separation offset, and follow Equation 4.4.

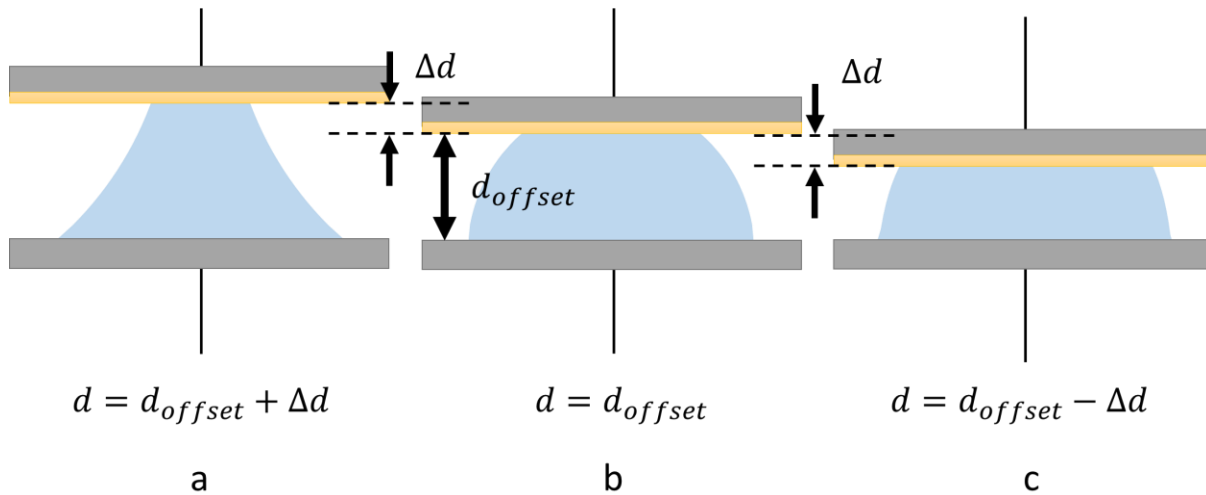


Figure 4-7 - Plate Separation Distance Notation – (b) represents the device’s rest position, at a separation distance of d_{offset} . When the electrodes are at their farthest apart, (a), the distances increases by the amplitude of the vibration, Δd , and when the vibrations pull the plates together, the distance decreases to $d_{offset} - \Delta d$.

To test this, a 0.25 mm 5 Hz vibration was applied with offset distances, d_{offset} , ranging from 1.00 to 1.75 mm separation. Figure 4-8 shows that V_{bias} is not affected by d_{offset} . It also shows that at increased separation distances the slopes decreases. This can be explained by Equation 4.5 as at larger offsets yield a reduced ΔC_T .

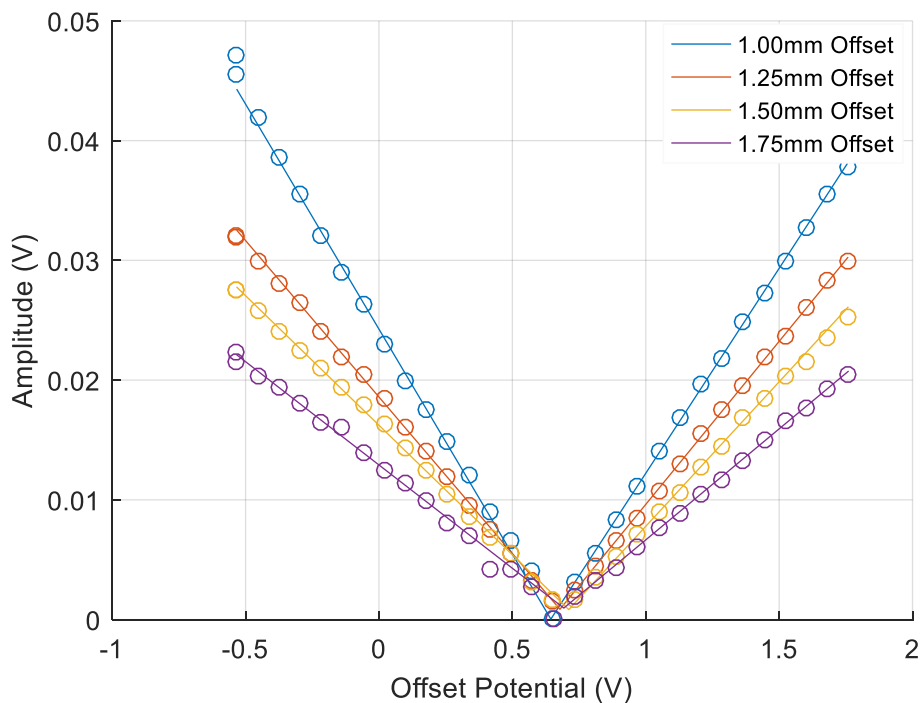


Figure 4-8 – Varying Electrode Separation Distance – Solid lines are a linear fit of data points for varying offsets.

The results shown in Figure 4-8 suggest that the biasing mechanism does not depend on the PTFE-droplet interfacial surface area. This supports the EDL theory that charge is contributed from the electrical double layer and should only depend on its surface area.

4.2.2 Varying C_{EDL}

According to both Equations 4.3 and 4.4, regardless of the charging mechanism, C_{EDL} should strongly affect V_{bias} . The addition of a salt to the droplet will significantly increase C_{EDL} , which should decrease V_{bias} . To confirm or disprove this, NaCl was added to ultrapure water and the V_{bias} measurement test explained earlier was ran. EIS was performed with and without the salt to determine the EDL capacitance by sandwiching a droplet between two uncoated ITO slides.

Using a resistor in series with a capacitor, the resistance and capacitance for DI water was measured to be $24458 \pm 581 \Omega$ and $1081 \pm 32.9 \text{ nF}$, respectively. For a 1.2 M NaCl solution, the resistance was $120.4 \pm 3.5 \Omega$ and capacitance being $1286 \pm 21.7 \text{ nF}$. Assuming that each interface has equal capacitance, each EDL will have a capacitance twice that of the equivalent capacitance measure by EIS. Therefore, the capacitance of a device with DI water will be approximately $2.16 \mu\text{F}$ and for one the salt solution will be $2.56 \mu\text{F}$. After substituting an electrode with a PTFE-coated one and rerunning EIS measurements, a device with salt yielded a capacitance of $31.2 \text{ nF} \pm 0.05\%$ and surprisingly $49.5 \text{ nF} \pm 0.5\%$ for DI water. Therefore, if there is no charge added to the system due to the presence of a salt, Equations 4.3 and 4.4 predict that V_{bias} should decrease to approximately 84% of its initial value with the addition of a salt.

Figure 4-9 shows the results of the experiment and reveals that by varying C_{EDL} , V_{bias} does not change. This indicates that initial relationship discussed in Section 4.1 may not be a true depiction of how the devices charge. Also included in Figure 4-9 is the measurement of V_{bias} for a gold electrode with a DI water droplet. V_{bias} does not change here either which could be explained by the similar work functions of ITO and gold.

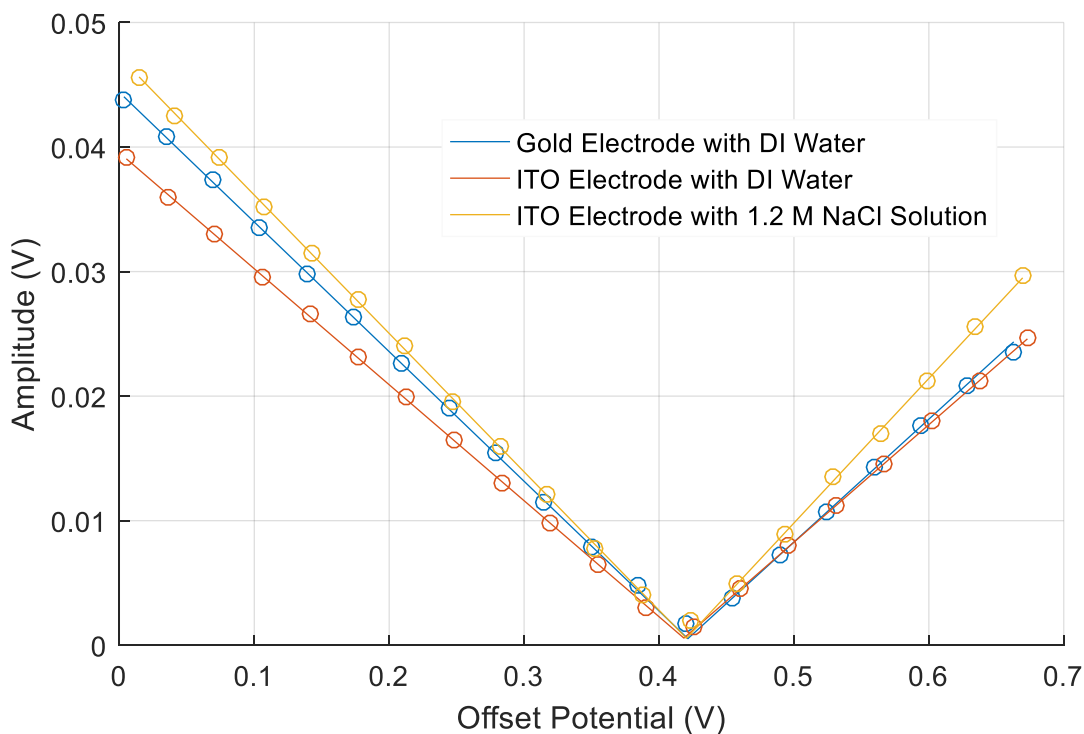


Figure 4-9 - Varying Electrode and Solution Composition V_{bias} Measurements - V_{bias} measurements as electrode and electrolyte composition is changed.

4.2.3 Varying pH

To test whether adsorption of hydroxide ions could possibly explain part of how the interface is being charged, the pH of the droplet was varied and V_{bias} measurements were taken. Earlier experiments indicate that gold responds identically to ITO, allowing gold to replace ITO as the bottom electrode. This is to ensure that acidic or basic droplets do not cause corrosion of the electrode.

Beginning with a pH of 7, V_{bias} measurements were performed for droplets with progressively basic solutions that were prepared by dissolving sodium hydroxide (NaOH) in ultrapure water.

Extra care was made to ensure that the droplets were placed at precisely the same location on the electrode. To test acidic solutions, this location was moved away from where basic measurements were performed and progressively more acidic droplets were measured beginning with a pH of 6. The location of where the droplets were placed was moved between acidic and basic solutions to limit the effects of hysteresis. Acidic solutions were prepared by diluting hydrochloric acid (HCl) to the desired pH.

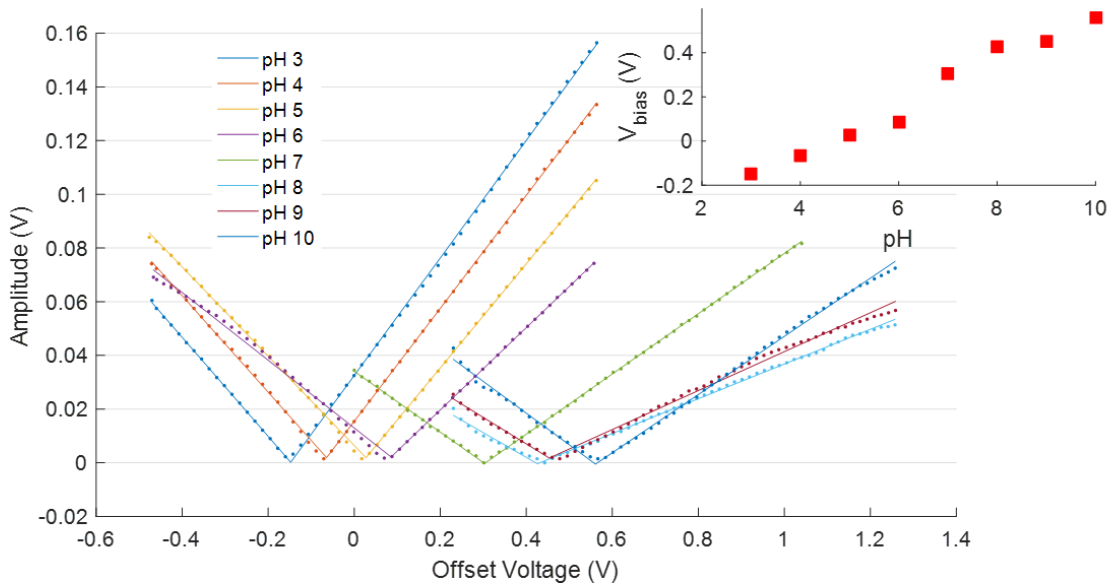


Figure 4-10 - V_{bias} Dependence on pH – V_{bias} measurements for varying pH solutions.

Figure 4-10 illustrates a direct dependence of V_{bias} on pH. Since V_{bias} increases with pH, it indicates hydroxide ions are preferentially adsorbing to one of the electrodes. These results however, could be explained by the EDL theory as well as charging via hydroxide adsorption. If OH^- adsorbs to the bare electrode, this could increase the potential across the electrical double layer, which in this case is V_{bias} . The amount of hydroxide ions that would adsorb would depend

on the amount in solution, and since pH is a direct measurement of OH^- concentration, an increase in pH would result in a larger V_{bias} , as shown in Figure 4-10. It could then be argued that this dependence supports the EDL theory.

On the other hand, since OH^- is known to adsorb to the surface of PTFE, this could provide additional support that it is playing a role in charging the mechanism. The change in potential with pH is very similar to the trend observed in the surface charge of Teflon/water interfaces, as measured by Zimmermann *et al.* [37], making this hypothesis seem most likely. The final test that was performed in this study involves a step response to determine the flow of current upon initial contact.

4.2.4 Step Response

Much can be revealed from the direction and magnitude of the current that flows upon initial contact between the droplet and electrode. Figure 4-11 shows a step response for a standard setup with the top, PTFE-coated electrode initially apart from the droplet. This current is predicted by the EDL theory.

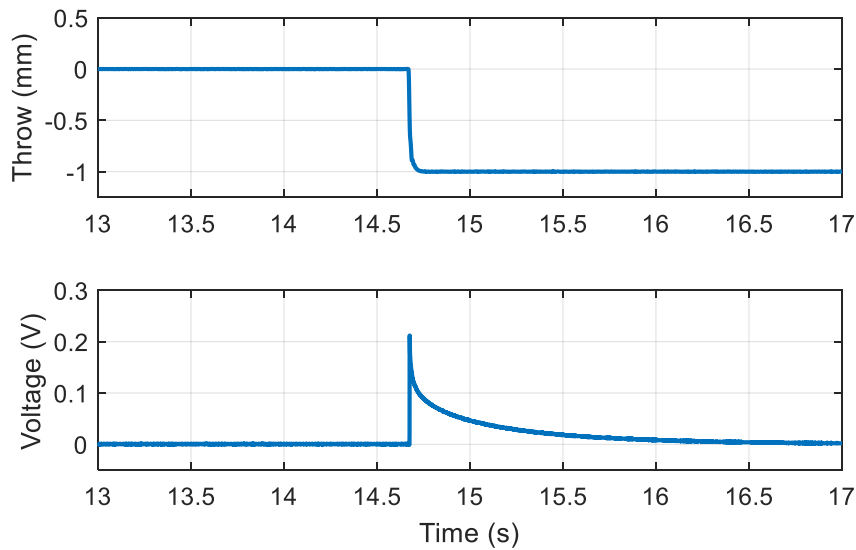


Figure 4-11 - Step Response: Standard Configuration – The top electrode is coated with PTFE and is initially not in contact with the droplet.

The positions of the electrodes were then switched, the PTFE coated electrode on the bottom and the bare, gold electrode placed on top. In this case, the EDL theory predicts a voltage spike opposite that of Figure 4-11, yet Figure 4-12 shows one with identical sign. This indicates that charging may not be coming from the interface at all, that the droplet may already have a positive charge on its surface prior to contact with either surface. One possible explanation can be from charge that is induced by conventional pipetting [38]. To test this scenario, a glass pipette was used in replace of the polypropylene pipette tip but yielded identical results. This ruled out charging via pipette. Following the step response using the reversed electrode orientation, the electrodes were replaced to their original orientation and another step response was conducted. This again yielded unexpected results.

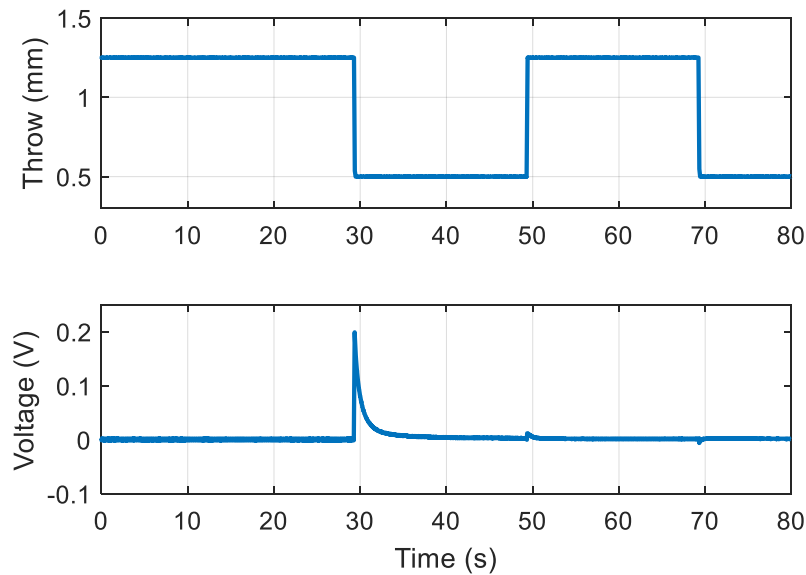


Figure 4-12 - Step Response: Reverse Electrode Setup – The top electrode is uncoated while the bottom has a thin coating of PTFE.

Figure 4-13 shows three step responses using a standard setup immediately after the step response displayed in Figure 4-12 was taken. The first step response, the left plot in Figure 4-13, responds opposite of what the EDL theory predicts. After subsequent steps however, the response returns to normal. This phenomenon, as well as results shown in Figure 4-12, can be explained by hydroxide ion adsorption at the top electrode.

In Figure 4-12, the droplet begins wetted to the PTFE without any contact to the bare electrode. Adsorption of hydroxide ions creates an electrical double layer beginning at the surface of the PTFE and extends into solution. As soon as the droplet contacts the bare electrode, electrostatic forces of the adsorbed hydroxide ions push electrons out of the PTFE electrode. This also

discharges the EDL at the PTFE interface which elicits the positive voltage across the load resistor and may cause hydroxide ions to desorb from the surface.

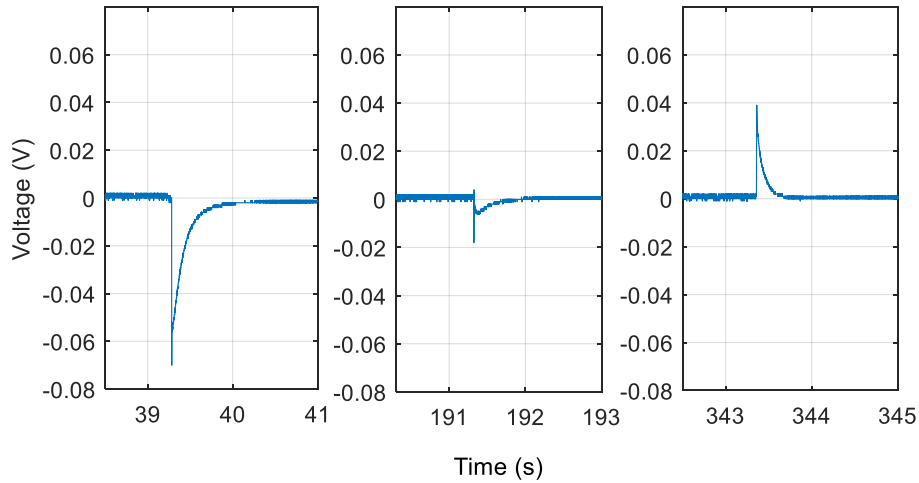


Figure 4-13 - Step Response Standard Setup after Reversing Electrode – Each of the three plots above are step responses using a standard orientation. Initially the top PTFE-coated electrode is not touching the droplet in each of the plots.

Once the electrodes have been replaced to their original orientation, as soon as the droplet meets PTFE the adsorption of hydroxide ions will dominate current and yield a response as shown in Figure 4-13. For each subsequent step, the current decreases. This seems to indicate that the adsorption of hydroxide ions may remain as the PTFE is removed from the droplet, as argued in [36].

4.3 Discussion

Many of the results presented in this work can be explained by the EDL theory. Varying plate separation offset yields very little change in V_{bias} , as would be expected if the non-varying bottom electrode was the source of charge. It also correctly predicts the current for step responses given that the top electrode has already been in contact with the droplet. However, there are key findings that question the EDL theory. First of all, the addition of a salt to the droplet showed little to no effects. If the electrical double layer theory postulates that electrolyte concentration should drastically affect V_{bias} . Even in one of Moon's papers, they simulate results showing that the addition of an electrolyte causes a decrease in V_{bias} , yet this was not observed experimentally [27]. Secondly, V_{bias} was shown to be strongly correlated to pH. Although this can be explained by the EDL theory as hydroxide ions have been observed to adsorb to the surface of bare electrodes [39], [40], there are far more examples of OH^- adsorbing to the surface of hydrophobic materials. And finally, the step responses revealed results that cannot be easily explained by EDL theory. Other observations not documented in this thesis also seem to support this. PTFE-coated electrodes tended to gain charge for no apparent reason. Figures 4-6, 4-8, and 4-9 illustrates examples of this. V_{bias} measurements vary from approximately 0.25V in Figure 4-6 up to 0.6V in Figure 4-8. They should all be equal in magnitude. The PTFE-coated electrodes tended to increase in V_{bias} measurements over time, thus, experiments needed to be performed in a timely manner. Even between PTFE samples there was variation in V_{bias} measurements and it was found that samples that were not baked at 330 °C yielded higher base V_{bias} results. These observation also seem to support the hydroxide adsorption theory. Yet, the hydroxide adsorption theory isn't perfect either. Even though most indications point towards OH^- adsorbing to the surface of the PTFE being the charging mechanism, it is not trivial to explain

the currents that are generated. Specifically, the current flows in the opposite direction as expected. In the following section a theory as to how the adsorption of hydroxide can cause currents that reflect real world observations is presented.

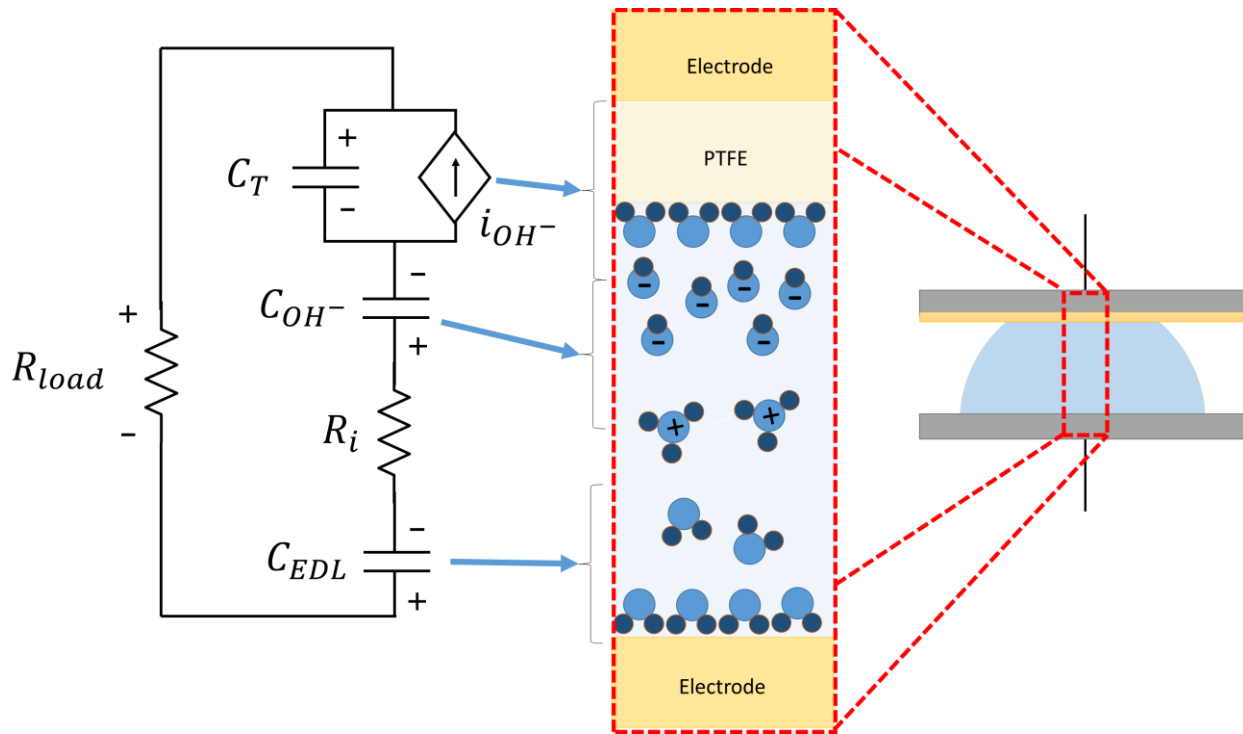


Figure 4-14 – PTFE-Water Interface: Hydroxide ions adsorb to the surface of the PTFE acting to charge the interfacial capacitance

4.3.1 Hydroxide Adsorption Induced Charging

The preferential adsorption of hydroxide ions can induce a positive charge on the top capacitor. This will also cause the formation of an electrical double layer that extends from the surface of the PTFE into solution, with a capacitance of C_{OH^-} . This is shown in Figure 4-14. As the plates are brought together, the top PTFE-water interface will grow, causing C_T to decrease as discussed previously. This can also cause an increase in physically adsorbed hydroxide ions,

which acts to add charge to the system. To compensate for this, positive ions and water molecules will rearrange themselves to screen the additional charge. This will drive a net positive current flowing from the bottom electrode to the top. When the electrodes are separated, the opposite will happen.

As an equivalent electrical circuit, a surface area dependent current source is added in parallel across C_T to simulate the addition of negative charges via hydroxide adsorption. Another key difference from Moon's original model is that the capacitor symbolizing the EDL formed at the PTFE interface is present.

As a quick check to ensure the theory predicts a real response, it can be compared to the linear approximation models developed in Chapter 3. Assuming C_{OH^-} and C_{EDL} and much greater than C_T that they approximate to short circuits, the model closely resembles the current source approximation of circuit of Figure 3-7.

4.4 Summary

This Chapter challenged the current idea of how these devices self-bias. Experiments were performed to help identify what the charging mechanism and from all that was gathered, it can be argued that hydroxide ion adsorption is how these devices self-bias. That being said, hydroxide adsorption is not the only mechanism of charging. Electrochemical reactions at the surface of the electrode could also impose a charge. The following Chapter ties everything together and attempts to give the technology a fair assessment as well as a guide for possible future work.

Chapter 5: Conclusion and Future Work

This thesis studied an electrostatic transduction mechanism that varies capacitance by modulating the interfacial surface area between a water droplet and PTFE-AF. The main goal of this thesis was to develop a strong enough understanding of the mechanism in hopes to provide an honest assessment as to whether or not the technology should be further studied. This Chapter begins with a short summary of the work conducted and the main experimental findings it revealed. The following section provides a road map for future work to develop a better understanding of the mechanism. Using what is currently known, some potential applications of the technology are presented. Finally, an assessment of the transduction mechanism as both a sensor and generator is provided.

5.1 Research Conducted

The first example of a device was presented by Moon *et al.* in 2013, published in Nature Communications [18]. They sandwiched a deionized water droplet between two electrodes with one coated by Teflon® AF. Vibrating one electrode with respect to the other resulted in a relatively impressive voltage response. They claimed that this was a result of “mechanically modulating electrical double layers,” and in a paper a couple years later they claimed that the biasing mechanism arises from the electrical double layer [27]. They provided a model that accurately predicts the voltage response as it relates to interfacial surface area between the PTFE and droplet. This model, however, was a non-linear differential equation. This made it very difficult to intuitively understand how to improve performance. They also demonstrated a very limited bandwidth of up to 30 Hz. To investigate optimization techniques and gain a better understanding of how this may work, a similar setup to Moon’s was constructed including the

design of 3D printed fixtures, the preparation of high quality thin PTFE-AF films, and the design of signal conditioning electronics.

Investigation of the frequency response revealed a simple method of improving bandwidth by decreasing the separation distance between electrodes. Bandwidth was improved to 100 Hz, surpassing literatures best of 80 Hz using a hydrogel [22]. Also revealed was the first-order high pass response in the frequency domain, something that had not been demonstrated previously. This led to the development of a linear-approximation model that was used to analytically predict the point of maximum power transfer. This prediction was proven experimentally to be accurate and could be extremely valuable for load tuning if the technology is used for generation. In doing so, average powers as high as 3.4 nW for 35 Hz were achieved giving a specific power density of 85 nW mL⁻¹. This was more than an order of magnitude less power than the 1.5 μW that was claimed by Moon *et al.* Arguably the greatest contribution however was that the model provides is that it clearly shows how to improve performance, chiefly by increasing the potential across the top interfacial capacitor and the change in its capacitance. Affecting the variation in capacitance can be done straightforward enough; examples include increasing plate size, adding more droplets, or even using some microfluidic techniques. However, to be able to generate substantial amounts of power, self-biasing needs to be increased. As an important step to increasing self-biasing, or at least in determining the limits, is to understand the physical origin of this effect.

To probe into how and why a potential is generated across the top capacitor, a circuit was designed that can apply a bias across the device. This technique provided an ability to measure

the voltage of the mechanism as electrolyte composition and device configuration was varied. This ultimately revealed a strong dependence of self-generated bias on solution pH. These results, along with the lack of a response after adding a salt to the ultrapure water, suggest that hydroxide adsorption to the PTFE-AF could be the source of bias.

5.2 Further Work

Although there is strong support that hydroxide adsorption is the cause of the device's ability to self-bias, it is not fully clear how the presence of negative ions at the PTFE surface drives a current, specifically, why the current seems to flow in the opposite direction as expected. Once a greater understanding of how and why hydroxide ions adsorb, it may reveal what the mechanism is that is driving the current. The technique for measuring V_{bias} presented in Chapter 4 may even be used as a tool to further understand what is occurring at the surface of hydrophobic materials.

To investigate further whether or not the electrical double layer is playing a role in self-biasing, redox couples of varying redox potentials could be added to solution to affect V_{bias} . Even if it is proved that the device is biased solely by the adsorption of hydroxide ions, adding a redox couple could significantly improve power output as V_{bias} would ultimately tend to the redox potential of the couple. Further investigation of this is strongly suggested.

In light of the results obtained and presented in the thesis, if the EDL is in fact the biasing mechanism, decreasing the hydrophobic layer thickness should greatly improve performance. Self-assembled monolayers could be used to create an atomically thin monolayer as well.

On the other hand, if the generated bias is due to hydroxide adsorption, increasing surface area of the PTFE-AF layer could potentially generate high V_{bias} 's. One way of doing this would be to increase the porosity of the PTFE-AF by plasma ablation [41], [42], or using an electrospun PTFE mat [43]. Whether or not these techniques increase performance may help support or refute this theory.

As a sensor, an important characteristic is its bandwidth. Since the current setup only allows testing of up to 100 Hz, a new experimental setup would need to be designed to test past the 100 Hz range. This can be performed via a shaker and appropriate power electronics. An additional improvement to the experimental setup could include a high frame-rate camera positioned directly above the top electrode as to measure the surface area directly. This may be required for the testing of higher frequencies and would alleviate a potential source of error.

5.3 Outlook and Applications

Any transduction mechanism can be used either for sensing or generation. In this section, we look at how this technology would perform as a sensor its current state and what would be required for this transduction mechanism to compete with other vibrational energy harvesters.

5.3.1 Sensing

The transduction mechanism in its current state *can* be used in a sensor. The main issue with a device based on this effect is evaporation, however, if a proper encapsulant was found that allows for deformation without letting water escape, a device could be made relatively cheap. Less volatile ionic liquids can also be used.

Bode plots of Chapter 3 have also shown that it has a bandwidth of up to at least 100 Hz. Proper design could allow for a bandwidth ranging into the kilohertz range which may allow it to be an acoustic sensor.

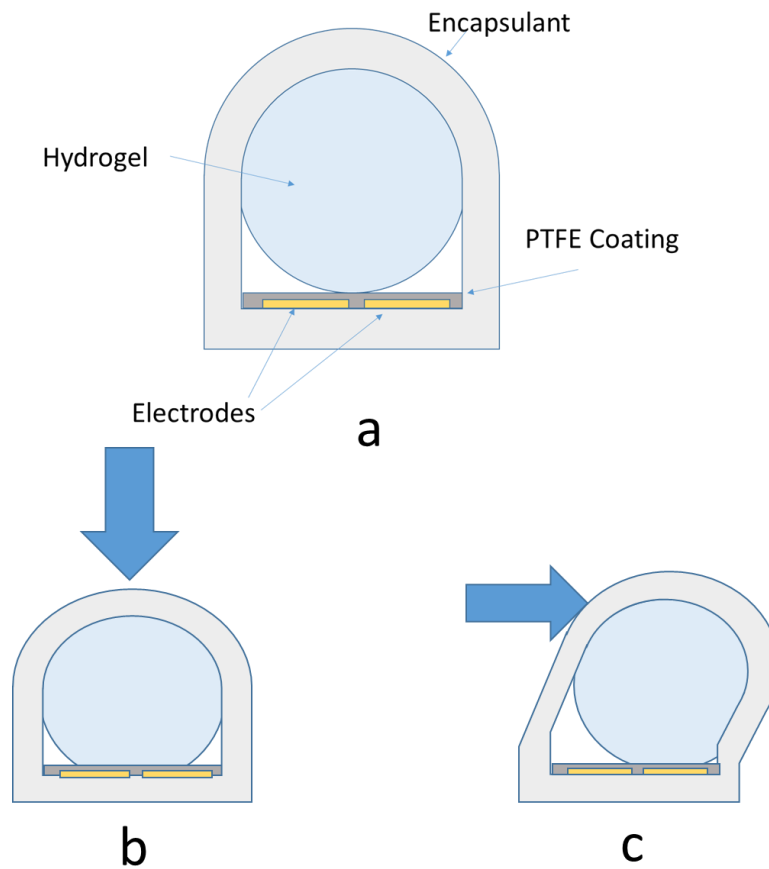


Figure 5-1 - Artificial Fingerprint Embodiment – (a) General design of the sensor. (b) and (c) illustrate how interfacial surface area changes for normal and shear forces, respectively.

One attractive feature of this transduction mechanism is that the sensor would not draw any power as it is generative. Capacitance based sensors on the other hand require an applied

sinusoidal signal to be measured. This adds an additional power draw and may limit its uses in low power applications.

One of the benefits of using a standard capacitance based transducer is that, if an electrolyte is used, it can be incredibly sensitive, owing to the huge capacitance per given surface area of an EDL. If the studied transduction mechanism is coupled with standard capacitance measurements, a design for an artificial fingertip-like shear sensor has been imagined. Figure 5-1 shows a possible embodiment for an artificial fingertip using the transduction mechanism to sense shear displacement. The proposed fingertip contains a spherical hydrogel within a dome-shaped encapsulant, possibly PDMS. Electrodes are at the base of the fingertip with a thin PTFE coating that is in contact with the hydrogel. As pressure is applied, as shown in Figure 5-1(b), the interfacial surface area between the hydrogel and PTFE will grow, yielding an increase in capacitance which can be measured. For a shear force on the other hand, Figure 5-1(c), the interfacial surface area of one electrode will increase while the other will get smaller. This will cause a decrease in surface area, which again, can be measured capacitively. This can provide an extremely sensitive reading, but in order to separate a shear force versus a decrease normal force, as both would yield a decrease in capacitance, the offset potential arising from the mechanism studied here could be measured. This potential would indicate whether or not a shear force is being applied and can even provide direction.

5.3.2 Generation

To be used as a vibration energy harvester, the transduction mechanism not only needs to compete with conventional electrostatic energy harvesters but alternative technologies as well.

The two other most common transduction mechanisms used for vibration energy harvesting, excluding electrostatic transduction, are through the use of piezoelectric materials and electromagnetic generators. In Roundy *et al.*'s textbook, "Energy Scavenging for Wireless Sensor Networks," a comparison of the three main transduction mechanisms is made. They calculate that the theoretical maximum energy density of piezoelectric and electromagnetic, 335 mJ cm⁻³ and 400 mJ cm⁻³, respectively. It should be noted however that at the time of the books publishing, the practical maxima were far less, at 17.7 mJ cm⁻³ for piezoelectrics and 4 mJ cm⁻³ for electromagnetics. For electrostatic transduction, they calculate a theoretical maximum at 44 mJ cm⁻³, which is close to an order of magnitude less than the others [12, pp. 47–50]. However, this was calculated for *conventional* electrostatic transduction. It can be argued that by utilizing the electrical double layer the improvement can be of the same order as when the EDL was applied to capacitors, which led to the development of supercapacitors. By adding an external potential source and incorporating a high dielectric-strength polymer to coat one of the electrodes, it can be possible for these devices be able to generate a significant amount of power.

To determine what the upper limit energy density this device may be able to produce, similar calculations can be performed as Roundy *et al.* [12]. Equation 1.3 of Chapter 1,

$$E = \frac{1}{2} V_{bias}^2 (C_{max} - C_{min}),$$

which calculates the amount of energy a device is able to extract per cycle, can be used to determine a theoretical maximum energy density. If it is assumed that an electrolyte can be removed from contact with one electrode, C_{min} can be set to zero. This allows it to reduce to the equation that governs the amount of energy that can be stored in a capacitor, or

$$E = \frac{1}{2} V_{bias}^2 C_{max}.$$

If an ionic liquid is used, potentials as high as 3 V can be applied without breakdown. If the device is made to self-bias, a redox couple could be added. A thin dielectric coating would then be required on the interfacial surface area-varying electrode to inhibit chemical reaction. If the coating has a high dielectric strength, such as a 210 V μm^{-1} barium titanate polymer [44], external circuitry could apply a potential to increase power output. The capacitance can then be estimated via the parallel plate equation as performed earlier in this thesis. After substituting the parallel plate equation for C_{max} , the above equation is

$$E = \frac{1}{2} V_{bias}^2 \left(\frac{\epsilon A}{d} \right),$$

and becomes

$$E = \frac{1}{2} (\beta d)^2 \left(\frac{\epsilon A}{d} \right) = \frac{1}{2} \beta^2 d A \epsilon,$$

where β is the insulators dielectric strength. For a 1 μm dielectric, the applied potential would be 210 V and yield a surface area energy density of 7.2 J m^{-2} . The strength of this transduction mechanism however is that a large amount of surface area can be fit into a small volume. To match the theoretical maximum of a piezoelectric energy harvester, 55 cm^2 of internal surface area per centimeter cubed would be required. As a point of reference, it has been shown that activated carbon can have surface areas as high as 1682 m^2 per centimeter cubed [45]. This proves that if a material with high surface area is able to be wetted and dewetted quickly, very high powers can be achieved.

Figure 5-2 shows an example of a potential electrostatic generator that uses the transduction method studied in this thesis, termed a super transducer. A metal housing holds either an ionic liquid or aqueous solution depending on whether it is sealed or not. The housing acts as one electrode while the other is a metal plate with holes that allows ionic liquid to penetrate. As the mass moves, it forces electrolyte into and out of the channels acting to vary the capacitance. An external voltage source would be necessary to charge the electric double layers. If the transducer is made to self-bias, a redox couple could be added to the solution and a coating to the channels to inhibit chemical reaction.

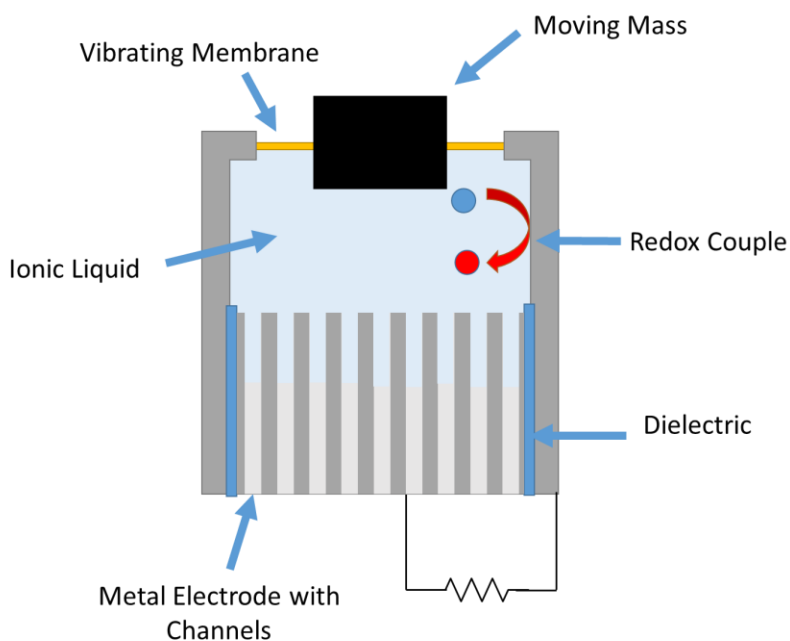


Figure 5-2 – “Super” Transducer – Applying a biasing source to high surface area electrodes may enable this technology for vibrational energy harvesting.

There are some significant challenges however before this can be realized. First of all, this is assumed that surfaces perfectly wet and dewet without being affected by applied potential. Initial

tests using carbon paper as an electrode shows that this can be a major challenge. Recent work has developed a one-step procedure that uses a nanosecond laser to create near superhydrophobic metal surfaces [46] that may be ideal for this application. This may completely negate the need for the hydrophobic surface layer altogether, which could substantially increase power.

5.4 Concluding Remarks

This thesis has studied a relatively recent electrostatic transduction mechanism that has the potential to be used as both a sensor and generator. It can also be used as a tool to investigate surface phenomena and may lead to the better understanding of hydrophobic surfaces. It has shown methods of how to increase a droplet based transducer's bandwidth and how to tune the load for increased power transfer. Investigation into the biasing mechanism can make a strong case that its origin is from hydroxide adsorption rather than via the formation of an EDL as thought previously. This effect may be useful as a sensor but shows limited practicality for generation. With the addition of an external power source, however, it has been argued that it may be able to surpass all other vibration transduction mechanisms. Adding a redox couple may be able to improve the self-biasing as well. Further study is strongly recommended.

Bibliography

- [1] J. A. Paradiso and T. Starner, "Energy scavenging for mobile and wireless electronics," *IEEE Pervasive Comput.*, vol. 4, no. 1, pp. 18–27, 2005.
- [2] M. A. Halim, H. Cho, and J. Y. Park, "Design and experiment of a human-limb driven, frequency up-converted electromagnetic energy harvester," *Energy Convers. Manag.*, vol. 106, no. October, pp. 393–404, 2015.
- [3] P. D. Mitcheson, E. M. Yeatman, G. K. Rao, A. S. Holmes, and T. C. Green, "Energy Harvesting From Human and Machine Motion for Wireless Electronic Devices," *Proc. IEEE*, vol. 96, no. 9, pp. 1457–1486, 2008.
- [4] G. Görge, M. Kirstein, and R. Erbel, "Microgenerators for energy autarkic pacemakers and defibrillators: fact or fiction?," *Herz*, vol. 26, no. 1, pp. 64–68, 2001.
- [5] B. Lo and G.-Z. Yang, "Key technical challenges and current implementations of body sensor networks," in *Proc. 2nd International Workshop on Body Sensor Networks (BSN 2005)*, 2005.
- [6] K. S. Low, W. Nu, N. Win, M. J. Er, and W. N. N. Win, "Wireless Sensor Networks for Industrial Environments," in *International Conference on Computational Intelligence for Modelling Control and Automation and International Conference on Intelligent Agents Web Technologies and Internet Commerce CIMCAIAWTIC06*, 2005, vol. 2, pp. 271–276.
- [7] S. Boisseau, "Energy harvesting , wireless sensor networks & opportunities for industrial applications," *EE Times*, 2012.
- [8] E. O. Torres and G. A. Rincón-Mora, "Energy budget and high-gain strategies for voltage-constrained electrostatic harvesters," *Proc. - IEEE Int. Symp. Circuits Syst.*, pp. 1101–1104, 2009.
- [9] E. O. Torres and G. A. Rincon-Mora, "Electrostatic energy harvester and Li-Ion charger circuit for micro-scale applications," *Midwest Symp. Circuits Syst.*, vol. 1, pp. 65–69, 2006.
- [10] P. A. Tipler, *College Physics*. New York, 1987.
- [11] S. P. Beeby, M. J. Tudor, and N. M. White, "Energy harvesting vibration sources for microsystems applications," *Meas. Sci. Technol.*, vol. 17, no. 12, p. R175, 2006.
- [12] S. J. Roundy, P. K. Wright, and J. M. Rabaey, *Energy Scavenging for Wireless Sensor Networks*, vol. 49. New York: Springer-Verlag, 2004.

- [13] K. A. Cook-Chennault, N. Thambi, and A. M. Sastry, “Powering MEMS portable devices—a review of non-regenerative and regenerative power supply systems with special emphasis on piezoelectric energy harvesting systems,” *Smart Mater. Struct.*, vol. 17, no. 4, 2008.
- [14] S. Kuyucak and T. Bastug, “Physics of Ion Channels,” *J. Biol. Phys.*, vol. 29, no. 4, pp. 429–446, 2003.
- [15] A. Bard, L. Faulkner, J. Leddy, and C. Zoski, *Electrochemical methods: fundamentals and applications*. 1980.
- [16] M. Z. Bazant, K. Thornton, and A. Ajdari, “Diffuse-charge dynamics in electrochemical systems,” *Phys. Rev. E - Stat. Nonlinear, Soft Matter Phys.*, vol. 70, pp. 1–24, 2004.
- [17] J. O. Bockris, A. K. N. Reddy, and M. E. Gamboa-Aldeco, *Modern Electrochemistry 2A: Fundamentals of Electrode Processes*. Springer US, 2000.
- [18] J. K. Moon, J. Jeong, D. Lee, and H. K. Pak, “Electrical power generation by mechanically modulating electrical double layers,” *Nat. Commun.*, vol. 4, p. 1487, 2013.
- [19] T. Krupenkin and J. A. Taylor, “Reverse electrowetting as a new approach to high-power energy harvesting,” *Nat. Commun.*, vol. 2, no. 448, pp. 1–7, 2011.
- [20] F. Garbassi, M. Morra, E. Occhiello, and F. Garbassi, *Polymer surfaces: from physics to technology*. 1998.
- [21] X. Wu, G. Li, and D. W. Lee, “A hydrogel-based energy harvester with broad bandwidth driven by ambient vibrations,” in *International Conference on Solid-State Sensors, Actuators and Microsystems (TRANSDUCERS)*, 2015, pp. 938–941.
- [22] X. Wu, G. Li, and D.-W. Lee, “A novel energy conversion method based on hydrogel material for self-powered sensor system applications,” *Appl. Energy*, vol. 173, pp. 103–110, 2016.
- [23] W. Kong, P. Cao, X. He, L. Yu, X. Ma, Y. He, L. Lu, X. Zhang, and Y. Deng, “Ionic liquid based vibrational energy harvester by periodically squeezing the liquid bridge,” *RSC Adv.*, vol. 4, no. 37, pp. 19356–19361, 2014.
- [24] Z. H. Lin, G. Cheng, S. Lee, K. C. Pradel, and Z. L. Wang, “Harvesting water drop energy by a sequential contact-electrification and electrostatic-induction process,” *Adv. Mater.*, vol. 26, no. 27, pp. 4690–4696, 2014.
- [25] K. Liu, Y. Zhou, F. Yuan, X. Mo, P. Yang, Q. Chen, J. Li, T. Ding, and J. Zhou, “Self-Powered Multimodal Temperature and Force Sensor Based-On a Liquid Droplet,” *Angew. Chemie*, no. d, pp. 1–6, 2016.

- [26] Y. Gao, J. Song, S. Li, C. Elowsky, Y. Zhou, S. Ducharme, Y. M. Chen, Q. Zhou, and L. Tan, "Hydrogel microphones for stealthy underwater listening," *Nat. Commun.*, vol. 7, p. 12316, 2016.
- [27] J. K. Moon, M. W. Song, and H. K. Pak, "Investigation of surface charge density on solid–liquid interfaces by modulating the electrical double layer," *J. Phys. Condens. Matter*, vol. 27, no. 19, 2015.
- [28] K. Yatsuzuka, Y. Higashiyama, and K. Asano, "Electrification of polymer surface caused by sliding ultrapure water," *IEEE Trans. Ind. Appl.*, vol. 32, no. 4, pp. 825–831, 1996.
- [29] R. Zimmermann, S. Dukhin, and C. Werner, "Electrokinetic measurements reveal interracial charge at polymer films caused by simple electrolyte ions," *J. Phys. Chem. B*, vol. 105, no. 36, pp. 8544–8549, 2001.
- [30] C. Dicket and G. Hahner, "pH-dependent force spectroscopy of tri(ethylene glycol)- and methyl-terminated self-assembled monolayers adsorbed on gold," *J. Am. Chem. Soc.*, vol. 124, no. 42, pp. 12619–12625, 2002.
- [31] R. Vácha, V. Buch, A. Milet, J. P. Devlin, and P. Jungwirth, "Autoionization at the Surface of Neat Water: Is the Top Layer pH Neutral, Basic, or Acidic?," *Phys. Chem. Chem. Phys.*, vol. 9, pp. 4736–4747, 2007.
- [32] J. K. Beattie, "Comment on autoionization at the surface of neat water: is the top layer pH neutral, basic, or acidic? by R. Vácha, V. Buch, A. Milet, J. P. Devlin and P. Jungwirth, *Phys. Chem. Chem. Phys.*, 2007, 9, 4736," *Phys. Chem. Chem. Phys.*, vol. 10, no. 2, pp. 330–331, 2007.
- [33] R. Vácha, V. Buch, A. Milet, J. P. Devlin, and P. Jungwirth, "Response to Comment on autoionization at the surface of neat water: is the top layer pH neutral, basic, or acidic? by R. Vácha, V. Buch, A. Milet, J. P. Devlin and P. Jungwirth, *Phys. Chem. Chem. Phys.*, 2007, 9, 4736," *Phys. Chem. Chem. Phys.*, vol. 10, no. 2, pp. 332–333, 2007.
- [34] J. K. Beattie, A. M. Djerdjev, and G. G. Warr, "The surface of neat water is basic," *Faraday Discuss.*, vol. 141, pp. 31–39, 2009.
- [35] J. K. Beattie, "The intrinsic charge on hydrophobic microfluidic substrates.," *Lab Chip*, vol. 6, no. 11, pp. 1409–1411, 2006.
- [36] A. Banpurkar, Y. B. Sawane, S. M. Wadhai, C. Murade, I. Siretanu, D. van den Ende, and F. Mugele, "Spontaneous electrification of fluoropolymer-water interfaces probed by electrowetting," *Faraday Discuss.*, 2017.

- [37] R. Zimmermann, U. Freudenberg, R. Schweiß, D. Küttner, and C. Werner, "Hydroxide and hydronium ion adsorption - A survey," *Curr. Opin. Colloid Interface Sci.*, vol. 15, no. 3, pp. 196–202, 2010.
- [38] D. Choi, H. Lee, D. J. Im, I. S. Kang, G. Lim, D. S. Kim, and K. H. Kang, "Spontaneous electrical charging of droplets by conventional pipetting," *Sci. Rep.*, vol. 3, p. 2037, 2013.
- [39] V. A. Marichev, "The adsorption of hydroxide ions on metals," *Electrochim. Acta*, vol. 43, no. 14–15, pp. 2203–2214, 1998.
- [40] A. C. Chen and J. Lipkowski, "Electrochemical and spectroscopic studies of hydroxide adsorption at the Au(111) electrode," *J. Phys. Chem. B*, vol. 103, no. 4, pp. 682–691, 1999.
- [41] E. Celia, T. Darmanin, E. Taffin de Givenchy, S. Amigoni, and F. Guittard, "Recent advances in designing superhydrophobic surfaces," *J. Colloid Interface Sci.*, vol. 402, pp. 1–18, 2013.
- [42] C. C. Cho, R. M. Wallace, and L. A. Files-Sesler, "Patterning and etching of amorphous teflon films," *J. Electron. Mater.*, vol. 23, no. 8, pp. 827–830, 1994.
- [43] P. Muthiah, S. H. Hsu, and W. Sigmund, "Coaxially electrospun PVDF-teflon AF and teflon AF-PVDF core-sheath nanofiber mats with superhydrophobic properties," *Langmuir*, vol. 26, no. 15, pp. 12483–12487, 2010.
- [44] P. Kim, S. C. Jones, P. J. Hotchkiss, J. N. Haddock, B. Kippelen, S. R. Marder, and J. W. Perry, "Phosphonic acid-modified barium titanate polymer nanocomposites with high permittivity and dielectric strength," *Adv. Mater.*, vol. 19, no. 7, pp. 1001–1005, 2007.
- [45] O. Barbieri, M. Hahn, A. Herzog, and R. Kötz, "Capacitance limits of high surface area activated carbons for double layer capacitors," *Carbon N. Y.*, vol. 43, no. 6, pp. 1303–1310, 2005.
- [46] R. Jagdheesh, J. J. Garcia-Ballesteros, and J. L. Ocana, "One-step fabrication of near superhydrophobic aluminum surface by nanosecond laser ablation," *Appl. Surf. Sci.*, vol. 374, pp. 2–11, 2016.

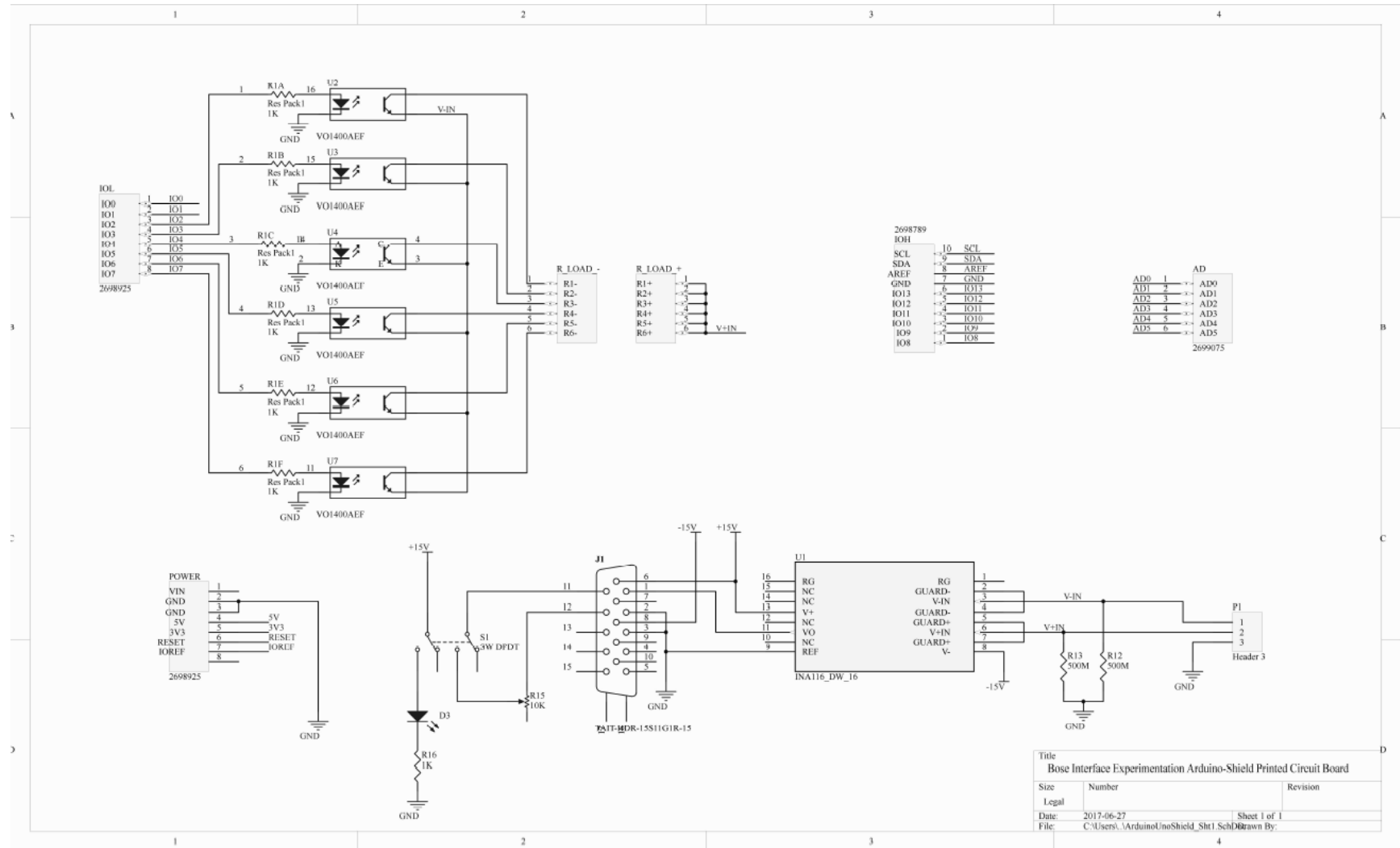
Appendices

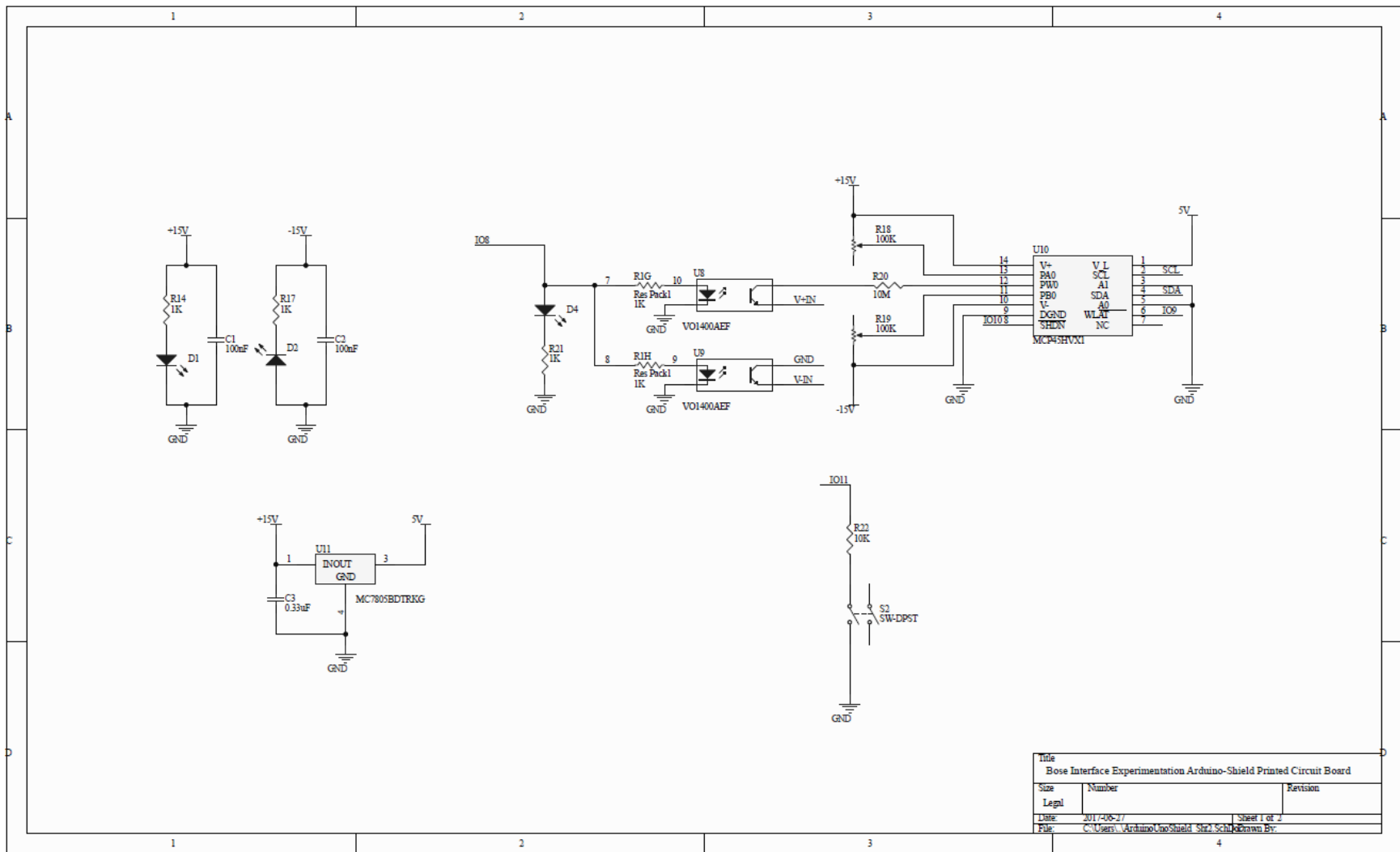
The following includes the Bose Interface and Experimentation Arduino-Shield Printed Circuit Board schematics and layout. Also included in the Appendices is the simulation finite-element MATLAB code.

Appendix A Bose Interface Experimentation Arduino-Shield Printed Circuit Board

This appendix includes the schematics and layout for the printed circuit board designed specifically for interfacing with the Bose® DAQ system and an Arduino Microcontroller.

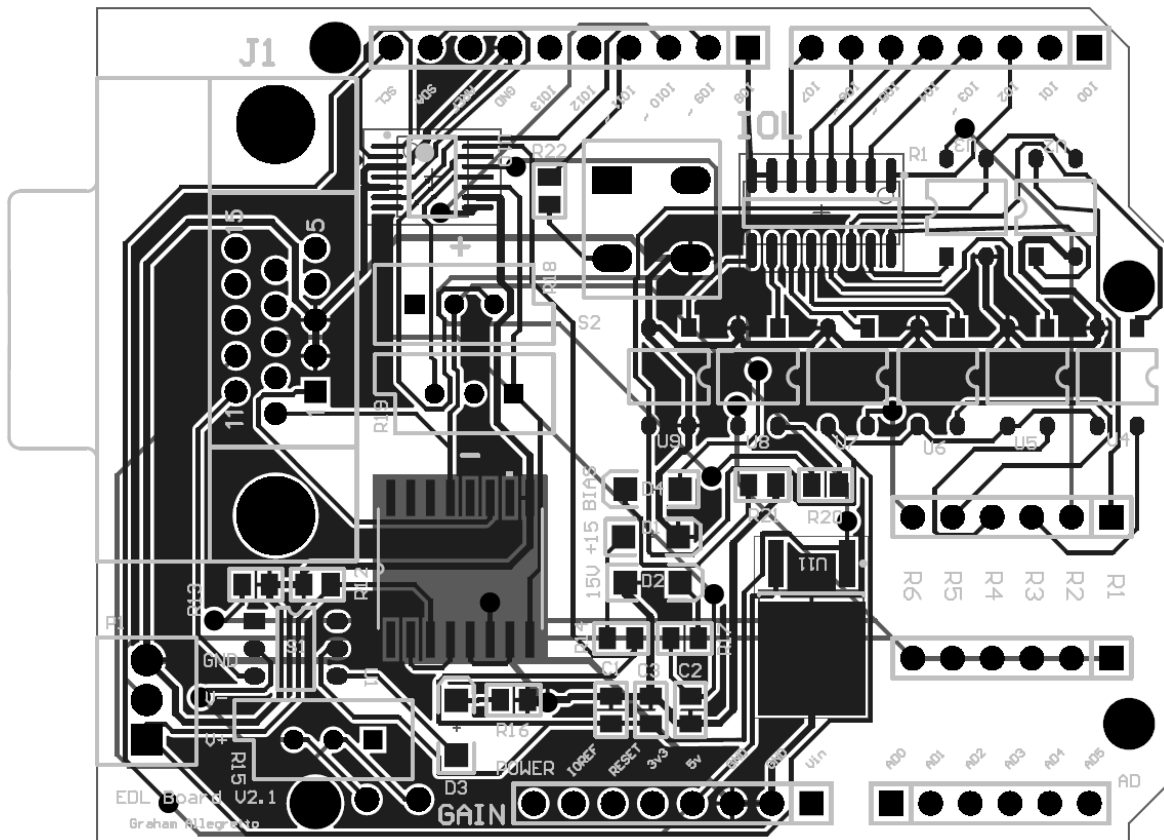
A.1 Schematics





A.2 Layout

Below is the layout of the PCB designed:



Appendix B Arduino Code

Below is the Arduino code developed to run the experimental procedures as explained in previous sections. The code was designed as a simple linear Finite State Machine with four states corresponding to each test. Pressing the button on the PCB initiates a state transition. Also included is a library developed to control the digital potentiometer via I²C. All other libraries are native to the Arduino developing environment according to the IDE used, Arduino 1.8.1.

CompleteTestSuite.ido

```
//
//
//                               EDL Arduino-Bose Test Suite
//                               - By Graham Allegretto
//
// Runs three different test modes:
//
// 1.) Frequency Response
//     - Enables the 10M0hm resistor to run a frequency response
//
// 2.) Load Optimization
//     - Varies the load resistance for a predetermined set amount of time
//       to determine the max power point
//
// 3.) Bias Control
//     - Similar to Load Optimization however this varies the applied bias
//       voltage for a certain interval of time.
//
// 4.) Sawtooth Bias Control
//     - Used for performing multiple back-to-back bias tests.
//
// 5.) Sawtooth Bias Lift-Off Control
//     - Same as Sawtooth Bias Control except it allows for time for the
//       tensiometer to move the top electrode completely off of the droplet
//       after each sawtooth.

#include <Wire.h>
#include "I2C_DigitalPot.h"

//-----
// Pin Declarations
//-----

// Load Resistors
const int R1      = 2;
const int R2      = 3;
const int R3      = 4;
const int R4      = 5;
const int R5      = 6;
```

```

const int R6          = 7;

// Bias Control
const int BIAS_ON    = 8;    // Enables connection to Applied Bias
const int WLAT       = 9;    // Wiper Latch Pin
const int SHTD       = 10;   // Shutdown Pin

// Button
const int BTN        = 11;

//-----
// General Constants
//-----
unsigned long FOREVER = 1000000000;

// Bits specifying which resistors to turn on
const byte R1_BIT = B00000001;
const byte R2_BIT = B00000010;
const byte R3_BIT = B00000100;
const byte R4_BIT = B00001000;
const byte R5_BIT = B00010000;
const byte R6_BIT = B00100000;

// Resistor Values for calculated resistance
const float R1_Val = 981000;
const float R2_Val = 1283000;
const float R3_Val = 1494000;
const float R4_Val = 1777000;
const float R5_Val = 2007000;

// For biasing test
const byte biasLowerVal = 127;

// Sawtooth Wave Test
unsigned long napTime = 3000;
const byte numSteps = 60;
const byte stepSize = 1;
const byte numCycles = 6;

//-----
// State Definition
//-----
typedef enum {
    freqResponseState,
    LoadOptState,
    BiasContState,
    SawToothBiasState,
    SawToothBiasLiftOffState,
} state;
state curState = freqResponseState;

//-----
// Global Variables
//-----
byte potVal = 0;
float currentResistance = 0;
int buttonState = 0;
bool calibrating = false;
bool counting = false;
// Boolean code for which resistors to turn on

```

```

const byte resistorCode[31] =
{16,8,4,2,1,24,20,12,18,10,6,17,9,5,28,3,26,22,14,25,21,13,19,11,7,30,29,27,23,15,31};

//-----
// void setup
//   - Sets pins a sets up serial and I2C.
//-----
void setup() {

  Wire.begin();
  Serial.begin(9600);

  // Setup digital outputs for enabling load resistors
  pinMode(R1, OUTPUT);
  pinMode(R2, OUTPUT);
  pinMode(R3, OUTPUT);
  pinMode(R4, OUTPUT);
  pinMode(R5, OUTPUT);
  pinMode(R6, OUTPUT);

  // Outputs Digital Pot
  pinMode( BIAS_ON, OUTPUT );
  pinMode( WLAT, OUTPUT );
  pinMode( SHTD, OUTPUT );

  // Inputs
  pinMode( BTN, INPUT );

  // Set Resistor Outputs
  digitalWrite(R1, LOW);
  digitalWrite(R2, LOW);
  digitalWrite(R3, LOW);
  digitalWrite(R4, LOW);
  digitalWrite(R5, LOW);
  digitalWrite(R6, LOW);

  // Set Digital Pot Outputs
  digitalWrite( WLAT, LOW );
  digitalWrite( SHTD, HIGH );
  digitalWrite( BIAS_ON, LOW );
  setR( 127 );

  // Print Current State
  Serial.println("Current State: Frequency Response State!");
}

//-----
// void printStateName()
//
//-----
void printStateName()
{
  Serial.println("STATE TRANSITION!");
  Serial.print("Current State: ");
  switch( curState )
  {
    case freqResponseState:
      Serial.println(" Frequency Response State!");
      break;

    case LoadOptState:

```

```

Serial.println(" Load Optimization State!");
break;

case BiasContState:
Serial.println(" Bias Control State!");
break;

case SawToothBiasState:
Serial.println("Saw Tooth Bias State!");
break;

case SawToothBiasLiftOffState:
Serial.println("Saw Tooth Bias Lift Off State!");
break;
}
}

//-----
// void incrementState()
//   Increments state
//-----
void incrementState()
{
  if( curState == SawToothBiasLiftOffState )
  {
    curState = freqResponseState;
  }
  else
  {
    curState = (state)(curState + 1);
  }
  printStateName();
  return;
}

//-----
// bool sleepyTime( unsigned long delayTime )
//   Keeps sleeping until it's awoken by a button press or it's alarm goes
//   off.
//-----
bool sleepyTime( unsigned long delayTime )
{
  unsigned long startTime = millis();
  while(1)
  {
    if( digitalRead( BTN ) == LOW )
    {
      delay(500);
      return true;
    }
    else if( (millis() - startTime) >= delayTime )
    {
      return false;
    }
  }
}

//-----
// void stateSleep( unsigned long delayTime )
//   Sleeps until the button is pressed or it times out. If button is pressed,
//   control returns to caller and the state is incremented. If the button

```

```

// isn't pressed, it'll wait until it timesout.
//-----
bool stateSleep( unsigned long delayTime )
{
  if( sleepyTime( delayTime ) )
  {
    incrementState();
    return true;
  }
  else
  {
    return false;
  }
}

//-----
// void sawToothCycle()
//   Performs one cycle of the sawtooth
//
//-----
bool sawToothCycle( int startVal, int stepSize )
{
  int i;
  int wiperVal;

  for( i = 0; i < numSteps; i++ )
  {
    wiperVal = startVal + i*stepSize;
    setR( wiperVal );
    Serial.println( wiperVal );
    if( stateSleep( napTime ) ) return true;
  }

  return false;
}

//-----
// void loop
//   Finite State Machine
//-----
void loop() {

// Check if the user has pressed the button to increment the state
switch( curState )
{
  /*-----
  *   Frequency Response State -
  *     Sets the Load Resistance to 10MOhms and ensures there isn't an
  *     applied bias. Frequency response load resistor must be installed in
  *     R6 on the PCB.
  *-----*/
  case freqResponseState:
  {
    digitalWrite(R1, LOW);
    digitalWrite(R2, LOW);
    digitalWrite(R3, LOW);
    digitalWrite(R4, LOW);
    digitalWrite(R5, LOW);
    digitalWrite(R6, HIGH);
    digitalWrite( BIAS_ON, LOW );
  }
}
}

```

```

stateSleep( 1000000000 );
break;
}

/*****
*   Load Optimization State -
*       Varies the load resistance based on the resistorCode array that is
*       an output of the Matlab script resistorSearch that takes as input
*       different resistors installed into R1-R5
*****/
case LoadOptState:
{
digitalWrite(R6, LOW);
for (int i = 0; i < sizeof(resistorCode); i++)
{
currentResistance = 0;
digitalWrite( R1, (R1_BIT & resistorCode[i]) ? HIGH : LOW );
currentResistance += ((R1_BIT & resistorCode[i]) ? (1/R1_Val) : 0);

digitalWrite( R2, (R2_BIT & resistorCode[i]) ? HIGH : LOW );
currentResistance += ((R2_BIT & resistorCode[i]) ? (1/R2_Val) : 0);

digitalWrite( R3, (R3_BIT & resistorCode[i]) ? HIGH : LOW );
currentResistance += ((R3_BIT & resistorCode[i]) ? (1/R3_Val) : 0);

digitalWrite( R4, (R4_BIT & resistorCode[i]) ? HIGH : LOW );
currentResistance += ((R4_BIT & resistorCode[i]) ? (1/R4_Val) : 0);

digitalWrite( R5, (R5_BIT & resistorCode[i]) ? HIGH : LOW );
currentResistance += ((R5_BIT & resistorCode[i]) ? (1/R5_Val) : 0);

Serial.print(i+1);
Serial.print(": ");
Serial.println( 1/currentResistance );
if( stateSleep( napTime ) ) break;
}
break;
}

/*****
*   Bias Control State -
*       Turns on the bias control circuit and increments the bias from the
*       wiper position set at biasLowerVal up to biasUpperVal.
*****/
case BiasContState:
{
int i = 0;

setR(biasLowerVal);
delay(5);
digitalWrite(R1, LOW);
digitalWrite(R2, LOW);
digitalWrite(R3, LOW);
digitalWrite(R4, LOW);
digitalWrite(R5, LOW);
digitalWrite(R6, HIGH);
digitalWrite( BIAS_ON, HIGH );
Serial.println("Press the button to start.");
sleepyTime( FOREVER );
if( sawToothCycle( biasLowerVal, stepSize ) ) break;
break;
}

```

```

}

/*****
*   Saw Tooth Bias Control -
*   Performs Bias Control over multiple cycles.
*****/
case SawToothBiasState:
{
  int i = 0;
  int upperBiasVal = biasLowerVal + stepSize*(numSteps-1);
  bool skip = false;

  setR(biasLowerVal);
  delay(5);
  digitalWrite(R1, LOW);
  digitalWrite(R2, LOW);
  digitalWrite(R3, LOW);
  digitalWrite(R4, LOW);
  digitalWrite(R5, LOW);
  digitalWrite(R6, HIGH);
  digitalWrite( BIAS_ON, HIGH );
  Serial.println("Press the button to start.");
  sleepyTime( FOREVER );

  for( i = 0; i < numCycles; i++ )
  {
    if( sawToothCycle( biasLowerVal, stepSize ) ) break;
  }

  break;
}

/*****
*   SawTooth Bias Control Lift Off State -
*   Exactly the same as previous state except it allows for added time
*   for tensiometer to remove the top electrode from contact with the
*   droplet.
*****/
case SawToothBiasLiftOffState:
{
  int i = 0;
  int upperBiasVal = biasLowerVal + stepSize*(numSteps-1);
  bool skip = false;

  setR(biasLowerVal);
  delay(5);
  digitalWrite(R1, LOW);
  digitalWrite(R2, LOW);
  digitalWrite(R3, LOW);
  digitalWrite(R4, LOW);
  digitalWrite(R5, LOW);
  digitalWrite(R6, HIGH);
  digitalWrite( BIAS_ON, HIGH );
  Serial.println("Press the button to start.");
  sleepyTime( FOREVER );

  Serial.println("Wait...");
  if ( stateSleep( 5200 ) ) break;

  for( i = 0; i < numCycles; i++ )
  {

```

```

        if( sawToothCycle( biasLowerVal, stepSize ) ) break;
        setR(biasLowerVal);
        Serial.println("Wait...");
        stateSleep( 6000 );
    }

    break;
}
}
}

```

B.1 Digital Potentiometer Library

I2C_DigitalPot.h

```

//-----
// I2C_DigitalPot.h
//
// For the MCP45HVx1 Digital Potentiometer.
//
//
//-----

#ifndef I2C_DIGITAL_POT_H
#define I2C_DIGITAL_POT_H

// Define Byte codes for different commands
const byte WIPER          = 0;
const byte WRITE          = 0;
const byte INCREMENT     = 1;
const byte DECREMENT     = 2;

// Define the address based on pins A1 and A0
const byte address = B0111100;

// Functions
void send2Pot( byte devAddress, byte memAddress, byte command, byte data );
byte readFromPot( byte devAddress );
void setR( byte rCode );
void incrementR();
void decrementR();

#endif

```

I2C_DigitalPot.cpp

```
#include "Arduino.h"
#include "Wire.h"
#include "I2C_DigitalPot.h"

//-----
// char readFromPot:
//   devAddress - Address of device
//-----
byte readFromPot( byte devAddress )
{
  byte c = 0;
  Wire.requestFrom( devAddress, byte(2) );
  while( Wire.available() )
  {
    c = Wire.read();
  }
  return c;
}

//-----
// void send2Pot:
//   devAddress - Address of device
//   memAddress - Address of Mem
//   command    - command
//   data       - data
//-----
void send2Pot( byte devAddress, byte memAddress, byte command, byte data )
{
  byte msg = (memAddress << 2) | command;
  msg = msg << 2;

  Wire.beginTransmission(devAddress);
  Wire.write(msg);
  Wire.write(data);

  switch( Wire.endTransmission() )
  {
    case 0:
      break;

    case 1:
      Serial.println("Too Long");
      break;

    case 2:
      Serial.println("NACK on Address");
      break;

    case 3:
      Serial.println("NACK on Data");
      break;

    case 4:
      Serial.println("Other Error");
      break;
  }
}

//-----
```

```

// void setResistance( byte rCode )
//   rCode - Address of device
//-----
void setR( byte rCode )
{
    send2Pot( address, WIPER, WRITE, rCode );
}

//-----
// void incrementR()
//   Incrementes resistance 1 value
//-----
void incrementR()
{
    send2Pot( address, WIPER, INCREMENT, 0 );
}

//-----
// void decrementR()
//   Incrementes resistance 1 value
//-----
void decrementR()
{
    send2Pot( address, WIPER, DECREMENT, 0 );
}

```

Appendix C MATLAB Code

This appendix includes the code used to simulate the devices and measure phase and amplitude of raw data. Additional software used to automate processes not included here can be found at

<https://github.com/grahamallegretto/School/tree/master/M-Files>.

C.1 EDL Simulation Code

EDLSimulation.m

```
function [time, SA, v] = EDLSimulation( SAName, varargin )
%EDLSIMULATION Simulates the voltage response of the EDL energy harvester
%based on the surface area of the top electrode
    % SAName - Filename of Bose Data (Must be in proper format)
    % Rl - Load Resistor
    % EDLBiasVoltage - Voltage generated from formation of Double Layer
    % toPlot - Set to true if you want plots

%% Constants %%
ep = 1.93;           % Dielectric Constant of PTFE
ed = 78;            % Dielectric Constant of Water droplet
lambdaD = 150e-9;   % Debye length of water droplet (m)

%% Parameter Defaults %%
epsilon = 8.854e-12; % Permittivity of free space

% Default Values for parameters
defaultRf = 70000;   % Resistance of electrolyte
                    % R = lp/A = (1.5mm * 20MOhm/mm)/15mm^2
defaultRl = 10e6;    % Load resistance
defaultVbias = 0.7;  % The generated voltage across the EDL
defaultPTFE = 30e-9; % Thickness of PTFE Layer (m)
defaultF = 1;        % Frequency of modulation (Hz)
defaultAbottom = 50; % Bottom surface area (mm^2)
defaultUpConFactor = 10; % Upconversion factor
defaultNumSamples = 100000; % Number of samples for artificial signals
defaultNumCycles = 5; % Length of time to run the simulation
defaultSAOffset = 27; % Average surface area (mm^2)
defaultSAamp = 13.5; % Amplitude of surface area signal (mm^2)
defaultToPlot = true; % Whether or not to plot
defaultCloseAll = true; % Whether or not to close all windows

p = inputParser;
addRequired(p, 'SAName', @ischar);
addParameter(p, 'Rf', defaultRf, @isnumeric);
addParameter(p, 'Rl', defaultRl, @isnumeric);
addParameter(p, 'Vbias', defaultVbias, @isnumeric);
addParameter(p, 'dPTFE', defaultPTFE, @isnumeric);
```

```

addParameter(p, 'f', defaultF, @isnumeric);
addParameter(p, 'Abottom', defaultAbottom, @isnumeric);
addParameter(p, 'upConFactor', defaultUpConFactor, @isnumeric);
addParameter(p, 'numSamples', defaultNumSamples, @isnumeric);
addParameter(p, 'numCycles', defaultNumCycles, @isnumeric);
addParameter(p, 'SAOffset', defaultSAOffset, @isnumeric);
addParameter(p, 'SAmp', defaultSAmp, @isnumeric);
addParameter(p, 'toPlot', defaultToPlot, @islogical);
addParameter(p, 'closeAll', defaultCloseAll, @islogical);
parse(p, SAName, varargin{:})

SAName = p.Results.SAName;
Rf = p.Results.Rf;
Rl = p.Results.Rl;
Vbias = p.Results.Vbias;
dPTFE = p.Results.dPTFE;
f = p.Results.f;
Abottom = p.Results.Abottom;
upConFactor = p.Results.upConFactor;
numSamples = p.Results.numSamples;
numCycles = p.Results.numCycles;
SAOffset = p.Results.SAOffset;
SAmp = p.Results.SAmp;
toPlot = p.Results.toPlot;
closeAll = p.Results.closeAll;

if closeAll
    close all
end

%% Surface Area Signal %%
% Can either be a signal that is passed in as a parameter or a step or sine
% wave generated based on the constants listed above
dt = (numCycles*(1/f) ) / numSamples;           % Delta T
time = 0:dt:numCycles*(1/f);                   % Time
Amax = SAOffset + SAmp;
Amin = SAOffset - SAmp;

if size(SAName,2) == 4

    % Sine Wave
    if strcmp(SAName, 'sine')
        SA = ( SAmp .* sin( (2*pi*f).*time ) + SAOffset )';

    % Step Response
    elseif strcmp(SAName, 'step')
        SA = zeros(size(time,2),1);
        SA(1:end) = Amin;
        SA( floor(size(SA,1)/2):end, 1 ) = Amax;
    end

    % If data is passed in
else
    % Read in data
    SData = headerIgnoreCSVRead( SAName );

```

```

SAData = SAData(:, [2 4 6]);

% Since the data we're using from the BOSE machine is in displacement we
% need to convert it to surface area.
SAData(:,2) = SAData(:,2) - mean(SAData(:,2));

AGain = SAamp / max( SAData(:,2) );
SAData(:,2) = (-1.*AGain.*SAData(:,2)) + (SAOffset - mean(SAData(:,2)));

SADataTemp(:,1) = interp(SAData(:,1),upConFactor);
SADataTemp(:,2) = interp(SAData(:,2),upConFactor);

dt = SADataTemp(2,1) - SADataTemp(1,1);
time = SADataTemp(:,1);
SA = SADataTemp(:,2);
end

%% Double Layer Constants and Calculations %%
%
% Constant values
Rprime = (Rf + Rl)/dt; % Used in the simulation
Cb = (epsilon * ed * Abottom * 1e-6) / lambdaD % Bottom capacitance
CbR = Cb*Rprime; % Intermediate value
CtPerArea = (epsilon * ep * 1e-6) / dPTFE; % Capacitance of the top
electrode without the area component (F/mm^2)
Ct = CtPerArea .* SA;
Ct(1)

% Initial Charge Calculation
% Assuming at the beginning that there is no current flow, therefore
% Qb/Cb = Qt/Ct = EDLBiasVoltage
% Charge at each EDL can be calculated
Qb = Vbias * Cb;
Qt = Vbias * Ct(1);

% Linear Model
C = (Ct(1)*Cb)/(Ct(1)+Cb);
CtMin = Amin*CtPerArea;
dCt = Ct(1)-CtMin;
dq = Vbias*dCt; %((CtMin*Qb) - (Qt*Cb)) / (Cb+CtMin);

%% Simulation %%
% Perform the simulation
q = zeros(size(SA));
Vlin = zeros(size(SA));
VlinOut = zeros(size(SA));

Ilin = 2*pi*f*Vbias*(SAamp/SAOffset)*dt;
linearTemp = (1-(dt/C)*(1/(Rl+Rf)));
vDivider = Rl/(Rl+Rf);

for i = 1:size(SA,1)-1

```

```

q(i+1) = ( (Qb-q(i)) / (CbR) ) ...
        - ( (Qt+q(i)) / (Ct(i)*Rprime) )...
        + q(i);

Vlin(i+1) = Vlin(i)*linearTemp + Ilin*cos(2*pi*f*time(i));
VlinOut(i+1) = Vlin(i+1)*vDivider;

% If the next charge is less than the relative accuracy of floating
% point numbers, just set it to 0. If you don't, the simulation
% explodes Ahhhhh!
if abs( q(i+1) ) < eps
    q(i+1) = 0;
end

end

dqdt = diff(q)./dt;
v = (((Qb-q)/Cb) - ((Qt+q)./Ct)).*( Rl / ( Rf+Rl ) );

%% Plot The Data %%

% Plot for self generated Sine/Step Waves
if (size(SAName,2) == 4) && toPlot

    subplotModified( time, SA, v, VlinOut, '', 'Time (s)', 'Surface Area
(mm^2)', ...
        'Voltage (V)', 'Non-Linear Model Response', 'Linear Model Response');

% Plot for Bose Data
elseif toPlot
    subplot(2,1,1);
    plot(time, SA);
    title('Surface Area Plot');
    axis([0 time(end) -inf inf]);
    xlabel('Time (s)');
    ylabel('Surface Area (mm^2)');

    subplot(2,1,2);
    plot( SAData(:,1), -1.*SAData(:,3), time, v );
    title('Voltage Response');
    legend('Measured', 'Simulated');
    axis([0 time(end) -inf inf]);
    xlabel('Time (s)');
    ylabel('Voltage (V)');
end

end
end

```

C.2 Phase Measurement Code

```

function [mag, phase] = transferFuncFind( time, f, refWave, depWave )
%TRANSFERFUNCFIND Summary of this function goes here
% Detailed explanation goes here

```

```

% Get the average of each wave to speed up fitting
meanRefWave = mean(refWave);
meanDepWave = mean(depWave);

% Two separate functions for each wave to accomodate each wave's offset
sineFuncRef = @(x,xdata,meanVal)...
    x(1).*sin((2*pi*f).*xdata + x(2) )+meanRefWave;
sineFuncDep = @(x,xdata,meanVal)...
    x(1).*sin((2*pi*f).*xdata + x(2) )+meanDepWave;

% Starting points
x0Ref = [(max(refWave)-min(refWave))/2, 0];
x0Dep = [(max(depWave)-min(depWave))/2, 0];

% Perform Fitting
xRef = lsqcurvefit( sineFuncRef, x0Ref, time, refWave );
xDep = lsqcurvefit( sineFuncDep, x0Dep, time, depWave );

% If amplitude is negative, reverse the sign of the amplitude and add pi to
% the phase
if( xRef(1) < 0 )
    xRef(1) = xRef(1)*-1;
    xRef(2) = xRef(2) + pi;
end
if( xDep(1) < 0 )
    xDep(1) = xDep(1)*-1;
    xDep(2) = xDep(2) + pi;
end

% If phase is greater than 2pi, get the remainder
xRef(2) = rem( xRef(2), 2*pi );
xDep(2) = rem( xDep(2), 2*pi );

% Set magnitude and phase
mag = xDep(1)/xRef(1);
phase = (xDep(2)-xRef(2))*(180/pi);

% Ensure phase is within +/-180 degrees
if phase < -180
    phase = phase + 360;
elseif phase > 180
    phase = phase - 360;
end
end

```